LAWRENCE
LIVERMORE
NATIONAL
LABORATORY

LLNL-TR-667635

Ultraviolet Light Generation and Transport in the Final Optics Assembly of theNational Ignition Facility

P. Wegner, L. Hackel, M. Feit, T. Parham, M. Kozlowski, P. Whitman

February 23, 2015

Disclaimer

This document was prepared as an account of work sponsored by an agency of the United States government. Neither the United States government nor Lawrence Livermore National Security, LLC, nor any of their employees makes any warranty, expressed or implied, or assumes any legal liability or responsibility for the accuracy, completeness, or usefulness of any information, apparatus, product, or process disclosed, or represents that its use would not infringe privately owned rights. Reference herein to any specific commercial product, process, or service by trade name, trademark, manufacturer, or otherwise does not necessarily constitute or imply its endorsement, recommendation, or favoring by the United States government or Lawrence Livermore National Security, LLC. The views and opinions of authors expressed herein do not necessarily state or reflect those of the United States government or Lawrence Livermore National Security, LLC, and shall not be used for advertising or product endorsement purposes.

This work performed under the auspices of the U.S. Department of Energy by Lawrence Livermore National Laboratory under Contract DE-AC52-07NA27344.

NIF-0017657

Ultraviolet Light Generation and Transport in the Final Optics Assembly of the National Ignition Facility

January, 1999

LAWRENCE LIVERMORE NATIONAL LABORATORY
University of California • Livermore, California • 94550

ECMS NO CM RELEASE 20070611 14:14 0017657 OA (pdf format)

NIF-0017657

Ultraviolet Light Generation and Transport in the Final Optics Assembly of the National Ignition Facility

Lloyd Hackel

Paul Wegner

Mike Feit

Tom Parham

Mark Kozlowski

Pam Whitman

January 8, 1999

LAWRENCE LIVERMORE NATIONAL LABORATORY
University of California • Livermore, California • 94550

ECMS NO CM RELEASE 20070611 14:14 0017657 OA (pdf format)

Acknowledgements

We would like to thank John R. Murray for his significant contributions to the formulation of the frequency conversion error budget. Susan N. Locke helped with the procurement of the Beamlet test crystals. The crystals were machined at Cleveland Crystals, Inc. Processing and assembly took place at LLNL under a team led by Michael E. Werve and Terry D. Schwinn. Special thanks to Tim L. Weiland and the Beamlet operations team for their invaluable suppport in conducting the experiments.

In addition, we would like to thank the following team members who contributed to the optics damage portion of this document: Lun Auyang, Ian Barton, Colin Battersby, Jerry Britten, Sham Dixit, Francis Genin, Steve Herman, Stephen Maricle, Ron Mouser, Mary Norton, John Prior, Mike Rushford, Sheldon Schwartz, Leslie Summers, Chuck Thorsness, Zhouling Wu, and Jim Yoshiyama.

ECMS NO CM RELEASE 20070611 14:14 0017657 OA (pdf format)

Table of Contents

1.0 STATUS AND UNDERSTANDING OF UV LIGHT GENERATION AND TRANSPORT FOR THE NIF 1

2.0 FREQUENCY CONVERTER DEVELOPMENT FOR THE NATIONAL IGNITION FACILITY 3

2.1 Introduction 3

2.2 Frequency Conversion Physics Model 4

2.3 Error Analysis of Frequency Conversion 6

2.4 Beamlet 11

2.5 Conclusion 16

2.6 References 16

3.0 DAMAGE MODEL AND OFF-LINE TESTING 19

3.1 References 26

4.0 HIGH-FLUENCE OPERATION OF KD*P ON BEAMLET 27

4.1 Abstract 27

4.1 Introduction 27

4.3 Beamlet High-Fluence Tests at Air 30

4.4 Beamlet High-Fluence Tests at Vacuum: MDT, HDTI 34

4.5 Beamlet High-Fluence Tests at Vacuum: HDTII 36

4.6 Conclusion 41

4.7 References 41

5.0 OPTICS DAMAGE 43

5.1 Fused Silica Damage 43

5.1.1 Purpose 43

5.1.2 Summary of Optics Used 44

5.1.3 Experimental Techniques 45

5.1.3.1 In-chamber microscopy 45

5.1.3.2 Surface mapping 46

ECMS NO CM RELEASE 20070611 14:14 0017657 OA (pdf format)

5.1.3.3 Laser damage tests 46
5.1.3.4 Fluence distributions 47
5.1.4 Results (not interpretation) 47
5.1.4.1 Focus lens RFL01K 47
Background 47
HDT2 illumination 49
Damage observations on lens RFL01K 49
5.1.5 Debris Shield (no diffractive optics 56
Background 56
Beamlet illumination results 56

5.2 Diffractive Optics Damage 58
5.2.1 DOP1:CSG/BSG 61
5.2.2 DOP2:KPP 72
5.2.3 Debris shield used with diffractive optics (DS02B) 77

5.3 Potential Alternatives to the NIF Baseline 78

5.4 References 79

6.0 IMPROVED AR COATINGS FOR CONVERSION CRYSTALS 81

6.1 Process and Material Development for As-Made Coatings 81

6.2 Characterization of Sol Performance in Clean Vacuum 84

6.3 Development of AR Coatings with Reduced Affinity for Organics 84

6.4 Development of AR Coatings with Reduced Scatter Loss 85

6.5 Facilities Required to Develop and Validate Improved Coatings 88

6.6 Summary 89

6.7 References 89

APPENDIX A, ORTHOGONAL-POLARIZATION INTERFEROMETRY A-1

APPENDIX B, HDTI DAMAGE INVESTIGATION B-1

APPENDIX C, 37-CM TRIPLER (TYPE I & II) AND 5-CM CRYSTALS C-1

ECMS NO CM RELEASE 20070611 14:14 0017657 OA (pdf format)

1.0 Status and Understanding of UV Light Generation and Transport for the NIF

October 1998

The design of the National Ignition Facility (NIF) includes a Final Optics Assembly (FOA) subsystem for ultraviolet (UV) light generation and transport for each of the 192 beamlines. Each subsystem incorporates a type I/type II third-harmonic generator to convert the 1.053-μm fundamental wavelength of the laser amplifier to a wavelength of 0.351 μm for target irradiation. This converter is followed by a large fused silica (SiO2) focusing lens, two diffractive optics plates, and a debris shield. The first diffractive optics plate contains a color separation grating (CGS) etched on the lens side and a beam sampling grating (BSG) etched on the target side. The CGS diffracts the unconverted 1-μm and 0.5-μm light, allowing it to be blocked from transport to the target. The BSG diffracts off a small sample of the UV beam for detailed diagnostics. The second diffractive optics plate contains a kinoform phase map intended to randomize the spatial coherence of the laser light at the target. Finally, the debris shield allows transport of the UV light to the target, while shielding the upstream optics from the shower of debris generated during experiments. To meet the requirements of the NIF, the FOA must achieve high conversion efficiency and must maintain high transmission.

Analytical and experimental work has been done to help understand and predict the performance of the FOA. A prime focus of the work has been a series of experiments on the NIF prototype, Beamlet, at high-fluence loading. These experiments have generated extensive and encouraging information on frequency conversion efficiency and unanticipated results on optics damage. In the five sections of this report, the current status and understanding of (1) frequency conversion efficiency, (2) damage model and off-line testing, (3) observation of damage and damage growth in potassium dihydrogen phosphate (KDP), (4) observation of damage and damage growth in fused silica, and (5) status and potential improvements of coatings for frequency conversion crystals are discussed.

This report is intended to document as a reference the status of work and understanding at the current time. It is not intended to report solutions to the remaining issues. As such, it will serve as an information reference as work progresses through the NIF program.

ECMS NO CM RELEASE 20070611 14:14 0017657 OA (pdf format)

2.0 Frequency Converter Development for the National Ignition Facility

2.1 Introduction

The wavelength of the NIF Nd:glass amplifier will be converted from 1.053 um (1ω) to 0.351 um (3ω) using cascade type I/type II sum-frequency generation [1]. The basic scheme is diagrammed in Figure 2-1. Through experiments conducted on the Beamlet prototype laser over the past year, valuable experience has been gained in operating and characterizing frequency converters of this type at an aperture-size of 37 cm and in a prototypical NIF configuration utilizing full-perimeter mounting of the crystals in a compact final optics cell (FOC) in vacuum [2,3]. Based on this experience, clear identification and greatly improved understanding of the many factors that are expected to impact third-harmonic generation on the NIF has been achieved. Currently, the level of understanding is such that 3ω conversion efficiencies on Beamlet have been predicted to within a few percent of measured values. As a result, it is now clear where the greatest leverage for improving performance lies and where future engineering efforts must be concentrated.

The close agreement between measurement and theory is the result of well-diagnosed experiments and an accurate physics model, for which the input parameters are firmly grounded on measurements or calculation. The next section briefly reviews this model to summarize the relevant crystal and field parameters that are important for frequency conversion. With the model as a tool, a detailed analysis has been performed of the NIF baseline converter design using an error budget approach in which expected deviations of the relevant parameters from their ideal values constitute "errors" resulting in specific reductions in conversion efficiency. The results of this analysis are compared side by side with the results from an identical analysis applied to a Beamlet converter in Section 2.3, followed by a more detailed discussion of the Beamlet experimental data that was used to validate the model in Section 2.4. Section 2.5 concludes with priorities for future work.

ECMS NO CM RELEASE 20070611 14:14 0017657 OA (pdf format)

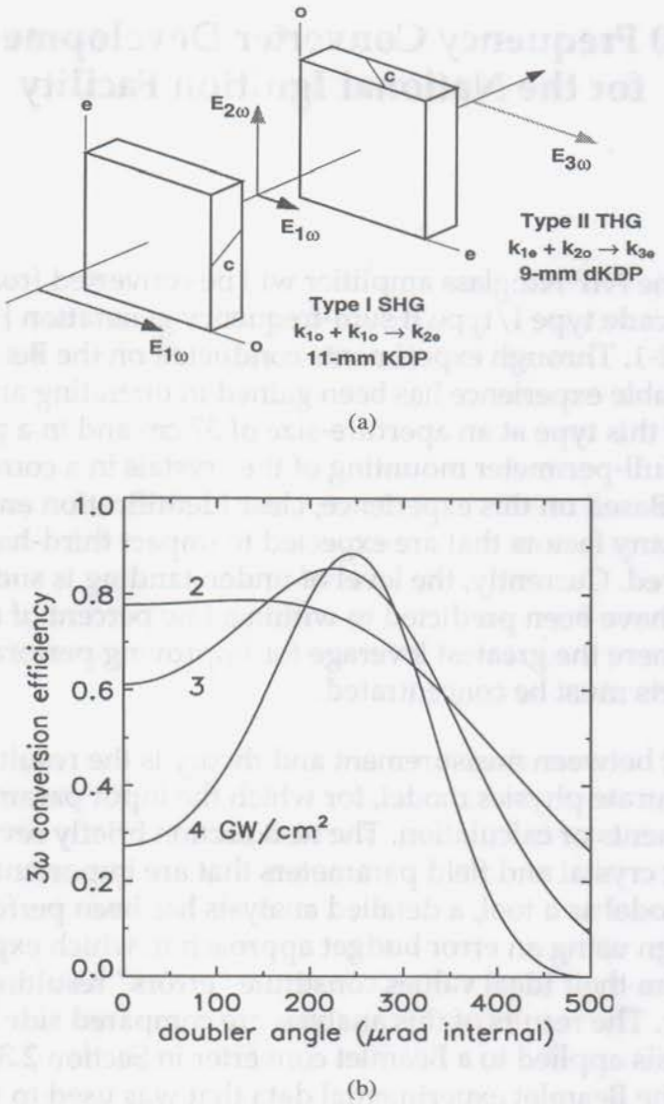

Figure 2-1. (a) Frequency conversion scheme for the NIF, consisting of an 11-mm type-I KDP doubling crystal and 9-mm type-II dKDP tripling crystal in series. The letter c denotes the direction of crystal optic axis. (b) Plane-wave calculation of 3ω conversion efficiency showing how the 1ω/2ω mix ratio for efficient tripling at high irradiance is set by angle-tuning the type-I doubler 200 to 250 μrad from exact phase matching.

2.2 Frequency Conversion Physics Model

The model for the frequency converter is based on the well-known coupled amplitude equations for sum-frequency generation in the paraxial slowly varying envelope approximation [4-6]. As adopted here, the equations include terms for effects identified as

ECMS NO CM RELEASE 20070611 14:14 0017657 OA (pdf format)

having small, but non-negligible impacts on frequency conversion: bulk linear loss, diffraction, Poynting vector walk-off, 2-photon absorption at the third harmonic, and nonlinear refractive index. In comparison, the effects of group velocity dispersion are negligible for this application and are not included in the model.

With the following definitions for the three fields associated with sum frequency generation

$$E_j(x,y,z,t) = \frac{1}{2}\frac{1}{\sqrt{n_j}} A_j(x,y,z,t)\exp[i(k_j z - \omega_j t)] + c.c\,, \qquad j = 1, 2, 3 \tag{1}$$

the equation for the sum-generated field A_3 has the form

$$\left(\frac{\partial}{\partial z} + \frac{1}{v_{g3}}\frac{\partial}{\partial t}\right)A_3 = -\frac{i}{2k_3}\nabla_\perp^2 A_3 - \frac{1}{2}\left(\alpha_3 + \beta_3|A_1|^2\right)A_3 + \frac{i}{2}k_{30}\varepsilon_0 c\left(2\gamma_{31}|A_1|^2 + 2\gamma_{32}|A_2|^2 + \gamma_{33}|A_3|^2\right)A_3$$
$$-\rho_3\frac{\partial A_3}{\partial r_e} + i\omega_3 K A_1 A_2 \exp[-i\Delta k z] \tag{2}$$

with similar equations applying for A_1 and A_2. In this expression, the quantity having by far the greatest impact on conversion efficiency, and the one that is also the most sensitive to operating conditions, is the momentum mismatch between the three fields

$$\Delta k = k_3 - k_2 - k_1 = \frac{1}{c}[\omega_3 n_3 - \omega_2 n_2 - \omega_1 n_1]\,, \qquad \omega_3 = \omega_1 + \omega_2 \tag{3}$$

which depends critically on the material birefringence (refractive indices n_j), and thus on the frequency of the input fields ω_1, ω_2, the crystal temperature T, and the orientation θ of the crystal optic axis with respect to the field propagation direction. Complicating the picture in large crystals is an effective variation of θ in x and y due to surface refraction and strain effects [7,8]. Some of the strain resides naturally in the crystal as a residue of the growth and fabrication process. In practice, however both θ and T can be treated as applied quantities, extrinsic to the material, and subject to characterization through measurement. For example, errors in average crystal orientation from specified values are either estimated from fabrication tolerances or measured. Variations in θ across the part due to refraction or stress are quantified after mounting using a technique called orthogonal-polarization interferometry, as described in Appendix A.

Parameters that are intrinsic to the crystals include the linear and nonlinear loss coefficients α_j and β_j, the nonlinear coefficient for the refractive index γ_{ji}, and the field coupling coefficient

ECMS NO CM RELEASE 20070611 14:14 0017657 OA (pdf format)

$$K = \frac{d_{eff}}{c\sqrt{n_1 n_2 n_3}} \tag{4}$$

where d_{eff} depends weakly on the orientation as $d_{36}\sin\theta\sin2\phi$ for type-I, and $d_{36}\sin2\theta\cos2\phi$ for type-II. Definition of the losses incurred at each crystal surface and a suitable approximation for the amplitude and phase profiles of the field at the input to the crystals complete the parameter specifications that are required for the model.

2.3 Error Analysis of Frequency Conversion

Using this physics model, an error analysis of the converter design has been performed to determine the performance that can be expected for the NIF ICF mission and to compare this performance with the peak-power conversion efficiency specified in the current NIF system performance model [9]. In the context of this analysis, factors that cause the parameters of the converter model to deviate from conditions defined as "ideal" constitute "errors" that produce a calculable reduction in conversion efficiency. The effect of each error is calculated separately, and with the assumption that the effects of small errors add independently, both the total reduction in efficiency relative to an ideal converter and the aspects of the design that are primarily responsible for the loss are determined. The starting point, or zero-error condition that produces maximum achievable tripling efficiency, is a plane-wave flat-in-time input field, an 11-mm thick type-I KDP doubler, and a 9-mm thick type-II dKDP tripler with both crystals having nominal bulk losses and perfect antireflection (AR) coatings. The drive irradiance of 3 GW/cm^2 used in the analysis is slightly higher than the 2.8 GW/cm^2 used in the NIF performance model, as insurance against reductions in the NIF beam size. At 3 GW/cm^2 the optimum tuning for the angle-tuned type-I doubler is 220 μrad (internal) from exact phase matching, and the ideal conversion efficiency is 89.4% (see Figure 2-1). The parameters used in the ideal model are summarized in Table 2-1.

Table 2-1. Parameters of the ideal converter model.

Parameter	units	doubler		tripler*	
l	mm	11.0	[1]	9.0	[1]
α_1	cm^{-1}	0.058	[10]	0.002	[11]
α_2	cm^{-1}	0		0	
α_3	cm^{-1}	0		0	
d_{36}	pm/V	0.39	[10]	0.37	[10,12]
θ_m	degrees	41.2	[13]	60.1	[14]
$\Delta\theta$	μrad	220		0	
surface loss	%	0		0	

* 70% deuteration level

Errors important for the analysis fall into two categories depending on whether they are static or dynamic. Static errors remain invariant from shot to shot and as such, can potentially be compensated for by varying the input 1ω drive irradiance. Errors of this type encompass

ECMS NO CM RELEASE 20070611 14:14 0017657 OA (pdf format)

reductions associated with a non plane-wave 1ω beam, including fill factor, amplitude/phase ripple, depolarization, and bandwidth; linear loss beyond nominal in the crystals and AR coatings; nonlinear loss in the crystals, including 2-photon absorption; and static angular errors in the crystals arising from uncertainties in the optimum tuning angle, or from spatial nonuniformity of the tuning angle associated with crystal quality and mounting distortion. In contrast, dynamic errors vary from shot to shot, cannot readily be compensated, and thus affect the ability to balance power on target. Identified errors of this type can all be related to angle: fluctuations in the crystal temperature, variability in crystal alignment, vibration and drift in the FOA, and pulsed beam pointing errors. The effects of these two categories of errors were evaluated separately.

Current engineering estimates for the dynamic errors are shown in Table 2-2. Because these errors are random, they are assumed to add in a root-sum-squares (RSS) manner, yielding a total error of ~±13 μrad (external angle, 1σ). At 3 GW/cm^2, the angular sensitivity of the type-I doubler is such that a 30-μrad external-angle error reduces the conversion efficiency by 1%, and a 55-μrad error reduces the efficiency by 3% (the angular sensitivity of the type-II tripler is smaller by a factor of three). The variation in conversion efficiency allowed by the NIF power balance budget is ±1% 1σ, thus the dynamic errors in the FOA should be within this budget.

Table 2-2. Dynamic error estimates for frequency conversion.

Error Source	Equivalent Δθ (μrad external, 1(σ)		Comments
FOA contributions:			
± 0.1° C short-term thermal drift	± 4		80 μrad (internal) /°C for doubler [15]
Structural motion	± 10	[16]	
FOC alignment	± 2	[17]	most of error is static
Beam contributions:			
pointing jitter	± 7	[17]	
RSS sum	± 13		

The individual and cumulative effects of the static errors are summarized in Table 2-3, which lists the representative values for the parameters in the physics model and their calculated effect on the efficiency for three cases: the converter in the NIF system performance model, a converter based on current NIF engineering estimates, and a converter as tested on Beamlet. Entries in the table are grouped according to whether they are associated with the input field, the doubler, or the tripler. To calculate the total losses in performance listed at the bottom of the table, the absolute percent losses in each of the three groups were added together, divided by 100, and subtracted from one to generate three separate derate factors for the ideal efficiency. Losses denoted by an asterisk represent 1σ values for an expected distribution and were added as root sum squared. The efficiencies in the table were calculated for flat-in-time pulse shapes, and as such correspond to aperture-averaged peak-power conversion efficiencies at 3 GW/cm^2. A less-than-unity temporal fill factor such as that of a real pulse will further decrease the efficiency.

ECMS NO CM RELEASE 20070611 14:14 0017657 OA (pdf format)

Table 2-3. Static error estimates for frequency conversion.

Parameter	Ideal value	NIF system performance model value	NIF system performance model Δη (%)	Current NIF estimate value	Current NIF estimate Δη (%)	Beamlet value	Beamlet Δη (%)
1ω pulse:							
Bandwidth (GHz)	0	30	1.45	30	1.45	30	1.45
Depolarization (deg)	0	0	0	3	0.30*	5.4	0.90
Fill factor (%)	100	90	0.53	90	0.53	88	
Amplitude/phase ripple	0	NIF	0.15	NIF	0.15	BLT	1.29
Collimation error (λ)	0	0	0	1.25	0.07	0.25	0.1
Irradiance (GW/cm^2)	3.0	2.8	0.86	3.0	0	3.0	0
Subtotal			2.99		2.22		3.74
Doubler:							
Linear loss (%/cm)							
α_{1o}	5.8	5.8	0	5.8	0	5.8	0
α_{2e}	0	0	0	0	0	0	0
Surface loss (%)							
R_1 (1ω)	0	0.5	0.56	0.2	0.22	1.65	1.85
R_2 (1ω, 2ω)	0	0.5	0.57	0.7	0.80	2.35	2.69
Static angle (μrad internal)							
nominal	220	220	0	220	0	220	0
quality/mounting (1σ)	0	0	0	25	1.19	25	1.19
alignment offset	0	0	0	10	0.60*	10	0.60*
thermal correction error	0	0	0	5	0.05*	5	0.05*
Subtotal			1.13		2.29		5.76
Tripler							
Linear loss (%/cm)							
α_{1e}	0.2	0.2	0	0.2	0	0.2	0
α_{2o}	0	0	0	0.1	0.03	0.1	0.03
α_{3e}	0	0	0	0.3	0.16	0.3	0.16
Nonlinear loss							
$\beta_{3\omega}$ (cm/GW)	0	6.0e-3	0.57	6.0e-3	0.57	6.0e-3	0.57
Surface loss (%)							
R_1 (1ω, 2ω)	0	0.5	0.57	0.7	0.80	2.35	2.69
R_2 (3ω)	0	0.5	0.50	0.2	0.20	1.30	1.30
Static angle (μrad internal)							
nominal	0	30	0.28	0	0	0	0
quality/mounting (1σ)	0	0	0	75	1.86	75	1.86
alignment offset	0	0	0	10	0.09*	10	0.09*
thermal correction error	0	0	0	20	0.12*	20	0.12*
Subtotal			1.92		3.62		6.61
Net efficiency	89.4	84.1		82.3		75.8	

* Losses representing 1σ values for an expected distribution, which were added as root sum squared.

ECMS NO CM RELEASE 20070611 14:14 0017657 OA (pdf format)

The error analysis result of 84.1% efficiency for the NIF system performance model is within 0.6% of the actual value produced by a full calculation with that model, lending confidence that the error analysis approach is sound. The conversion efficiency based on current NIF engineering estimates is a few percent lower than that in the system model, primarily due to angular errors not included in that model. On the other hand, the NIF estimate is over 6% higher than the conversion efficiency predicted for the rapid-growth Beamlet converter described in the next section. Only a small part of the discrepancy between the NIF estimate and Beamlet prediction is related to differences between the NIF and Beamlet beams. The majority is associated with surface losses caused by rapid degradation of the sol-gel AR coatings in the vacuum test environment. These losses are currently not in the NIF engineering estimate. As a result, coatings are an area of uncertainty in this design and have a high priority for future development efforts. In addition, two other aspects of the design require attention to ensure that the specifications reflected in the budget are carried successfully to the NIF. First, the tight angular tolerances of the converter are such that the tripler must phase match at an angle of 10.58 mrad ± 30 μrad (external) relative to the beam direction, as fixed by the NIF system design. The fabrication and metrology process to meet this tolerance requires some additional development and testing, including the design and implementation of a machine to correctly orient the crystal surfaces during fabrication, and the development of a means to verify the optimum tilt angle for the assembled FOC to within the 10 μrad specified in the static error budget prior to installation on the NIF. Both of these efforts are currently under way. Second, the tolerance for long-term temperature drift in the FOA is ±0.3 °C, which is large enough that some amount of compensating adjustments to the tilt angle of the FOC will be required. Fully compensating the tripler, which thermally tunes at a rate of ~200 μrad/°C, is expected to use up approximately two-thirds of the alignment and diagnostics sensor's field of view.

Crystal thickness is a special case of a static error that directly impacts power balance. As shown in Figure 2-2, the conversion efficiency is most sensitive to crystal thickness in the low-irradiance foot of the shaped ICF ignition pulse. The current specified tolerance of 0.2 mm meets the budgeted allocation for power balance throughout the pulse (Figure 2-2b) and allows the crystals to be refinished at least once. Fortunately, crystal thickness variations can be budgeted independently of the dynamic errors in Table 2-2, since the angular errors in 2- 2 affect power balance only at high irradiance, where sensitivity to angle is large, but sensitivity to crystal thickness is small.

ECMS NO CM RELEASE 20070611 14:14 0017657 OA (pdf format)

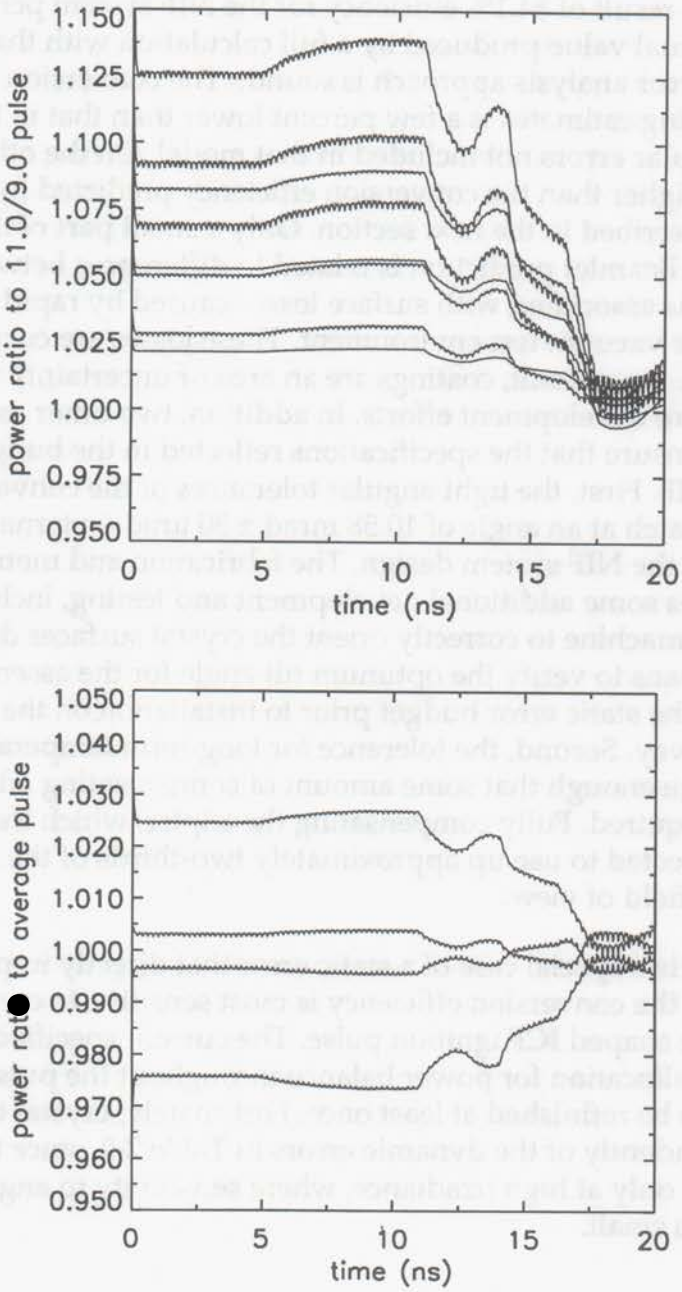

Figure 2-2. (a) Calculation of 3ω power versus time in the 20-ns shaped ICF ignition pulse for various crystal thicknesses, normalized to the 3ω power produced by the baseline 11.0-mm doubler/9.0-mm tripler combination. (b) Similar plot for four crystal thickness combinations representing limits of the current 2-mm tolerance, normalized to the average power produced by the four combinations. High-frequency structure is the result of the applied 30-GHz SBS-suppression bandwidth.

ECMS NO CM RELEASE 20070611 14:14 0017657 OA (pdf format)

2.4 Beamlet

The physics model used in the error analysis has been tested and validated over the course of several frequency conversion experimental campaigns conducted on Beamlet. Extensive diagnostics provided an accurate and complete set of input parameters for the model, as well as the frequency conversion performance data to which it was compared. Off-line diagnostics included orthogonal-polarization interferometry to determine crystal refractive index nonuniformities and photometry to measure crystal surface losses and bulk transmission, both before and after the experiments. On-line diagnostics included calorimetry to measure the input and output pulse energies, scientific-grade charged coupled device (CCD) cameras to record the input and output near-field fluence distributions, and streak cameras to record the input and output temporal pulse shapes. Several Beamlet test configurations, summarized in Table 2-4, were used to evaluate both second-harmonic generation (SHG) and third-harmonic generation (THG) efficiencies, with converters consisting of both conventionally grown and rapidly grown crystals [18]. All of the crystals were mounted in a prototype 37-cm aperture FOC and tested in the vacuum environment of the FOA test mule [19,20]. The configuration of the Beamlet amplifier was the same for all tests: eleven cavity amplifiers, five booster amplifiers, a 200-μrad carbon pinhole in the pass-4 cavity spatial filter pinhole, and a 150-μrad stainless-steel cone pinhole in the transport filter. Pulse format was 1.5-ns square. Estimated accuracy of the conversion efficiency measurements was ± 6% (3σ).

Table 2-4. Configuration and results summary for Beamlet FOA test mule frequency conversion experiments.

Parameter	Conventional growth		Rapid growth	
	SHG	THG	SHG	THG
1ω laser				
Beam size (cm)	34	34	34	30
Doubler				
Serial number	345-1	345-1	RG8B-2	RG8B-2
Thickness (mm)	11.09	11.09	11.10	11.10
θ distribution (μrad int. 1σ)	22.3	18.8	17.5	27.8
Surface loss (% before/after)				
S_1 (1ω)	0.91/-	-/1.49	1.03/-	1.64/1.67
S_2 (1ω)	0.91/-	-/1.49	1.03/-	1.64/1.67
S_2 (2ω)	1.70/-	-/2.53	1.48/-	2.85/3.30
Tripler				
Serial number	-	LL1-37-1	-	RG8A-1
Thickness (mm)	-	9.48	-	9.41
Deuteration level (%)	-	70	-	85
θ distribution (μrad int. 1σ)	-	36.2	-	67.7
Surface loss (% before/after)	-		-	
S_1 (1ω)	-	0.60/-	-	2.75/3.05
S_1 (2ω)	-	1.82/-	-	1.30/2.20
S_2 (3ω)	-	0.10/-	-	0.37/2.21
Measured performance				
Maximum energy efficiency (%)	73	75	70.5	73.5
At 1ω irradiance (GW/c m^2)	4.0	3.8	3.9	3.6

ECMS NO CM RELEASE 20070611 14:14 0017657 OA (pdf format)

SHG efficiencies measured with a conventionally grown type-I doubler from a NIF production boule are plotted in Figure 2-3(a). Maximum energy efficiency was 73% (aperture-averaged, time-integrated) at an input 1ω irradiance of approximately 4 GW/cm^2 (aperture-averaged, peak-in-time). Similar tests of a rapidly grown type-I doubler achieved 70.5% efficiency at similar drive irradiance. The measured performance of these crystals was in good agreement with modeling based on measured 1ω pulse parameters and measured crystal refractive-index variations. The effects of the latter were enhanced by measuring the 2ω near-field fluence distributions with the crystal tilt biased well away from exact phase matching. As shown in Figure 2-4, the resulting nonuniformities in the data were well-reproduced in the model.

THG efficiencies measured with a rapidly grown doubler and tripler are plotted in Figure 2-3(b). Maximum energy efficiency was 73.5% at an input 1ω irradiance of approximately 3.6 GW/cm^2. In comparison, the model, with an input field based on near-field 1ω irradiance data and an eleven time-slice approximation of the measured 1ω pulse shape, predicted an energy conversion efficiency of 77% and a peak-power conversion efficiency of 79.5%. Correcting the model to account for the 30-GHz bandwidth of the drive pulse and the measured depolarization in the Beamlet laser (see Table 2-3) lowers the calculated energy efficiency to 75%. Incorporating the additional losses caused by the degradation of the sol-gel AR coatings over the course of the experiment further reduces the efficiency to 71.5%, suggesting that the model is accurate to within the uncertainty in the component transmissions (the calculated peak-power conversion efficiency in this case is 74%). Calculated and measured near-field fluence distributions for both the third-harmonic and residual second-harmonic fields are in fairly good agreement as a result of having the orthogonal-polarization interferomery data incorporated in the model (see Figure 2-5). The energy balance in the model (the ratio of total energy out of the converter to total energy into the converter) is ~3% higher than observed, consistent with the actual transmissions of the components in vacuum being lower than the initial values modeled.

ECMS NO CM RELEASE 20070611 14:14 0017657 OA (pdf format)

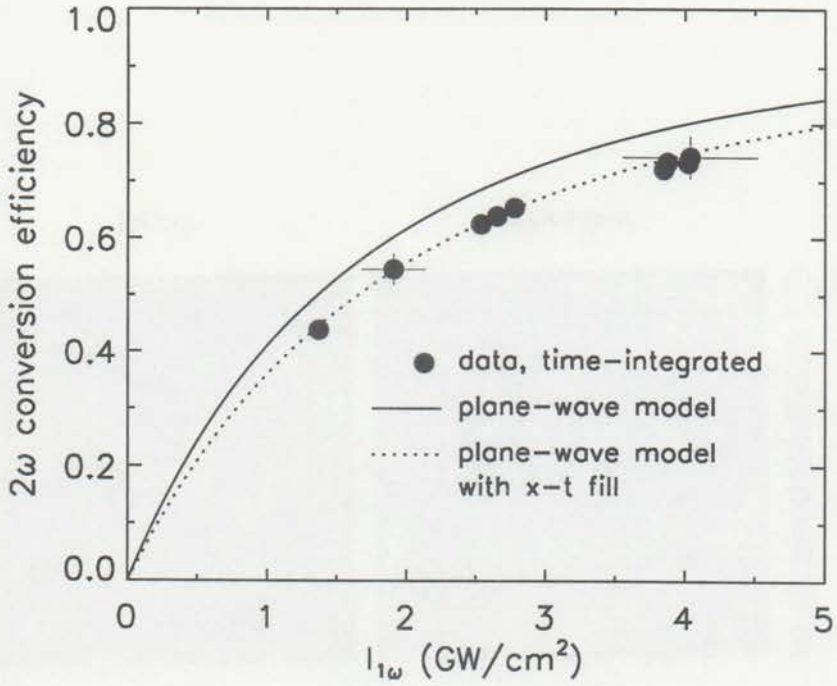

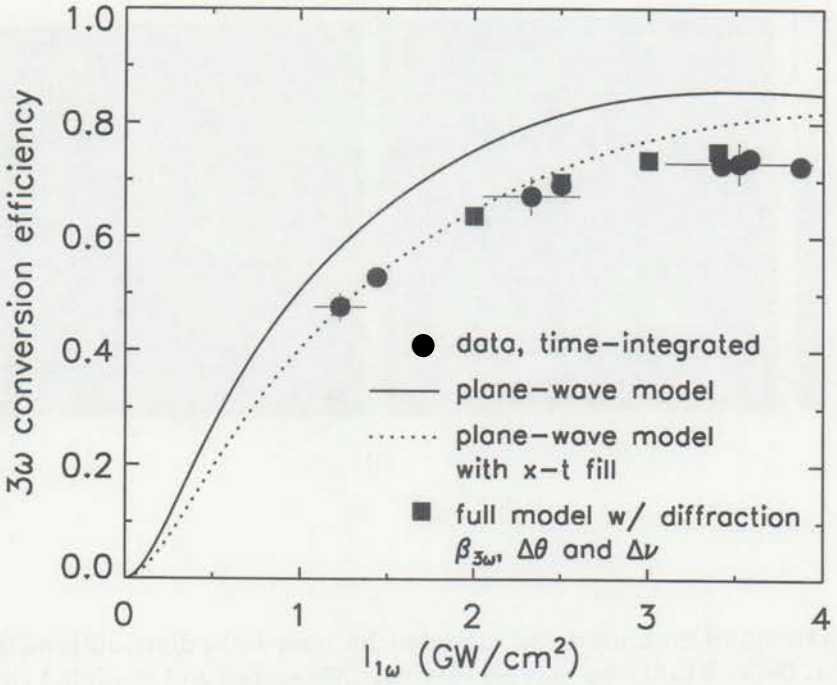

Figure 2-3. (a) Plot comparing measured and calculated SHG efficiency versus 1ω irradiance for conventional-growth doubler 345-1. (b) Comparison of measured and calculated THG efficiency for rapid-growth doubler RG8B-2 and tripler RG8A-1.

ECMS NO CM RELEASE 20070611 14:14 0017657 OA (pdf format)

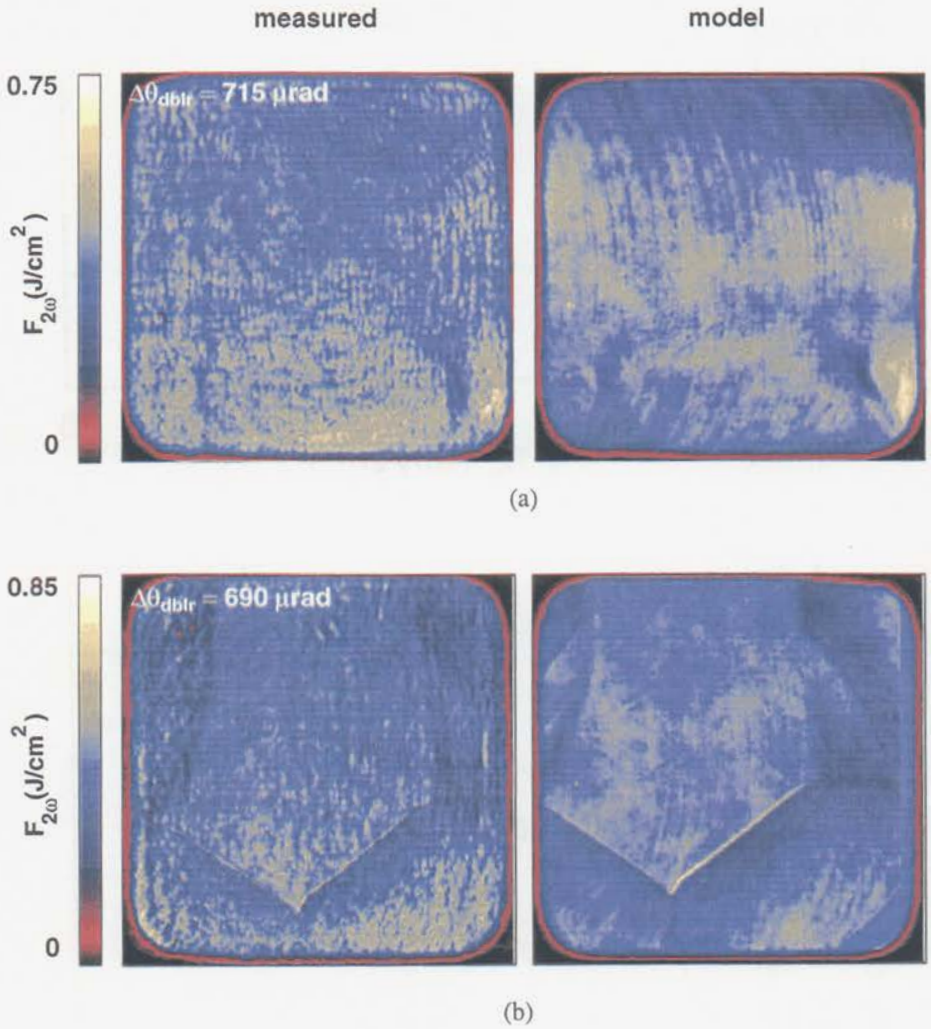

Figure 2-4. (a) Comparison of measured and modeled 2ω near-field distributions for conventional-growth doubler 345-1. Drive irradiance was 3.9 GW/cm^2. Measured and modeled conversion efficiencies were 6.7 and 6.5% respectively at an angular detuning of 715 μrad (internal). (b) Similar comparison for the rapid-growth doubler RG8B-2. Drive irradiance was 4.2 GW/cm^2. Measured and modeled conversion efficiencies were 6.6 and 7.0% respectively at an angular detuning of 690 μrad (internal). Sharp features in (b) are the boundaries between pyramidal and prismatic growth regions in the crystal. Conventional growth material is all pyramidal.

ECMS NO CM RELEASE 20070611 14:14 0017657 OA (pdf format)

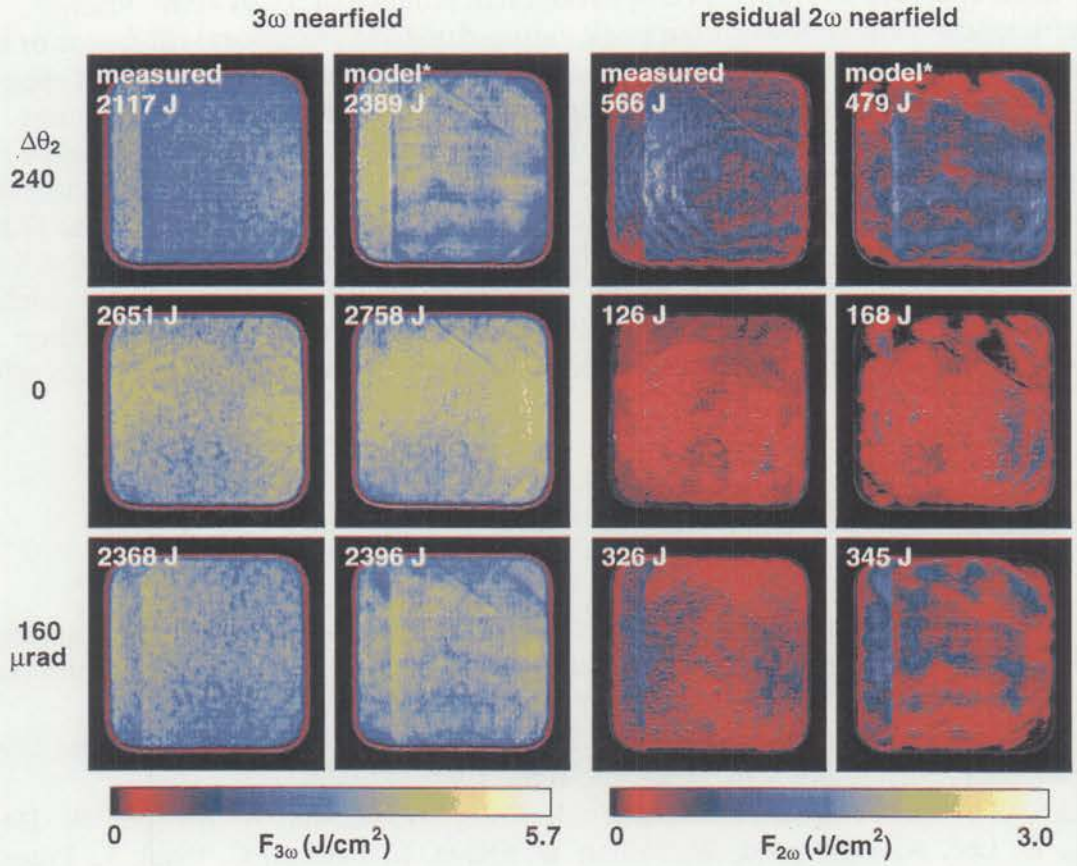

Figure 2-5. Comparison of measured and modeled near-field fluence distributions for the rapid-growth converter on three different shots in which the tripler angle was varied while the doubler angle was held fixed at 220 μrad. Drive irradiance was 3.4 ± 0.05 GW/cm2. Measured 3ω conversion efficiencies top to bottom were 56, 73, and 66%.

ECMS NO CM RELEASE 20070611 14:14 0017657 OA (pdf format)

2.5 Conclusion

Recent experimental results from Beamlet and detailed modeling indicate the NIF baseline frequency converter should achieve aperture-averaged peak-power 3ω conversion efficiencies of 75 to 80% at an aperture-averaged peak-power 1ω irradiance of 3 GW/cm^2. Energy conversion efficiencies will be lower than peak values due to the temporal fill-factor of the drive pulse, which is always less than one. Error analysis has been used to identify aspects of the converter design that have high leverage for improving performance. Of particular importance are the sol-gel AR coatings, which degrade rapidly to a few percent loss per surface in typical vacuum environments. Of lesser concern, but representing some uncertainty, are the tight angular tolerances to which the crystals must be cut and oriented in the FOC to ensure phase-matching within the narrow field of view of the NIF output sensor, and the relatively loose tolerance of ±0.3°C for the long-term thermal stability of the FOA, which will require compensating angular adjustments to the FOCs with associated errors. Further attention in each of these areas will be needed to ensure 80% peak-power conversion efficiency on NIF.

2.6 References

1. C.E. Barker, B. M. VanWonterghem, J.M. Auerbach, R.J. Foley, J.R. Murray, J.H. Campbell, J.A. Caird, D.R. Speck, and B. Woods, "Design and performance of the Beamlet laser third harmonic frequency converter," *Proc. Soc. Photo-Opt. Instrum. Eng.*, Vol. 2633, 398 (1995).
2. R.E. English Jr.,J. Miller, C. Laumann, and L. Seppala, *ICF Annual Report*, Lawrence Livermore National Laboratory, Livermore, CA, UCRL-LR-105821-97, 112 (1997).
3. V. Karpenko, C. Adams, J. Chael, P. Dohoney, R. Foley, W. Gibson, W. Hibbard, W. Horton, J. Latkowski, D. Lee, A. McDonald, W. Miller, W. Olson, L. Parietti, C. Patel, L. Pittenger, P. Pittman, T. Reitz, D. Trummer, H. Walther, R. Wavrik, W. Weed, and K. Wong, *ICF Annual Report*, Lawrence Livermore National Laboratory, Livermore, CA, UCRL-LR-105821-97, 166 (1997).
4. J.A. Armstrong, N. Bloembergen, J. Ducuing, and P.S Pershan, "Interactions between light waves in a nonlinear dielectric," *Phys. Rev.*, Vol. **127**, 1918 (1962).
5. D. Eimerl, J. M Auerbach, and P.W. Milonni, "Paraxial wave theory of second and third harmonic generation in uniaxial crystals. I. Narrowband pump fields," *J. Mod. Opt.*, Vol. **42**, 1037 (1995).
6. J.M. Auerbach, C.E. Barker, D. Eimerl, K.R. Manes, D. Milam, P.W. Milonni, J.B. Trenholme, and B. VanWonterghem, *ICF Quarterly Report*, Lawrence Livermore National Laboratory, Livermore, CA, UCRL-LR-105821-96-4, 199 (1996).
7. J.J. DeYoreo and B. Woods, "A study of residual stress and the stress-optic effect in mixed crystals of $K(D_xH_{1-x})_2P\ O_4$," *J. Appl. Phys.*, Vol. **73**, 7780 (1993).
8. J.M. Auerbach, C.E. Barker, S.A. Couture, D. Eimerl, J.J. DeYoreo, R.L. Hibbard, L.W. Liou, M.A. Norton, S.A. Perfect, P.J. Wegner, and L.A. Hackel, "Modeling of frequency doubling and tripling with converter crystal refractive index spatial non-uniformities," Third International Conference on Solid-State Lasers for Application to Inertial Confinement Fusion, Monterey, CA., June 10, 1998.

ECMS NO CM RELEASE 20070611 14:14 0017657 OA (pdf format)

9. R. Sacks and W. Williams, "NIF performance summary for the 11-0-5 configuration," internal report NIF-000858, Lawrence Livermore National Laboratory, Livermore, CA. 94550 (1996).
10. D. Eimerl, "Electro-optic, linear, and nonlinear optical properties of KDP and its isomorphs," *Ferroelectrics*, Vol. **72**, 95 (1987).
11. C.A. Ebbers, J. Happe, N. Nielsen, and S.P. Velsko, "Optical absorption at 1.06 μm in highy deuterated potassium dihydrogen phosphate," *Appl. Opt.*, Vol. **31**, 1960 (1992).
12. V.G. Dmitriev, G.G. Gurzadyan, and D.N. Nikogosyan, *Handbook of Nonlinear Crystals*, Springer-Verlag, Berlin, 1991.
13. Calculated from the refractive index data of Zernike in Ref. 10.
14. Calculated from refractive index data of Kirby in Ref. 10 and extrapolated to 70% deuteration.
15. R.S. Craxton, S.D. Jacobs, J.E. Rizzo, and R. Boni, "Basic properties of KDP related to the frequency conversion of 1-μm laser radiation," *IEEE J. Quant. Elec.*, Vol. **QE-17**, 1782 (1981).
16. C. Adams, "Angular thermo-mechanical stability budget for the NIF frequency conversion crystals," internal report NIF-0002724-0B, Lawrence Livermore National Laboratory, Livermore, CA. 94550 (1997).
17. E. Bliss, "NIF alignment system accuracy for frequency conversion crystals," internal report NIF-0008425, Lawrence Livermore National Laboratory, Livermore, CA. 94550 (1997).
18. N.P. Zaitseva, J.J. De Yoreo, M.R. DeHaven, R.L. Vital, K.E. Montgomery, M. Richardson, and L.J. Atherton, "Rapid growth of large-scale (40-55 cm) KH_2PO_4 crystals," *J. Cryst. Growth*, Vol. **180**, 255 (1997).
19. P.J. Wegner, J.M. Auerbach, C.E. Barker, K.R. Brading, J.A. Britten, S.C. Burkhart, J.A. Caird, S.N. Dixit, P. Feru, M.A. Henesian, R.L. Hibbard, M.R. Kozlowski, D. Milam, J.E. Murray, M.A. Norton, J.E. Rothenberg, T.L. Weiland, W.H. Williams, S.E. Winters, B.M. VanWonterghem, and R.A. Zacharias, "Recent performance results of the Beamlet prototype for the National Ignition Facility," Conference on Lasers and Electro-Optics, San Francisco, CA., May 7, 1998
20. S.C. Burkhart, K.R. Brading, P.M. Feru, M.R. Kozlowski, J.E. Murray, J.E. Rothenberg, B.M. VanWonterghem, P.J. Wegner, and T.L. Weiland, "High-fluence and high-power 1.05-μm and 351-nm performance experiments on Beamlet," Third International Conference on Solid-State Lasers for Application to Inertial Confinement Fusion, Monterey, CA., June 9, 1998.

ECMS NO CM RELEASE 20070611 14:14 0017657 OA (pdf format)

ECMS NO CM RELEASE 20070611 14:14 0017657 OA (pdf format)

3.0 Damage Model and Off-line Testing

The conventional way of characterizing laser-induced surface damage by experimentally determining the lowest damage threshold for a number of small sites is inadequate for relating the results of off-line damage testing (using small beams) to expected results on a large-aperture system like the NIF. Neither a single damage threshold nor even a damage threshold probability curve from off-line tests is directly applicable to the large-aperture case. This is because damage occurs first at the weakest site on the illuminated area, and larger beams are more likely to find increasingly rare weaker sites (see Figure 3-1). The relevant question is not "will damage occur?" It certainly will on a large aperture. The important question is to quantify what density of damage will occur and to assess its functional significance.

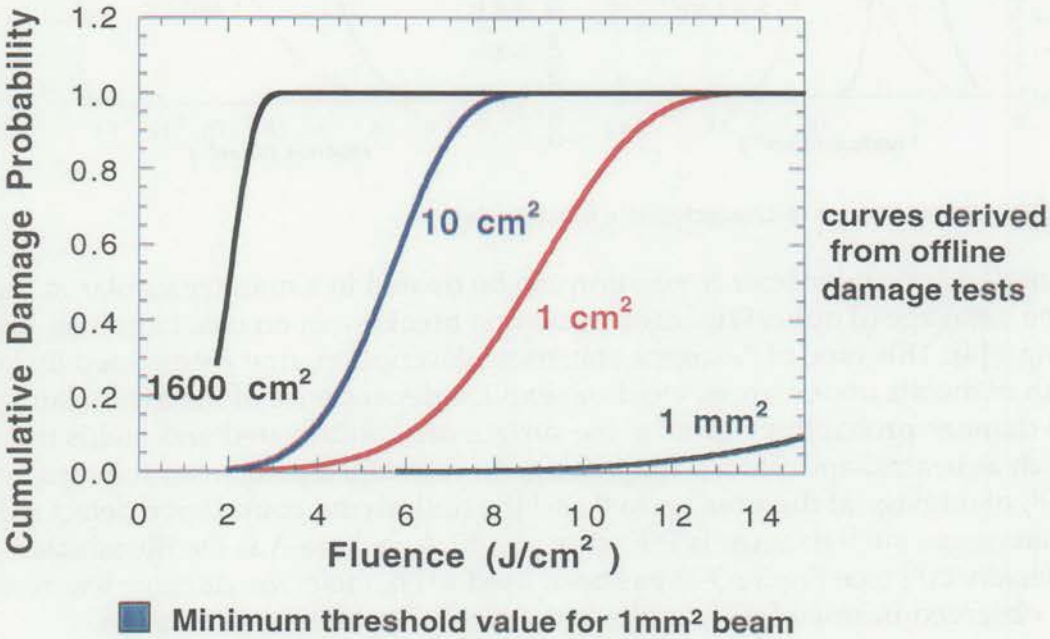

Figure 3-1. Damage probability depends on test area. Neither a single threshold or single probability curve adequately describes both small (test) and large areas.

A statistical model has been developed of laser damage initiation [1–3] that relates the probability curves measured in off-line tests to the underlying density of damage initiating defects (see Figure 3-2). The reader is referred to the references for a more detailed description of the model. Once this expected density is known for a given optic, the extrapolation of test results to larger areas and different beamshapes is straightforward. It is also possible to report the results of different types of damage tests in the same "language." An added benefit of this formulation is that, combined with a model of damage growth upon repeated irradiation, it provides a methodology for estimating the functional implications of laser damage, e.g., the expected number of laser shots at a given fluence level (and for a given fluence distribution including hot spots) to reach a given fraction of obscured area on an optic (lifetime estimation).

ECMS NO CM RELEASE 20070611 14:14 0017657 OA (pdf format)

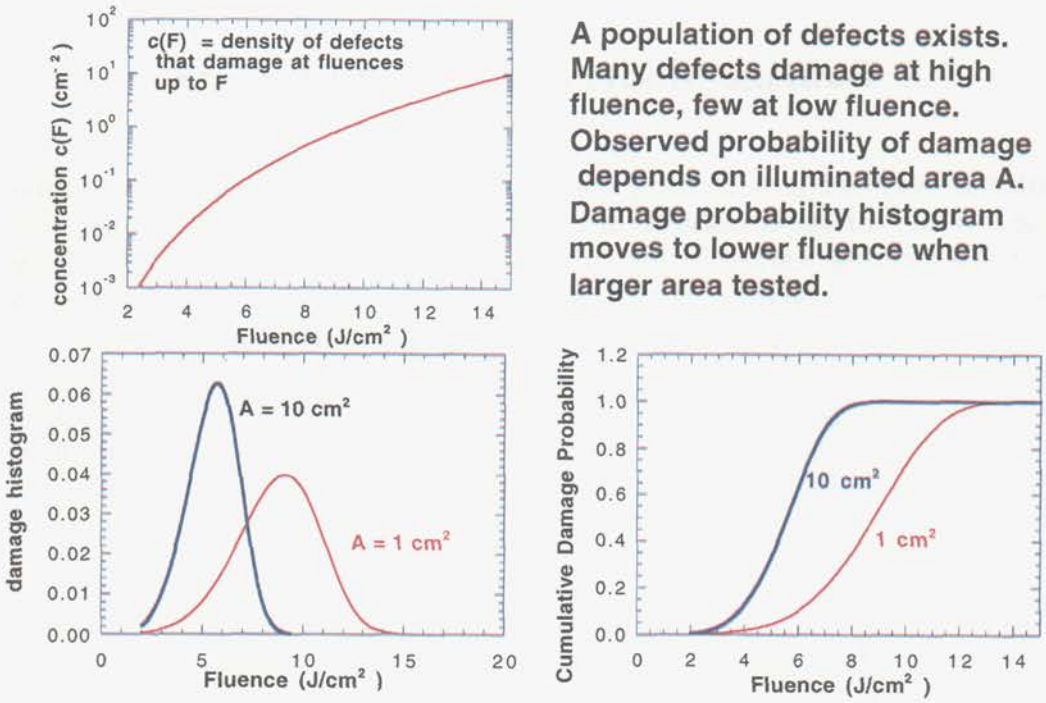

Figure 3-2. Defect concentration is characteristic of material.

Incidence of damage under laser irradiation can be treated in a manner similar to that used, e.g., to describe breakage of optical fibers or insulation breakdown on coaxial cables, both as a function of length[4]. This type of "extreme statistics" description, first formulated by Weibull for the strength of metals under stress, yields an explicit dependence of the mean damage threshold and damage probability curve on the surface area illuminated and yields test parameters such as beamshape. For a flattop beam, the relationship between the measured probability P(F) of damage at fluences up to F and the underlying cumulative defect surface density c(F) that causes such damage is $P(F)=1-\exp(-c(F)\,A)$, where A is the illuminated area. The derived density c(F) (see Figure 3-3) has been used to characterize damage test results to compare with observed Beamlet HDT results and as input for lifetime estimation.

Currently, two types of damage testing are done at LLNL (see Figure 3-4). The Automatic Damage Tester (ADT) tests a number of sites with an approximately 1-mm-diameter beam. At each site, the fluence is increased until damage is observed. The result is a damage probability curve. The Large Aperture Tester (LAT) scans a larger area (typically 10–20 cm^2) with a small beam at a fixed fluence, after which the number of damage sites occurring in the scanned area is counted. When analyzed with the Weibull formalism, the results of both types of test are consistent and comparable (see Figure 3-5). Generally, the expected damage density scales as a power of the fluence. Indeed, a database is being built of such results for lenses, debris shields and diffractive optics plate substrates from potential NIF vendors (see Figures 3-6 to 3-11). Such testing allows quantitative evaluation of effects of processing on damage susceptibility (see Figures 3-7 and 3-8).

ECMS NO CM RELEASE 20070611 14:14 0017657 OA (pdf format)

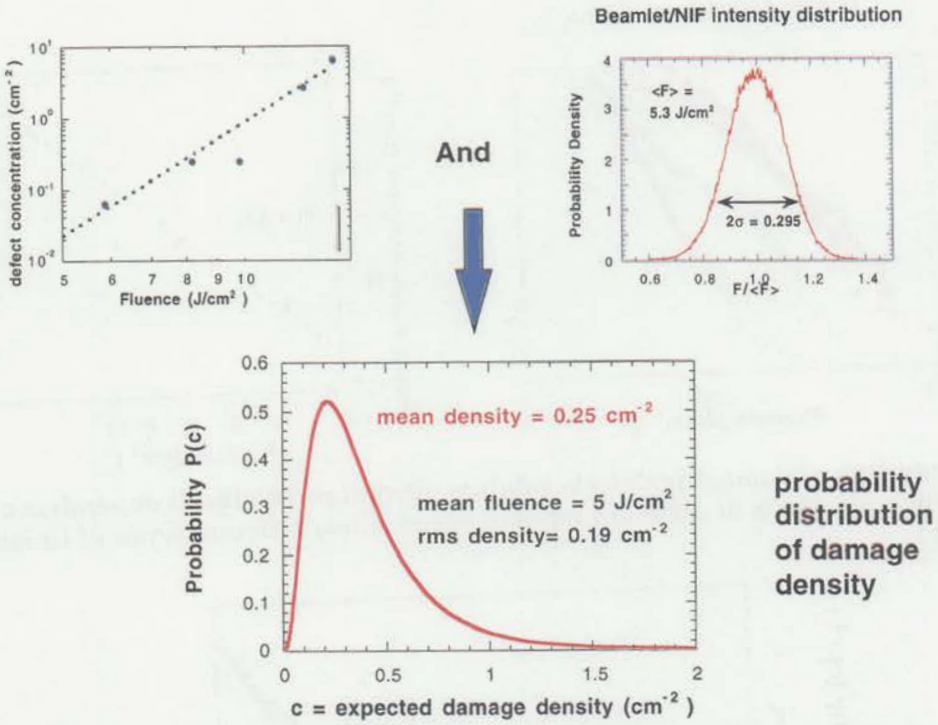

Figure 3-3. Damage test and shot fluence distribution data can be used to calculate expected damage density.

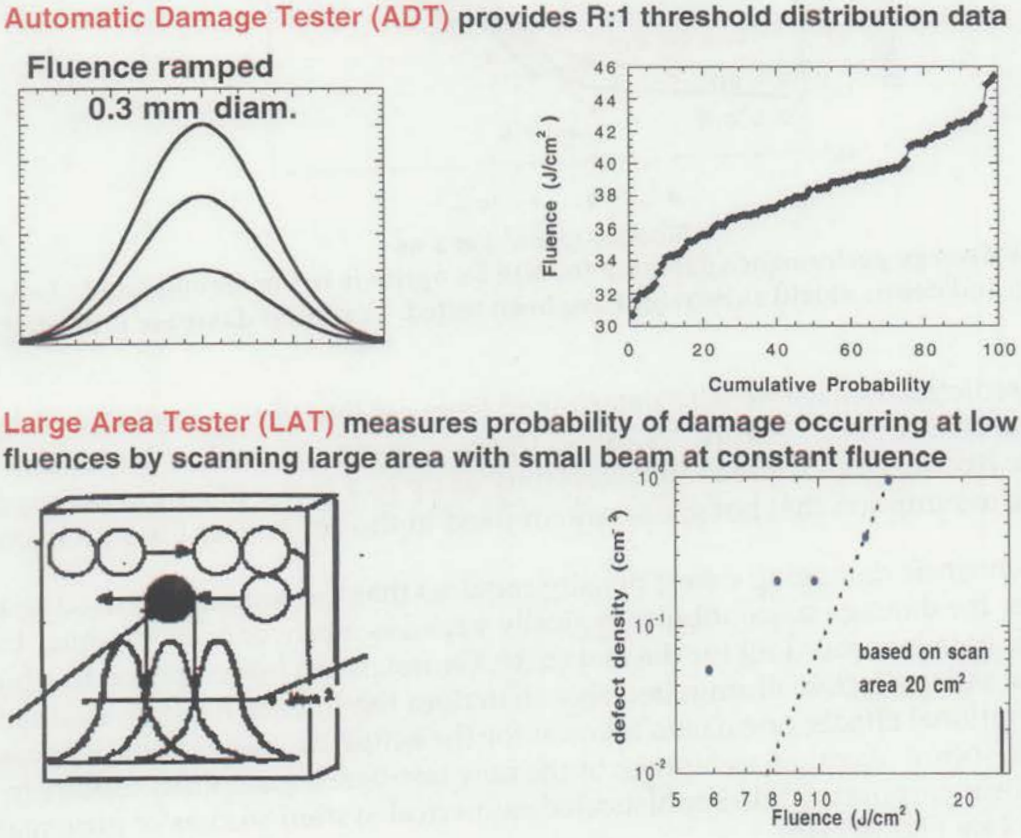

Figure 3-4. Different types of damage tests give different information.

ECMS NO CM RELEASE 20070611 14:14 0017657 OA (pdf format)

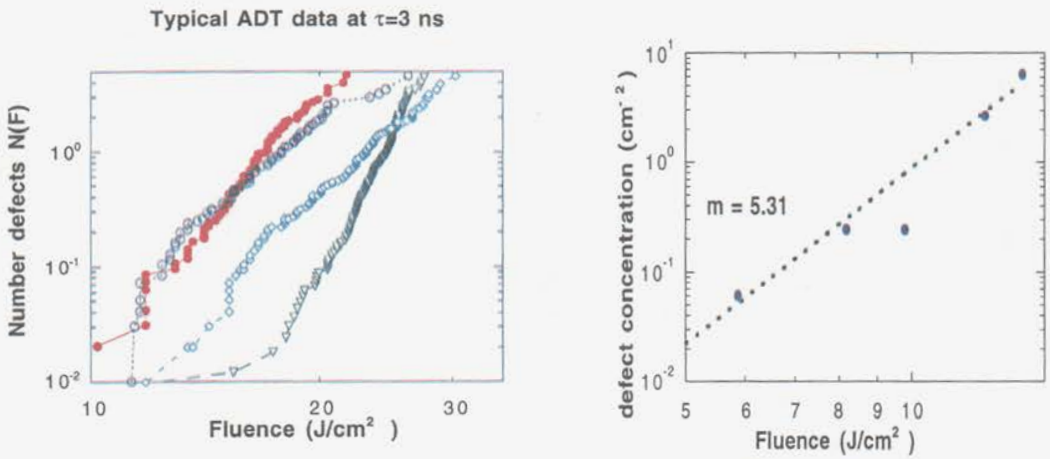

Figure 3-5. Concentration of damaging defects exhibits power law (Weibull) dependence on fluence. Above examples include effects of different types of fused silica, different types of finishing, different test lasers.

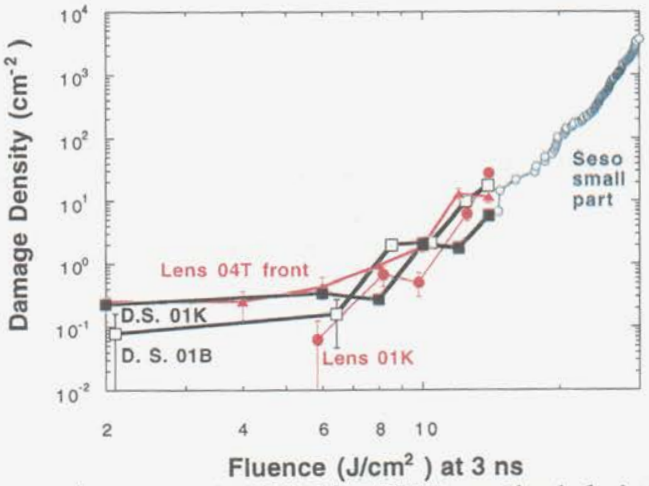

Figure 3-6. A new damage performance database for NIF 3ω optics is being accumulated. Lens, diffractive optics, and debris shield substrates have been tested. A similar database is needed for KDP.

Agreement of predicted damage density determined from off-line testing with that observed on Beamlet is reasonably good. Figure 3-9 shows the two quantities used in the tripler campaign for the Kodak lens. There is an uncertainty of up to a factor of two in the expected values due to the assumption that hot spots remain fixed in the beam over the shot history.

Deriving the intrinsic damaging defect density requires that the beamshape used be taken into account since the damage susceptibility typically varies as a power of the fluence. In the test situation, this entails accounting for the fact that a Gaussian test beam (raised to a high exponent) has a smaller effective illuminated area than does the fluence itself. In evaluating the expected operational effects, one has to account for the actual distribution of fluences over the Beamlet or NIF beam. Another advantage of the new test-based formalism used here is that it can easily be incorporated into sophisticated numerical system studies of propagation through the FOA (see Figure 3-10).

ECMS NO CM RELEASE 20070611 14:14 0017657 OA (pdf format)

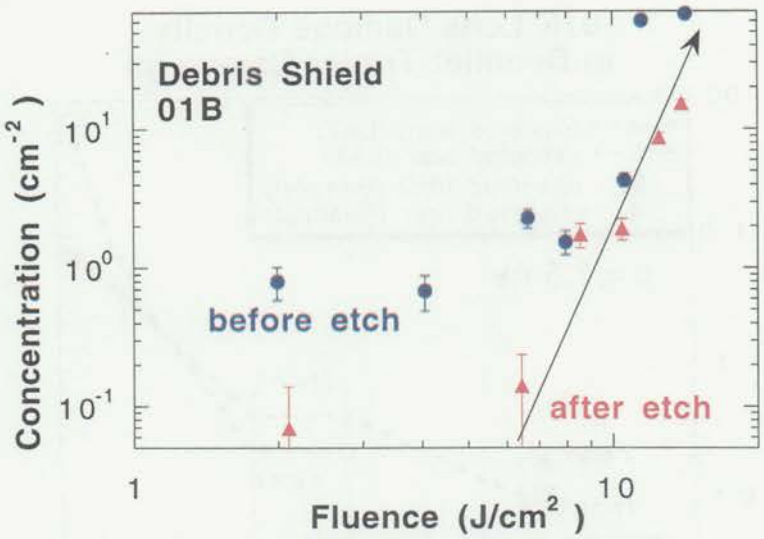

Figure 3-7. Low-fluence damage associated with Ceria polish removed by 600-nm etch. Etch-reduced damage density by more than an order of magnitude at fluences less than 10 J/cm2, after etch results similar to those for 01Z found previously.

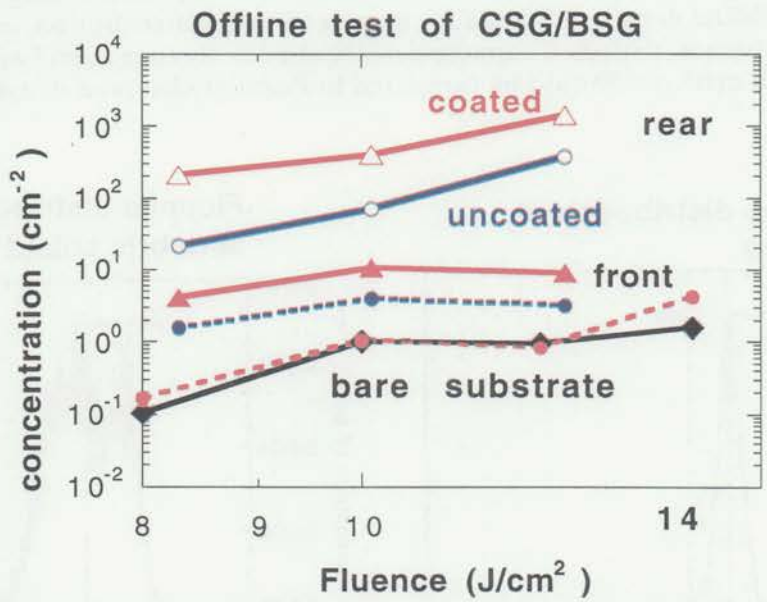

Figure 3-8. Off-line tests aid determination of significant influences on damage behavior. FF lens 01 K and color separation grating were fabricated from"sister" substrates.

The damaging defect density can be used together with a description of damage growth with repeated irradiation to estimate the fraction of an optic obscured by laser damage after a sequence of laser shots (see Figure 3-11). Preliminary experiments indicate that the diameter of the damaged area scales with pulse fluence and the number of shots. Further theoretical and experimental work is necessary to understand how the growth rate varies with environment (vacuum vs air), substrate (fused silica, KDP, coated or uncoated), and type of damage. Larger damage growth rates observed on Beamlet compared to off-line experiments imply a corresponding reduction in lifetime if not ameliorated (see Figure 3-12). Beamlet data imply a range of damage growth rates.

ECMS NO CM RELEASE 20070611 14:14 0017657 OA (pdf format)

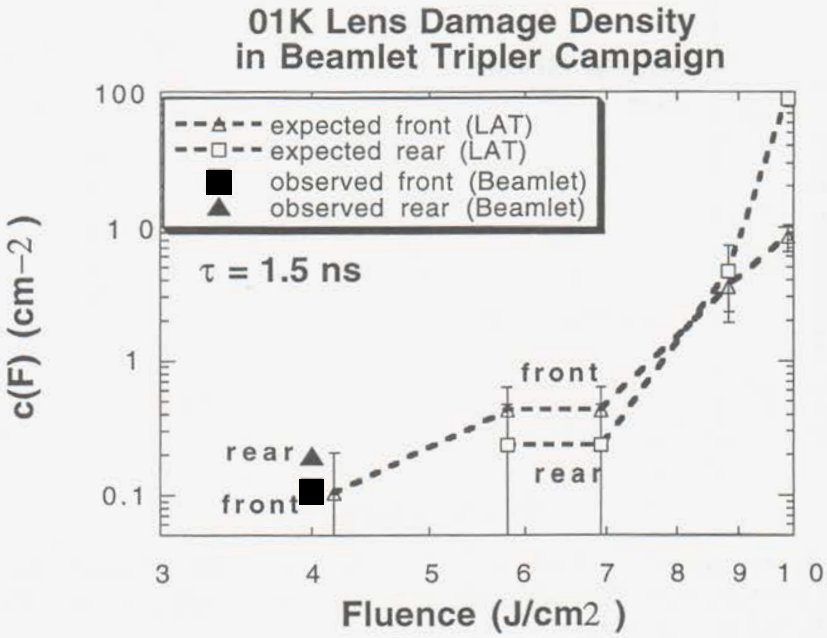

Figure 3-9. Expected damage density on 3ω lens in34-cm Beamlet Tripler Campaign. √τ scaling of fluence was assumed, off-line density adjusted for Beamlet fluence distribution, and Beamlet density plotted at peak fluence. Expected damage density at peak fluence from Large Area Tester (LAT) off-line tests (open markers) should be compared to Beamlet observed density (filled markers).

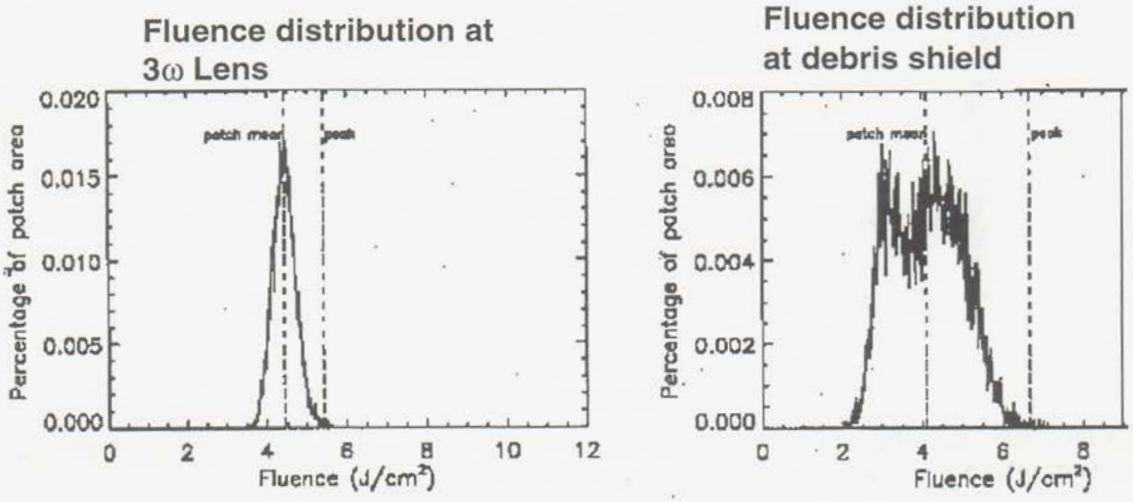

Calculations include measured surface roughness on lens, DOP1, DOP2, and debris shield as well as self focusing. CSG modeled has period of 245 μm.

Figure 3-10. Damage model can be included in sophisticated numerical FOA propagation simulations. Actual fluence distribution varies in FOA due to surface roughness, diffractive optics, and nonlinear diffraction.

The strategy for off-line damage testing requires testing at NIF-relevant 3ω fluences of 6–12 J/cm^2 and over areas large enough to measure the low-probability tail of the damage distribution that is most important for high-quality optics. The relevant area is 10 cm^2 at the larger fluences and 25 cm^2 at the lower fluences for fused silica. A test area of about 50 cm^2 is

ECMS NO CM RELEASE 20070611 14:14 0017657 OA (pdf format)

required to reliably observe the type of surface damage observed on the AR-coated KDP tripler in the HDT2 Beamlet test.

In addition to the presently available LAT off-line tester, it is desirable to have a large beam area test facility in which influences such as environment on damage initiation and growth can be determined. A large beam facility is also desirable for damage testing of diffractive optics so that many grating periods are illuminated. Of the facilities available to the program (OSL, Slab Lab, NOVA), Slab Lab appears the most practical since it offers both a relatively large beam size (1-2 cm^2 and 10 J at 3ω) and a high repetition rate (1 Hz).

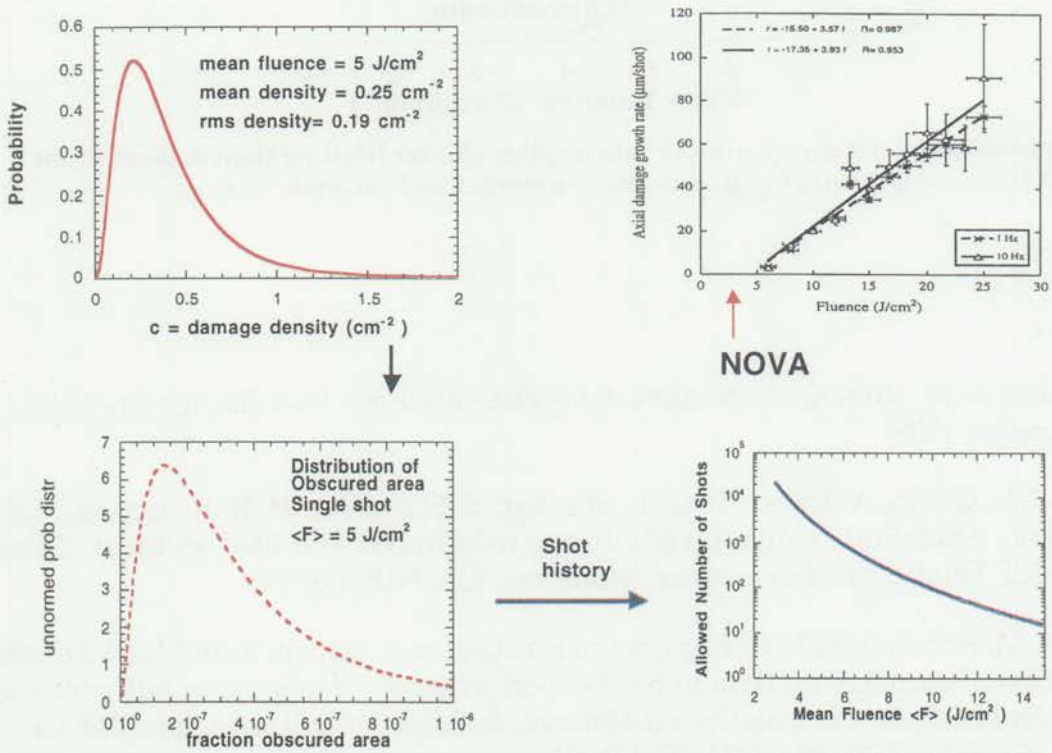

Figure 3-11. Damage density and growth rate can be used to estimate obscuration, and, with shot history, lifetime.

ECMS NO CM RELEASE 20070611 14:14 0017657 OA (pdf format)

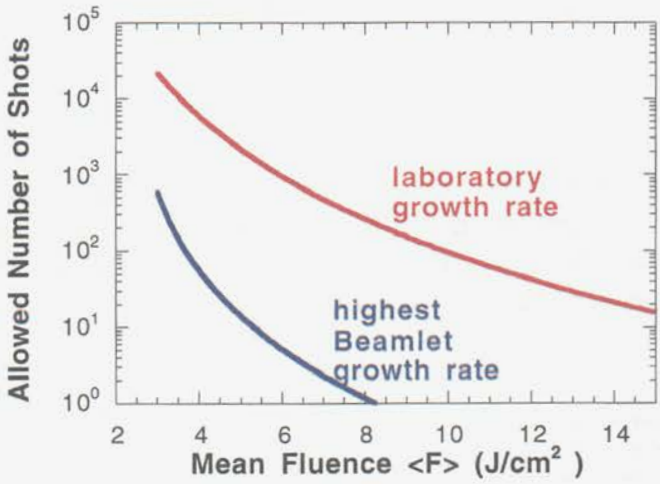

Figure 3-12. Highest Beamlet damage growth rate implies shorter lifetime than derived from intrinsic rate. Differences presumably due to environmental and extrinsic factors.

3.1 References

1. M. D. Feit and A. M. Rubenchik. *Statistical properties of surface laser damage thresholds.*, NIF-0008019 (April 6, 1998).

2. M. D. Feit, F. Y. Génin, A. Rubenchick, L. Sheehan, S. Schwartz, M. R. Kozlowski, J. Dijon , and P. Garrec, "Statistical evaluation of damage risks in NIF and LMJ optics at 355 nm," *1998 SSLA-ICF Third Annual Conference*, Monterey, CA, NIF-0010149.

3. M.D. Feit, A.M. Rubenchik, M.R. Kozlowski, F.Y. Génin, S. Schwartz and L.M. Sheehan, "Extrapolation of damage test data to predict performance of large-area NIF optics at 355 nm," *XXX Annual Symposium on Optical Materials for High-Power Lasers*, Boulder, Co, Sept. 28–Oct. 1, 1998, SPIE-3578-48 UCRL-JC-131222.

4. R. Olshansky and R.D. Maurer, "Mechanical strength and fatigue of optical fibers", *J. of Appl. Phys.* **47**, 4497, (1976).; l. Simoni, G. Mazzanti, G. Montano, "Electrical breakdown of insulating materials and structures," *Size-scale Effects in the Failure Mechanisms of Materials and Structures*, edited by A. Carpinteri, (E&FN Spon, Chapman and Hall, London, 1996).

ECMS NO CM RELEASE 20070611 14:14 0017657 OA (pdf format)

4.0 High-Fluence Operation of KD*P on Beamlet

4.1 Abstract

Recent high-fluence operation of a prototype final optics cell in the Beamlet FOA test mule caused unacceptable damage to the KD*P tripler. The damage occurred on the output surface of the crystal at approximately 50 sites, a few of which grew to cm scale after repeated exposure to 3ω fluences of ~7.8 J/cm^2 in a 3-ns-square pulse. This result contrasts sharply with previous Beamlet experience in which AR-coated crystals tested in air, and uncoated crystals tested in vacuum, sustained negligible surface damage at similar and higher fluences. A question concerning the recent experiment involves the quality of the tripler AR coating, which exhibited very poor transmission even prior to use; it remains to be determined if and how this factor influenced the damage. Examination of high-resolution near-field photographs reveals that at least some of the damage originated at small, as-yet unidentified precursors that were visibly present on the very first (low-power) shot.

4.2 Introduction

There have been five high-fluence 3ω campaigns conducted on Beamlet, the chronology and essential features of which are outlined in Table 4-1. The shot history of the average 3ω fluences in these campaigns is plotted in Figure 4-1. The purpose of this report is to review the various configurations and conditions of these tests and to summarize the results in the context of KD*P surface damage. In addition to the full-aperture Beamlet tests, there have been several subaperture tests of bare KDP and bare KD*P at high 3ω fluence in both air and vacuum. These tests are summarized in Table 4-2. In all of the subaperture tests, post-test visual and microscopic inspection of samples gave no definitive indications of laser-induced surface damage, despite low levels of particulates and digs [1].

ECMS NO CM RELEASE 20070611 14:14 0017657 OA (pdf format)

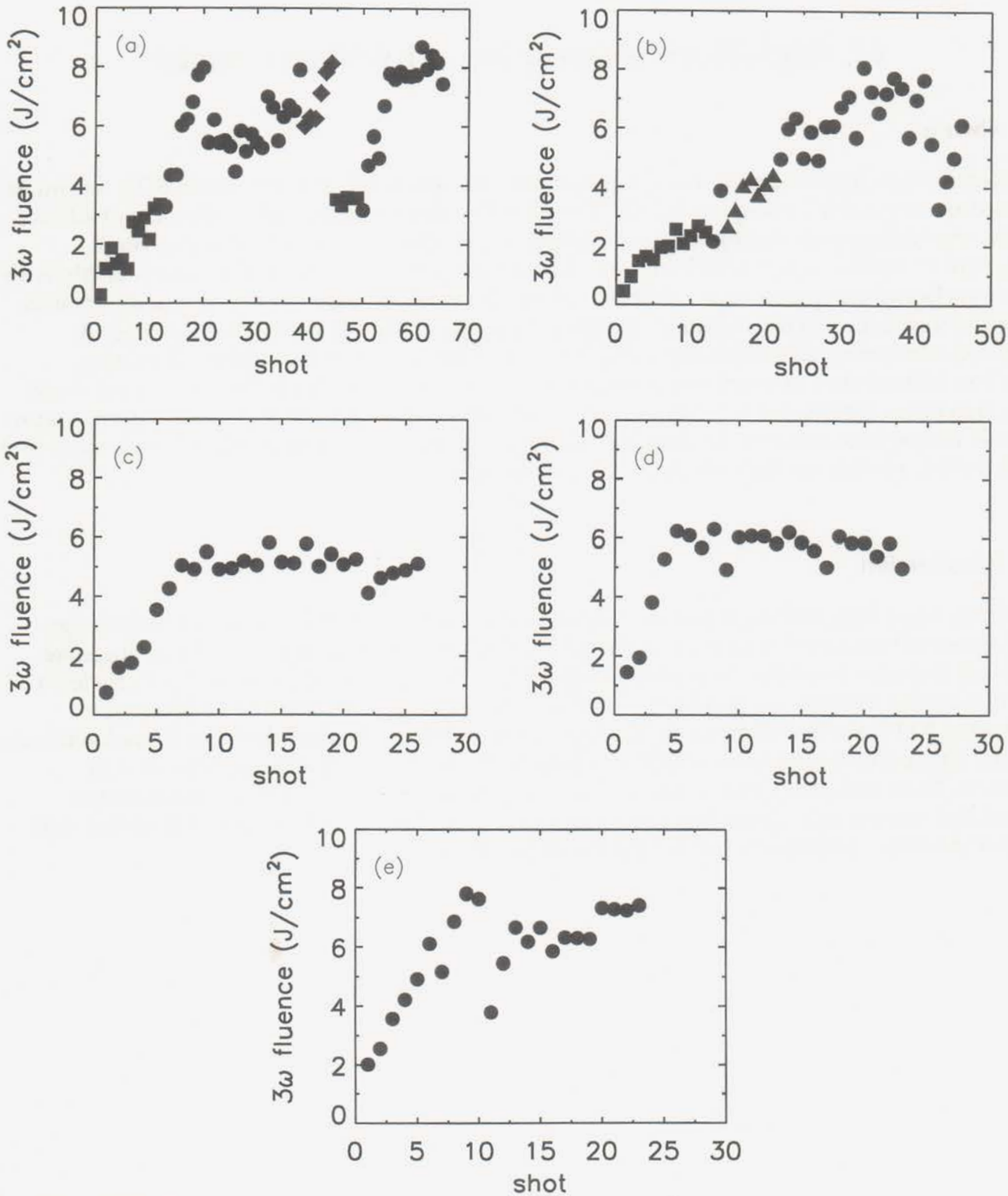

Figure 4-1. Shot fluence histories for the five high-fluence 3ω Beamlet campaigns: (a) 32-cm activation, (b) 37-cm activation, (c) MDT, (d) HDTI, and (e) HDTII. Squares, triangles, circles, and diamonds denote pulse formats of 1-ns square, 1.7-ns square, 3-ns square, and 10-ns shaped, respectively.

ECMS NO CM RELEASE 20070611 14:14 0017657 OA (pdf format)

Table 4-1. Summary of Beamlet high-fluence 3ω campaigns (full aperture).

Campaign	Date	Beam size cm^2	Pulse	# shots	3ω fluence* J/cm^2	Optics
32-cm THG activation	8/2/94 to 10/7/94	740	1 ns sq 3 ns sq 10 ns NIF	14 43 6	3.6 8.7 8.1	air
37-cm THG activation	3/16/95 to 4/3/95	1030	1 ns sq 1.7 ns sq 3 ns sq	12 7 27	2.7 4.3 8.1	air
Baseline changed to 1ω vacuum barrier, 1996						
FOA test mule MDT	1/6/98 to 1/21/98	1030	3 ns sq	26	5.7	vacuum
FOA test mule HDTI	5/12/98 to 5/21/98	1030	3 ns sq	23	6.3	vacuum
FOA test mule HDTII	7/21/98 to 7/31/98	785	3 ns sq	23	7.8	vacuum

* maximum fluence in campaign, aperture-averaged at last component

Table 4-2. Summary of high-fluence subaperture tests of bare KDP/KD*P.

Campaign	Date	Type	Beam size cm^2	Pulse	# shots		3ω fluence J/cm^2	Optics
Beamlet	1/9/96 to 2/2/98	N/1 ramp	55	3 ns Gauss.	LL6-15* LL6-16*	1 2	6.7 6.4	vacuum
Beamlet	8/8/96 to 8/19/96	N/1 ramp	85	3 ns Gauss.	LL1-18*	4	11.0	vacuum
OSL	3/24/97 to 5/27/97	N/1 ramp	0.4	3 ns Gauss.	KDP214 DKDP11* LL6-56* KDP328	9 8 9 5	13.4 12.4 12.8 17.8	air

* deuterated material

ECMS NO CM RELEASE 20070611 14:14 0017657 OA (pdf format)

4.3. Beamlet High-Fluence Tests at Air

The first Beamlet high-fluence 3ω campaigns were part of the initial system activation experiments at 32-cm and 37-cm aperture [2] and were conducted with the frequency conversion crystals and auxiliary UV optics fielded at standard atmospheric pressure. As shown in Figure 4-1 and summarized in Tables 4-3 and 4-4, both the 32-cm and 37-cm THG activation campaigns achieved aperture-averaged 3ω fluences of >8 J/cm^2 in a 3-ns square pulse, with 15 to 30 shots each at fluences > 6 J/cm^2. In both cases, negligible surface damage was observed on the KD*P triplers. In the configuration tested, the doubler and tripler were held by their corners in separate gimbals with a spacing between the crystals of 46 cm. Auxiliary UV optics were a 35-mm thick fused-silica splitter located 78 cm downstream of the tripler and a fused-silica beam expansion lens located a further ~700 cm downstream. Both the 32-cm and 37-cm tripler were newly finished crystals, with high-quality sol-gel AR coatings applied shortly before the tests. The 32-cm tripler (80% LL6-14) was finished on 4/26/94, processed and sol-gel AR coated on 6/22/94, and used from 8/2/94 to 10/7/94. This crystal was also used with the same AR coating from 11/22/95 to 2/2/96 during the activation of the focal plane diagnostic at very low fluence. Visual inspection data dated 10/3/94 and 11/22/95 claimed between 5 and 10 damage sites on the second surface of the crystal ranging from 100 μm to less than 500 μm in size [3]. Recent inspection on 9/19/98 identified ~14 sites less than 200 μm in size plus several scratches. The 37-cm tripler (80%LL1-12) was finished on 7/14/94, processed and AR coated on 2/22/95, and used from 3/16/95 to 4/3/95. Since that time it has been reworked several times, on 4/1/96 and 2/20/97. Visual inspection data dated 3/31/95 and 9/27/95 identified no surface damage [4].

ECMS NO CM RELEASE 20070611 14:14 0017657 OA (pdf format)

Table 4-3. Summary of Beamlet 32-cm THG activation campaign.

Shot	Type	Pinholes µrad	SHG µrad	THG (int)	$\Delta\nu$ GHz	$\tau_{1\omega}$** ns	$E_{1\omega}$* J	$I_{1\omega}$ GW/cm^2	$E_{3\omega}$* J	$\eta_{3\omega}$ %	$F_{3\omega}$ J/cm^2
B4080210	1ω, no crystals	200/200			30	1.0	991	1.34			
B4082402	3ω	200/200	250	0	30	1.0	586	0.79	206	35.1	0.28
B4082411	3ω	200/200	250	0	30	1.0	1367	1.85	849	62.1	1.15
B4082414	3ω	200/200	250	0	30	1.0	1900	2.57	1372	72.2	1.85
B4083106	1ω, no crystals	200/200			30	1.0	1480	2.00			
B4083110	3ω	200/200	250	-188	30	1.0	1656	2.24	979	59.1	1.32
B4083114	3ω	200/200	250	236	30	1.0	1923	2.60	1081	56.2	1.46
B4083119	3ω	200/200	200	0	30	1.0	1349	1.82	847	62.8	1.14
B4090107	3ω	200/200	250	0	30	1.0	2710	3.66	2030	74.9	2.74
B4090113	3ω	200/200	250	0	30	1.0	2362	3.19	1809	76.6	2.44
B4090119	3ω	200/200	200	0	30	1.0	3117	4.21	2129	68.3	2.88
B4090202	3ω	200/200	300	0	30	1.0	2614	3.53	1589	60.8	2.15
B4090206	3ω	200/200	225	0	30	1.0	3069	4.15	2369	77.2	3.20
B4090210	3ω	200/200	225	-45	30	1.0	3127	4.23	2461	78.7	3.33
B4090702	3ω	200/200	225	-50	30	3.0	3804	1.71	2412	63.4	3.26
B4090705	3ω	200/200	225	-50	30	3.0	4579	2.06	3201	69.9	4.33
B4090708	3ω	200/200	225	-50	30	3.0	4579	2.06	3210	70.1	4.34
B4090802	3ω	200/200	225	-50	30	3.0	5789	2.61	4440	76.7	6.00
B4090808	3ω	200/200	225	-50	30	3.0	5973	2.69	4599	77	6.22
B4090812	3ω	200/200	225	-50	30	3.0	6466	2.91	5037	77.9	6.81
B4090816	3ω	200/200	232	-50	30	3.0	7095	3.20	5719	80.6	7.73
B4090914	3ω	200/200	232	-50	30	3.0	7386	3.33	5901	79.9	7.97
B4091304	3ω	200/200	232	-50	30	3.0	5411	2.44	4020	74.3	5.43
B4091406	3ω	200/200	232	-50	30	3.0	6069	2.73	4588	75.6	6.20
B4091416	3ω	200/200	232	-50	30	3.0	5382	2.42	4010	74.5	5.42
B4091506	3ω	200/200	232	-50	30	3.0	5518	2.49	4061	73.6	5.49
B4091515	3ω	200/200	232	-50	30	3.0	5334	2.40	3920	73.5	5.30
B4091619	3ω	200/200	232	-50	30	3.0	4724	2.13	3293	69.7	4.45
B4091905	3ω	200/200	232	-50	30	3.0	5944	2.68	4303	72.4	5.82
B4091922	3ω	200/200	232	-50	30	3.0	5227	2.35	3800	72.7	5.14
B4092003	3ω	200/200	232	-50	30	3.0	5769	2.60	4229	73.3	5.71
B4092009	3ω	200/200	232	-50	30	3.0	5537	2.49	4020	72.6	5.43
B4092017	3ω	200/200	232	-50	30	3.0	5314	2.39	3890	73.2	5.26
B4092204	3ω	200/200	232	-50	30	3.0	6824	3.07	5173	75.8	6.99
B4092208	3ω	200/200	232	-50	30	3.0	6573	2.96	4903	74.6	6.63
B4092211	3ω	200/200	232	0	30	3.0	5614	2.53	4059	72.3	5.49
B4092214	3ω	200/200	232	-50	30	3.0	6157	2.77	4661	75.7	6.30
B4092304	3ω	200/200	232	-50	30	3.0	6418	2.89	4961	77.3	6.70
B4092308	3ω	200/200	232	-50	30	3.0	6563	2.96	4817	73.4	6.51
B4092312	3ω	200/200	232	-50	30	3.0	7347	3.31	5848	79.6	7.90

* 1ω energy at input to converter, 3ω energy at output of converter

** nominal pulse width

ECMS NO CM RELEASE 20070611 14:14 0017657 OA (pdf format)

Table 4-3. Summary of Beamlet 32-cm THG activation campaign (cont.).

Shot	Type	Pinholes μrad	SHG μrad	THG (int)	Δν GHz	$\tau_{1\omega}$** ns	$E_{1\omega}$* J	$I_{1\omega}$ GW/cm²	$E_{3\omega}$* J	$\eta_{3\omega}$ %	$F_{3\omega}$ J/cm²
B4092703	3ω, shaped	200/200	232	-50	30	10.0	7521	-	4430	58.9	5.99
B4092706	3ω, shaped	200/200	232	-50	30	10.0	7928	-	4654	58.7	6.29
B4092711	3ω, shaped	200/200	232	-50	30	10.0	7589	-	4614	60.8	6.24
B4092804	3ω, shaped	200/200	232	-50	30	10.0	8528	-	5270	61.8	7.12
B4092808	3ω, shaped	200/200	232	-50	30	10.0	9206	-	5800	63.0	7.84
B4092903	3ω, shaped	200/200	232	-50	30	10.0	9177	-	6002	65.4	8.11
B4092914	3ω	200/200	232	-50	30	1.0	3582	4.84	2590	72.3	3.50
B4093007	3ω	200/200	232	-50	30	1.0	3127	4.23	2452	78.4	3.31
B4093015	3ω	200/200	232	-50	30	1.0	3601	4.87	2650	73.6	3.58
B4093024	3ω	200/200	232	-50	30	1.0	4172	5.64	2620	62.8	3.54
B4093027	3ω	200/200	232	-50	30	1.0	3969	5.36	2639	66.5	3.57
B4100303	3ω	200/200	232	-50	30	3.0	3824	1.72	2329	60.9	3.15
B4100307	3ω	200/200	232	-50	30	3.0	4947	2.23	3453	69.8	4.67
B4100404	3ω	200/200	232	-50	30	3.0	5702	2.57	4180	73.3	5.65
B4100408	3ω	200/200	232	-50	30	3.0	5256	2.37	3642	69.3	4.92
B4100413	3ω	200/200	232	-50	30	3.0	6689	3.01	4950	74.0	6.69
B4100504	3ω	200/200	232	-50	30	3.0	7579	3.41	5760	76.0	7.78
B4100507	3ω	200/200	232	-50	30	3.0	7396	3.33	5621	76.0	7.60
B4100510	3ω	200/200	232	-50	30	3.0	7521	3.39	5799	77.1	7.84
B4100517	3ω	200/200	237	-40	30	3.0	7279	3.28	5707	78.4	7.71
B4100603	3ω	200/200	237	-40	30	3.0	7357	3.31	5702	77.5	7.70
B4100606	3ω	200/200	237	-40	30	3.0	7376	3.32	5731	77.7	7.74
B4100612	3ω	200/200	232	-40	30	3.0	8402	3.78	6428	76.5	8.69
B4100616	3ω	200/200	232	-60	30	3.0	7686	3.46	5872	76.4	7.94
B4100701	3ω	200/200	232	-35	30	3.0	8247	3.71	6218	75.4	8.40
B4100705	3ω	200/200	232	-50	30	3.0	7909	3.56	6042	76.4	8.17
B4100708	3ω	200/200	232	-50	30	3.0	7270	3.27	5511	75.8	7.45
B4100714	3ω	200/200	232	-50	30	3.0	8141	3.67	6114	75.1	8.26

* 1ω energy at input to converter, 3ω energy at output of converter

** nominal pulse width

ECMS NO CM RELEASE 20070611 14:14 0017657 OA (pdf format)

Table 4-4. Summary of Beamlet 37-cm THG activation campaign.

Shot	Type	Pinholes µrad	SHG µrad	THG (int)	Δν GHz	$\tau_{1\omega}$** ns	$E_{1\omega}$* J	$I_{1\omega}$ GW/cm²	$E_{3\omega}$* J	$\eta_{3\omega}$ %	$F_{3\omega}$ J/cm²
B5031615	3ω	200/200	249	-78	30	1.0	1094	1.06	475	43.4	0.46
B5031618	3ω	200/200	249	-78	30	1.0	1810	1.76	974	53.8	0.95
B5031703	3ω	200/200	249	-78	30	1.0	2691	2.61	1520	56.5	1.48
B5031706	3ω	200/200	249	-78	30	1.0	2817	2.73	1679	59.6	1.63
B5031710	3ω	200/200	249	-78	30	1.0	2488	2.42	1570	63.1	1.52
B5031713	3ω	200/200	202	-78	30	1.0	2672	2.59	2001	74.9	1.94
B5031802	3ω	200/200	202	-59	30	1.0	2817	2.73	2040	72.4	1.98
B5032003	3ω	200/200	202	-59	30	1.0	3572	3.47	2640	73.9	2.56
B5032006	3ω	200/200	227	-59	30	1.0	3185	3.09	2131	66.9	2.07
B5032010	3ω	200/200	177	-59	30	1.0	3524	3.42	2410	68.4	2.34
B5032013	3ω	200/200	192	-59	30	1.0	3969	3.85	2758	69.5	2.68
B5032102	3ω	200/200	212	-59	30	1.0	3727	3.62	2542	68.2	2.47
B5032203	3ω	200/200	202	-59	30	3.0	4124	1.33	2210	53.6	2.15
B5032206	3ω	200/200	202	-59	30	3.0	6108	1.98	3989	65.3	3.87
B5032210	3ω	200/200	202	-59	30	1.7	3746	2.14	2648	70.7	2.57
B5032214	3ω	200/200	202	-59	30	1.7	4579	2.62	3219	70.3	3.13
B5032302	3ω	200/200	202	-59	30	1.7	5673	3.24	4073	71.8	3.95
B5032305	3ω	200/200	202	-59	30	1.7	6399	3.65	4319	67.5	4.19
B5032308	3ω	200/200	202	-59	30	1.7	5305	3.03	3751	70.7	3.64
B5032325	3ω	200/200	202	-59	30	1.7	6195	3.54	4107	66.3	3.99
B5032408	3ω	200/200	192	-59	30	1.7	6389	3.65	4453	69.7	4.32
B5032413	3ω	200/200	192	-59	30	3.0	7328	2.37	5108	69.7	4.96
B5032416	3ω	200/200	197	-59	30	3.0	8664	2.80	6169	71.2	5.99
B5032419	3ω	200/200	187	-59	30	3.0	9022	2.92	6532	72.4	6.34
B5032702	3ω	200/200	202	-59	30	3.0	7541	2.44	5143	68.2	4.99
B5032705	3ω	200/200	197	-109	30	3.0	8567	2.77	6057	70.7	5.88
B5032709	3ω	200/200	197	-8	30	3.0	7531	2.44	5068	67.3	4.92
B5032714	3ω	200/200	202	-59	30	3.0	8857	2.87	6253	70.6	6.07
B5032809	3ω	200/200	207	-59	30	3.0	9128	2.95	6271	68.7	6.09
B5032813	3ω	200/200	202	-59	30	3.0	10067	3.26	6946	69.0	6.74
B5032816	3ω	200/200	207	-59	30	3.0	11519	3.73	7315	63.5	7.10
B5032819	3ω	200/200	243	-59	30	3.0	10745	3.48	5867	54.6	5.70
B5032902	3ω	200/200	187	-59	30	3.0	11713	3.79	8328	71.1	8.09
B5032908	3ω	200/200	172	-59	30	3.0	10551	3.41	7491	71.0	7.27
B5032911	3ω	200/200	152	-59	30	3.0	9448	3.06	6736	71.3	6.54
B5033003	3ω	200/200	131	-59	30	3.0	10938	3.54	7427	67.9	7.21
B5033006	3ω	200/200	179	-59	30	3.0	11132	3.60	7971	71.6	7.74
B5033009	3ω	200/200	179	-185	30	3.0	10842	3.51	7622	70.3	7.40
B5033012	3ω	200/200	179	93	30	3.0	10067	3.26	5879	58.4	5.71
B5033102	3ω	200/200	179	-107	30	3.0	10164	3.29	7196	70.8	6.99
B5033105	3ω	200/200	179	-107	30	3.0	10938	3.54	7897	72.2	7.67
B5033108	3ω	200/200	179	-107	30	3.0	7860	2.54	5659	72.0	5.49
B5040302	3ω	200/200	179	-107	30	3.0	5305	1.72	3379	63.7	3.28
B5040305	3ω	200/200	179	-107	30	3.0	6302	2.04	4342	68.9	4.22
B5040308	3ω	200/200	179	-107	30	3.0	7550	2.44	5157	68.3	5.01
B5040311	3ω	200/200	179	-107	30	3.0	9486	3.07	6318	66.6	6.13

* 1ω energy at input to converter, 3ω energy at output of converter

** nominal pulse width

ECMS NO CM RELEASE 20070611 14:14 0017657 OA (pdf format)

4.4 Beamlet High-Fluence Tests at Vacuum: MDT, HDTI

With the change in the NIF baseline to a 1ω vacuum barrier in 1996, subsequent high-fluence campaigns on Beamlet were conducted with the frequency converter crystals and the fused-silica 3ω optics located in the vacuum environment of the Beamlet FOA test mule. The first campaign in this series tested a NIF-like FOC for 20 shots at an average fluence of 5.1 J/cm^2 [5], and generated the first laser-induced surface damage to KD*P observed on Beamlet. The shot summary for this campaign is provided in Table 4-5. The cell contained an 11-mm KDP doubler (328-4), a 9.5-mm KD*P tripler (80%LL1-12), and a medium damage threshold lens (MDT 02T) in a close-packed arrangement with a crystal-to-crystal spacing of 30 mm and crystal-to-lens spacing of 20 mm. All of the components in the cell were sol-gel AR coated. On-line inspection of the components was performed after the 7th and 18th shots. A visual inspection map of the components after the 7th shot and dated 1/13/98 (Figure 4-2) identified at least five damage sites on the second surface of the tripler that had clearly spalled debris on the input surface of the lens. Micrographs of one of the sites showed it was 500 μm in diameter; the same site photographed after eleven subsequent shots at 5 J/cm^2 had grown to 750 μm. Visual inspection data prior to the campaign indicated the presence of small "random pits" on the output surface [6], but the data is of insufficient quality to identify these as precursors to the damage.

Table 4-5. Summary of Beamlet MDT campaign.

Shot	Type	Pinholes μrad	SHG μrad	THG (int)	Δν GHz	fwhm ns	$E_{1\omega}$* J	$I_{1\omega}$ GW/cm^2	$E_{3\omega}$* J	$\eta_{3\omega}$ %	$F_{3\omega}$ J/cm^2
B8010602	1ω, calibration	200/150	-1100	1100	30		931		0	0.0	0.00
B8010605	1ω, calibration	200/150	-1100	1100	30	3.24	996	0.30	0	0.0	0.00
B8010702	2ω, calibration	200/150	0	1100	30	3.04	1046	0.33	0	0.0	0.00
B8010802	2ω, calibration	200/150	0	1100	30	3.18	1022	0.31	0	0.0	0.00
B8010805	3ω, ramp	200/150	-240	0	30	3.39	2405	0.69			
B8010808	3ω, ramp	200/150	-240	0	30	3.36	2356	0.68			
B8010903	3ω, ramp	200/150	-240	200	30	3.36	2372	0.69	781	32.9	0.76
B8010907	3ω, ramp	200/150	-240	200	30	3.37	3561	1.03	1637	46.0	1.59
B8010910	3ω, ramp	200/150	-240	200	30	3.34	3776	1.10	1799	47.6	1.75
B8011203	3ω, ramp	200/150	-240	200	30	3.39	4459	1.28	2354	52.8	2.29
B8011207	3ω, ramp	200/150	-240	200	30	3.39	5921	1.70	3641	61.5	3.53
B8011303	3ω, ramp	200/150	-240	200	30	3.39	6786	1.94	4383	64.6	4.26
B8011307	3ω	200/150	-240	200	30	3.32	7685	2.25	5196	67.6	5.04
B8011402	3ω	200/150	-240	200	30	3.39	7450	2.13	5055	67.9	4.91
B8011405	3ω	200/150	-240	200	30	3.41	8142	2.32	5656	69.5	5.49
B8011408	3ω	200/150	-240	200	30	3.39	7447	2.13	5055	67.9	4.91
B8011503	3ω	200/150	-240	200	30	3.43	7581	2.15	5090	67.1	4.94
B8011508	3ω	200/150	-240	200	30	3.39	7923	2.27	5338	67.4	5.18
B8011513	3ω	200/150	-240	200	30	3.39	7730	2.21	5196	67.2	5.04
B8011062	3ω	200/150	-240	200	30	3.44	8628	2.44	5974	69.2	5.80
B8011605	3ω	200/150	-240	200	30	3.41	7766	2.21	5303	68.3	5.15
B8011608	3ω	200/150	-240	200	30	3.43	7745	2.19	5267	68.0	5.11
B8012003	3ω	200/150	-240	200	30	3.36	8557	2.47	5939	69.4	5.77
B8012006	3ω	200/150	-240	200	30	3.43	7570	2.14	5161	68.2	5.01
B8012105	3ω	200/150	-240	200	30	3.41	8105	2.31	5585	68.9	5.42
B8012109	3ω	200/150	-240	200	30	3.44	7641	2.16	5232	68.5	5.08
B8012112	3ω	200/150	-240	200	30	3.41	7809	2.22	5409	69.3	5.25

* 1ω energy at input to converter (corrected for ASE), 3ω energy at ouput of last optic

ECMS NO CM RELEASE 20070611 14:14 0017657 OA (pdf format)

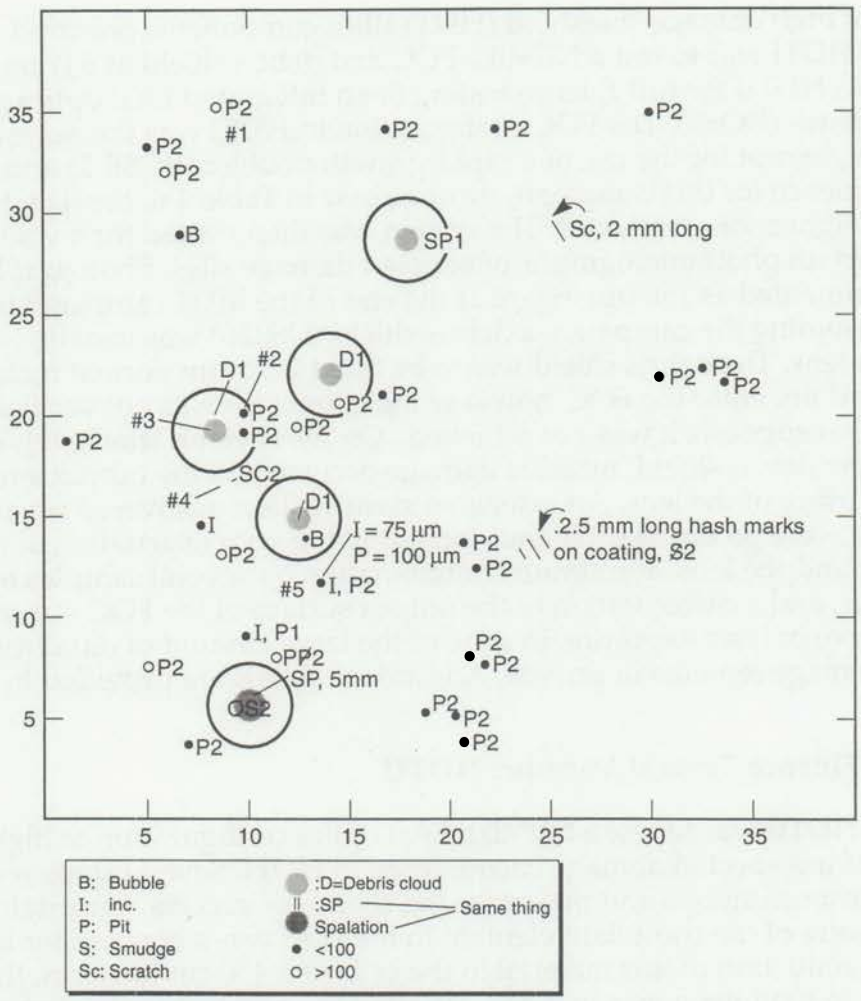

Figure 4-2. Visual inspection map of the components after the 7th shot in the Beamlet MDT campaign. At least five damage sites on the second surface of the tripler were identified (enclosed in circles).

The tripler used in the MDT campaign was the same crystal used in the 37-cm THG activation campaign, but in this case it was not a newly finished and AR-coated crystal. The crystal was reworked on 2/20/97, processed, and sol-gel coated on 6/29/97, used from 7/15/97 to 8/29/97 in the first phase of the FOA test mule experiments, and then reused from 1/6/8 to 1/23/98 in the MDT campaign. By the end of the MDT campaign, the crystal had had the same AR coating for 11 months. The 3ω transmission through the crystal after coating was 95.2%, consistent with expected transmission values for the 3ω AR coating on S_2 and the 1ω/2ω compromise AR coating on S_1. By the end of the MDT campaign, the aperture-averaged 3ω transmission through the crystal had decreased to 90.2%. Part of this loss may be attributed to the operation of the sol-gel coating in vacuum. For example, data has been obtained on Beamlet that clearly shows how exposure to the vacuum environment of the test mule modified the AR properties of a sol-gel coating on a fused silica window [7]. Another potential area of concern that remained undiscovered until several months after this campaign was due to an error in the design of the prototype cell, which provided only a small cross sectional area (~0.02 cm^2) for evacuating the volume between the tripler and the lens.

ECMS NO CM RELEASE 20070611 14:14 0017657 OA (pdf format)

The first tests of high damage-threshold (HDT) silica components occurred in Beamlet HDTI. The goal of HDTI was to test a NIF-like FOC and debris shield at 6 J/cm^2 for 20 shots, and then proceed to HDTII for full-fluence testing of an integrated final optics package with diffractive optics plates (DOPs). The FOC configuration in HDTI was the same as that used in the MDT campaign, except for the use of a rapid-growth doubler (RG8B-2) and an HDT lens (04T). The shot sequence for this campaign, summarized in Table 4-6, consisted of a five-shot ramp followed by eight shots at 6 J/cm^2. The system was then vented for a visual inspection of the optics and to obtain photomicrographs of selected damage sites. Photographs showed that the tripler site documented as 750 um in size at the end of the MDT campaign had grown to 1.5 mm. Prior to resuming the campaign, a debris shield (DS02B) was installed 42.4 cm downstream of the lens. The debris shield was to be tilted 22° from normal incidence to ensure that its reflection did not enter the FOC, however the correct tilt was not verified, and there is indirect evidence that suggests it was not achieved. On the seventh shot at 6 J/cm^2 following the installation of the debris shield, massive damage occurred on the output surface of the tripler and input surface of the lens. An extensive investigation uncovered several aspects of the experiment that were potential problems, including the poor evacuation of the volume between the tripler and the lens, aluminum contamination on several samples of the output surface of the tripler, and a discoloration of the output surface of the FOC not covered by the cap flange, suggestive of laser exposure. In spite of the large amount of data from this analysis, the source of the damage remains unproven. Additional details are provided in Appendix B.

4.5 Beamlet High-Fluence Tests at Vacuum: HDTII

The purpose of HDTII was to test a NIF-like final optics configuration at high fluence while avoiding the type of unexpected damage encountered in HDTI. Several steps were taken to improve previous test conditions and maximize the chance of success. Uncertainty about whether laser exposure of the compliant element in the FOC was a contributor to the HDTI damage lead to the reduction of this material in the cell from 430 cm to 18 cm, the bare minimum required to hold the optics in place. This had the additional effect of increasing the cross-sectional area for evacuating the volume between the tripler and lens to 4.5 cm^2. For HDTI, the FOC and IOM components were CO_2 spray-cleaned and ethanol wiped prior to assembly. For HDTII, the FOC and IOM components were washed in a commercial detergent and high-pressure rinsed with water in a cleaning procedure designed to simulate NIF as closely as possible, and then baked overnight at 200°C in a nitrogen-purged oven (the FOC itself was not baked). Unfortunately, this procedure failed to yield acceptable cleanliness as evidenced by a black residue on swipes of the parts after the bake out. Analysis of the residue identified metal silicates, suggestive of detergent. Subsequent cleaning of each part up to five times using a lint-free cloth soaked with ethanol was required to remove this residue (subsequent tests on other parts indicate this ethanol procedure may have recontaminated the baked parts with plasticizers and a bacteriocide [8]). Inside the FOA test mule, special care was taken to ensure that the numerous back-reflections and ghosts from the debris shield and DOPs were blocked or absorbed. The beam dumps for this purpose, with the exception of those on the inside of the FOC and cap flange, were fashioned from NG-absorbing glass held onto aluminum backing plates with clips. The absorbing glass on the inside of the FOC and cap flange was held in place with Torr Seal, as was the case in HDTI. Another difference between experiments was the beam size, which was scaled down to 30 cm for HDTII to provide a large unexposed region on the optics for post campaign testing. The shot summary for this campaign is shown in Table 4-7.

ECMS NO CM RELEASE 20070611 14:14 0017657 OA (pdf format)

Table 4-6. Summary of Beamlet HDTI campaign.

Shot	Type	Pinholes µrad	SHG µrad	THG (int)	Δν GHz	fwhm ns	$E_{1\omega}$* J	$I_{1\omega}$ GW/cm²	$E_{3\omega}$* J	$\eta_{3\omega}$ %	$F_{3\omega}$ J/cm²
B8051206	3ω, ramp	200/150	-250	0	30	3.02	3264	1.05	1476	45.2	1.43
B8051209	3ω, ramp	200/150	-250	0	30	3.13	3883	1.20	1975	50.9	1.92
B8051218	3ω, ramp	200/150	-250	0	30	3.15	6028	1.86	3875	64.3	3.76
B8051333	3ω, ramp	200/150	-250	0	30		7882		5382	68.3	5.23
B8051405	3ω	200/150	-250	0	30	3.13	8995	2.79	6348	70.6	6.16
B8051412	3ω	200/150	-250	0	30	3.18	8878	2.71	6210	69.9	6.03
B8051419	3ω	200/150	-250	0	30	3.17	8317	2.55	5775	69.4	5.61
B8051422	3ω	200/150	-250	-100	30	3.17	8913	2.73	6423	72.1	6.24
B8051506	3ω	200/150	-250	-200	30	3.20	8704	2.64	5021	57.7	4.88
B8051511	3ω	200/150	-250	-100	30	3.18	8517	2.60	6147	72.2	5.97
B8051515	3ω	200/150	-220	-70	30	3.17	8793	2.69	6200	70.5	6.02
B8051804	3ω	200/150	-280	-70	30	3.17	8952	2.74	6189	69.1	6.01
B8051809	3ω	200/150	-250	-70	30	3.20	8389	2.55	5934	70.7	5.76
B8051905	3ω, DS	200/150	-250	-70	30	3.17	8917	2.73	6327	71.0	6.14
B8051909	3ω, DS	200/150	-250	-70	30		8982		5977	66.5	5.80
B8051916	3ω, DS	200/150	-250	-70	30	3.17	8110	2.48	5690	70.2	5.52
B8051923	3ω, DS	200/150	-250	-70	30	3.15	7404	2.28	5117	69.1	4.97
B8052004	3ω, DS	200/150	-250	-70	30	3.15	8717	2.69	6189	71.0	6.01
B8052009	3ω, DS	200/150	-250	-70	30	3.17	8494	2.60	5966	70.2	5.79
B8052014	3ω, DS	200/150	-250	-70	30	3.20	8694	2.64	5966	68.6	5.79
B8052018	3ω, DS	200/150	-250	-70	30	3.18	8557	2.61	5510	64.4	5.35
B8052101	3ω, DS	200/150	-250	-70	30	3.17	9184	2.81	5955	64.8	5.78
B8052109	3ω, DS	200/150	-250	-70	30	3.13	8575	2.66	5085	59.3	4.94
B8052113	1ω, calibration	200/150	-1075	-1040	30	3.11	2956	0.92	0	0.0	0.00
B8052117	1ω, calibration	200/150	0	-1040	30	3.18	2889	0.88	124	4.3	0.12

* 1ω energy at input to converter (corrected for ASE), 3ω energy at output of last optic

As shown in Figure 4-1, the first part of HDTII consisted of an eight-shot ramp to 7 J/cm² followed by two shots at ~7.8 J/cm², which is the calculated 3-ns equivalent to the Beamlet milestone fluence of 8.4 J/cm² in 3.5 ns, assuming damage threshold scales as the square-root of the pulse length. The FOC was fielded alone in this part of the campaign, with the same doubler used in HDTI (RG8B-2), a conventional-growth tripler (80% LL6-11), and a high-damage threshold fused-silica lens (01K). After the first ten shots, the FOC optics were inspected, and two DOPS (DS02K and 04K) and a debris shield (DS02B) were installed. The two DOPs were mounted in a dual-slot aluminum bezel using nylon-tipped set screws, with a spacing between the plates of ~1.5 cm. The debris shield was mounted in the second slot of a similar package that was clamped to the back of the first, positioning the debris shield ~3 cm downstream of the second DOP. The DOP and debris shield holders were cleaned with the same procedure used on the FOC and IOM parts, but not baked. The spacing between the lens and the first DOP was 42.4 cm. All of the plates were tipped 22° from normal incidence. After six shots, the DOPs and debris shields were removed, and the FOC optics were inspected a second time. While a second debris shield was being prepared for testing, three additional shots were fired through the FOC at an average fluence of 6.3 J/cm². The second debris shield (DS03K) was then installed, and four shots were fired at ~7.6 J/cm² to obtain a comparative baseline for the DOP tests. The shot summary for this series is provided in Table 4-7. Throughout the campaign, the uncertainty in the 3ω fluence at the output of the tripler increased with the uncertainty in the transmission through the downstream optics.

ECMS NO CM RELEASE 20070611 14:14 0017657 OA (pdf format)

Table 4-7. Shot summary of Beamlet HDTII campaign.

Shot	Type	Pinholes μrad	SHG μrad	THG (int)	Δν GHz	fwhm ns	$E_{1\omega}$* J	$I_{1\omega}$ GW/cm²	$E_{3\omega}$* J	$\eta_{3\omega}$ %	$F_{3\omega}$ J/cm²
B8072102	3ω ramp	200/150	-250	0	30	3.17	3009	1.22	1567	52.1	2.01
B8072105	3ω ramp	200/150	-250	0	30	3.13	3559	1.46	1985	55.8	2.55
B8072201	3ω ramp	200/150	-250	0	30	3.08	4434	1.85	2780	62.7	3.56
B8072205	3ω ramp	200/150	-250	0	30	3.17	5072	2.05	3292	64.9	4.22
B8072208	3ω ramp	200/150	-250	0	30	3.15	5866	2.39	3835	65.4	4.92
B8072214	3ω ramp	200/150	-290	0	30	3.08	7108	2.96	4765	67.0	6.11
B8072303	3ω ramp	200/150	-295	150	30	3.06	8108	3.40	4034	49.7	5.17
B8072306	3ω ramp	200/150	-295	-150	30	3.13	7657	3.14	5361	70.0	6.87
B8072309	3ω	200/150	-295	-150	30	3.15	8907	3.63	6092	68.4	7.81
B8072313	3ω	200/150	-295	-150	30	3.11	8946	3.69	5956	66.6	7.64
B8072502	3ω ramp, DOP	200/150	-310	-200	30	3.13	5164	2.12	2947	57.1	3.78
B8072507	3ω ramp, DOP	200/150	-310	-200	30	3.11	7022	2.89	4253	60.6	5.45
B8072510	3ω, DOP	200/150	-295	-150	30		9078		5204	57.3	6.67
B8072704	3ω, DOP	200/150	-280	-100	30	3.03	9676	4.09	4817	49.8	6.18
B8072707	3ω, DOP	200/150	-310	-100	30	3.11	9110	3.76	5194	57.0	6.66
B8072711	3ω, DOP	200/150	-310	-100	30	3.10	9123	3.77	4567	50.1	5.85
B8072903	3ω	200/150	-310	-200	30	3.13	7247	2.97	4932	68.1	6.32
B8072906	3ω	200/150	-310	-200	30	3.11	7146	2.95	4911	68.7	6.30
B8072909	3ω	200/150	-310	-200	30	3.15	7179	2.92	4891	68.1	6.27
B8073002	3ω, DS	200/150	-310	-200	30	3.04	8782	3.70	5716	65.1	7.33
B8073102	3ω, DS	200/150	-340	-200	30	3.13	8865	3.63	5685	64.1	7.29
B8073105	3ω, DS	200/150	-340	-200	30	3.13	8991	3.68	5653	62.9	7.25
B8073108	3ω, DS	200/150	-310	-200	30	3.17	9578	3.87	5789	60.4	7.42

* 1ω energy at input to converter (corrected for ASE), 3ω energy at output of last optic

At the conclusion of the HDTII campaign, the tripler by visual inspection had 47 damage sites, the largest being 2.5 cm in diameter (see Figure 4-3). Of these, 43 were on the output surface of the crystal; the four on the input surface were all less than 150 μm in size. Figure 4-4 shows how the size of four of the largest sites on S_2 evolved over the course of the campaign. The measurements were obtained from photographs of the 3ω beam taken with the focal plane diagnostic high-resolution near-field camera imaging the plane of the lens [9]. To interpret the data it was assumed that the mechanics of the damage growth occur on time-scales that are long compared to the 3-ns exposure of the photographs, and thus that the damage measured in a given photograph is representative of the size of the site after the previous shot. Tracing the four largest sites back in time, it was possible to determine that they each originated from small ~100- μm features that were visible in the very first photograph. These small features remained essentially unchanged for the first few shots of the ramp and did not begin to grow until the fluence reached ~4 J/cm². For the first ten shots, the growth behavior of the four sites was essentially the same. No data was analyzed for the period of time in which the DOPS were installed, but after the DOPS were removed, two of the sites showed a greatly increased growth rate. The rapid growth rate appeared to be related to cracks emanating from these sites, while the lower growth rate sites exhibited more stable, well-defined pit morphologies.

ECMS NO CM RELEASE 20070611 14:14 0017657 OA (pdf format)

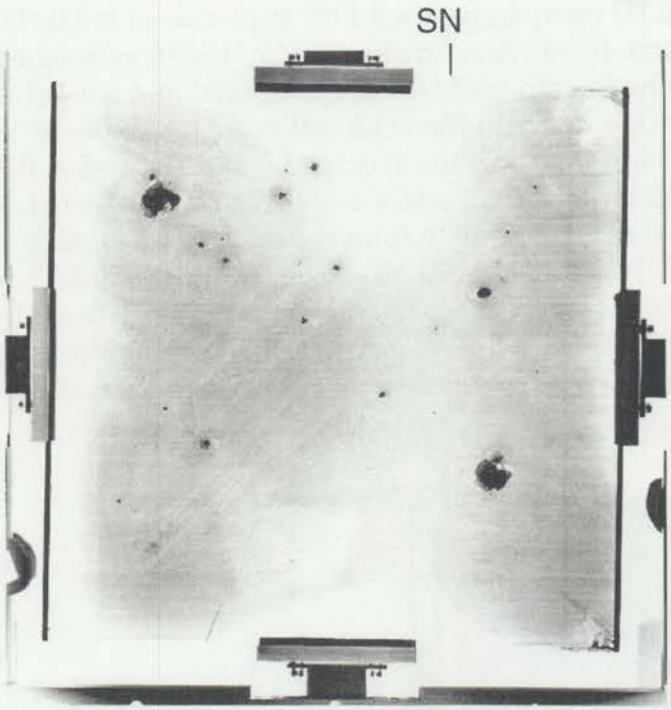

Figure 4-3. Photograph of the HDTII tripler taken with the damage mapping system at the end of the campaign, showing 47 damage sites, the largest being 2.5 cm in diameter.

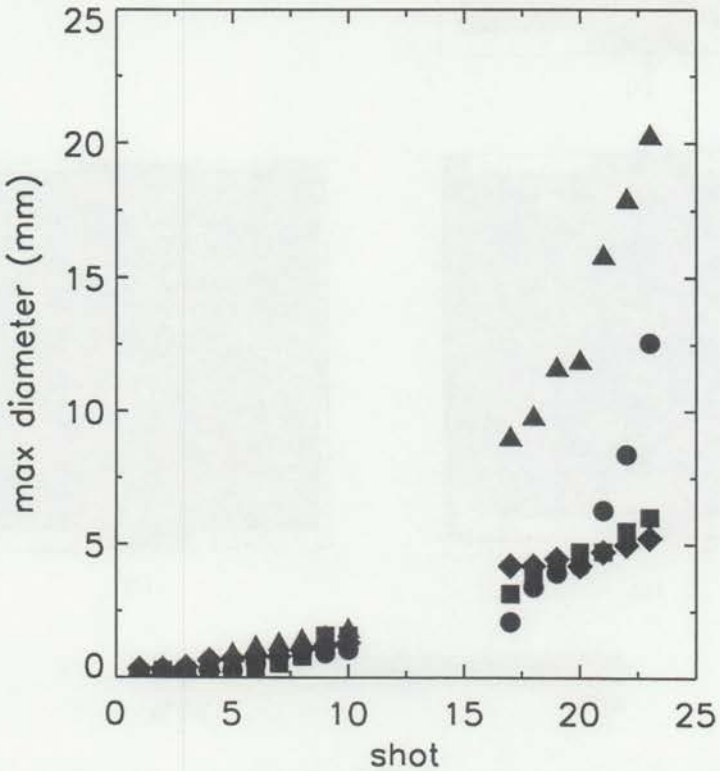

Figure 4-4. Damage growth of four sites on the output surface as measured from high-resolution 3ω near-field photographs. Data was not analyzed for shots with the diffractive optics plates installed.

ECMS NO CM RELEASE 20070611 14:14 0017657 OA (pdf format)

Like the MDT and HDTI campaigns, the KD*P tripler used in HDTII was not a newly finished and coated crystal. It was first finished on 12/15/96, refinished, coated but never deployed in 2/97, refinished again on 5/15/98, processed and sol-gel AR-coated on 5/21/98, and used from 6/18/98 to 6/25/98 in the FOA test mule for the Beamlet CEA experiments [12]. As shown in Figure 4-5, the aperture-averaged 3ω transmission through the crystal prior to use was only 89%, which is approximately 6% lower than expected. Following the CEA experiments, the crystal was washed with toluene, and the transmission measured at 85.5% on 7/15/98. A small area of the crystal was damage tested to > 10 J/cm2 on 7/16/98, at which time microscopy revealed that there were line defects on the surface of the crystal similar to those observed on LL1-12 after HDTI (see appendix), but limited to isolated regions comprising about 10% of the total area. After the experiment, these line defects covered most of the input and output surfaces of the crystal.

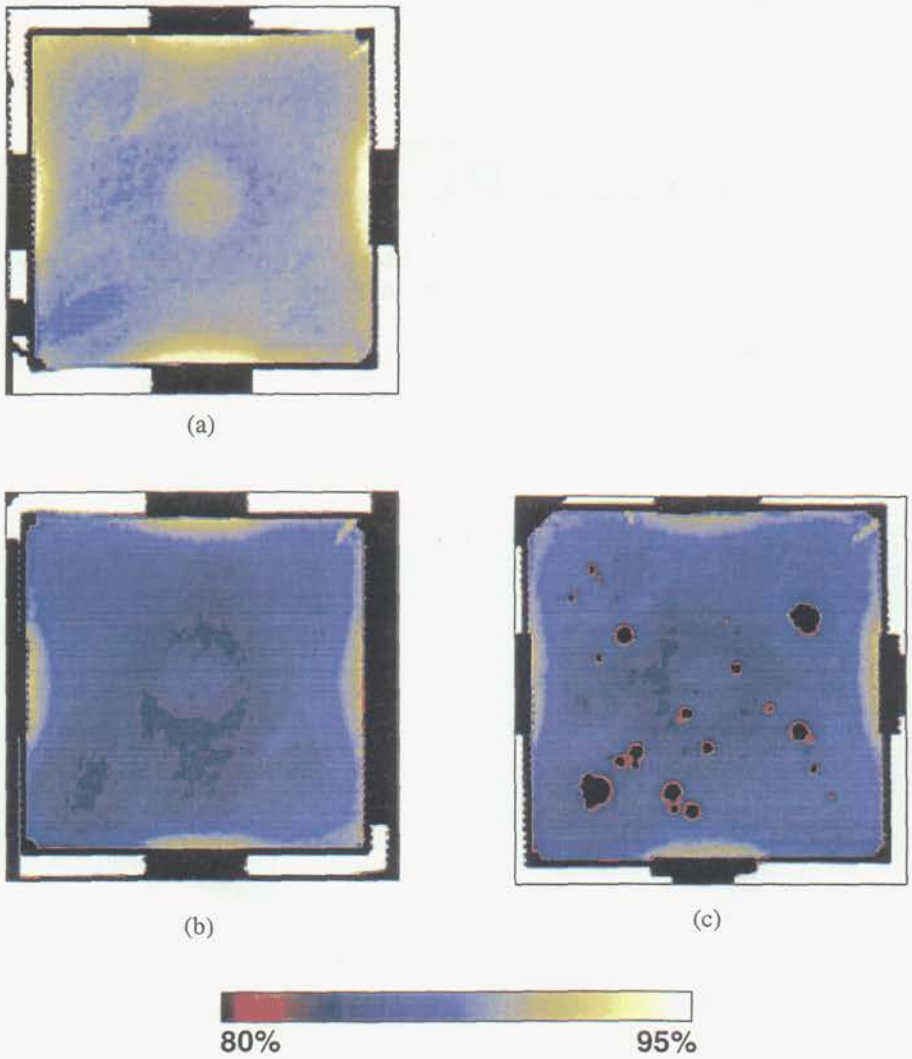

Figure 4-5. Scanning photometer measurements of 3ω transmission through the HDTII tripler (a) after sol-gel coating and prior to use, (b) after CEA experiments and toluene cleaning, and (c) after HDTII. Aperture-averaged transmissions are 88.8%, 85.4%, and 84.9%, respectively.

ECMS NO CM RELEASE 20070611 14:14 0017657 OA (pdf format)

4.6. Conclusion

Laser-induced surface damage of KD*P was first observed at NIF fluences during the Beamlet tests of prototype FOCs in vacuum conducted this past year. The damage in the Beamlet tests occurred on the output surface of the crystals, and grew rapidly to very large size in the case of HDTII. At least some of the damage in HDTII originated at small unidentified defects that were visible on the very first shot. In all of the tests, the sol-gel AR coatings on the crystals were of very poor quality, with 3ω transmissions that were 5 to 10% lower than expected for new coatings. Large-area surface damage was limited to HDTI. Initiation and growth of surface damage was observed in all three high-fluence test mule campaigns.

4.7. References

1. M. Runkel, internal reports NIF-LMO96-098, NIF-LMO96-509, NIF-0003690, Lawrence Livermore National Laboratory, Livermore, CA.
2. C. E. Barker et al., "Design and performance of the Beamlet laser third harmonic frequency converter," Proc. Soc. Photo. Instrum, Eng, Vol. **2633**, 398 (1995).
3. Inspection notes, C. E. Barker, Nov. 22, 1995.
4. Inspection notes, C. E. Barker, March 31, 1995, and M.E. Werve, Sept. 27, 1995.
5. M. Kozlowski, S. Maricle, R. Mouser, S. Schwartz, P. Wegner, and T. Weiland, "Laser damage performance of fused silica optical components measured on the Beamlet laser at 351 nm," *Symposium on Optical Materials for High Power Lasers*, (Boulder, CO), Sept. 30, 1998.
6. Inspection notes, M.E. Werve, Dec. 19, 1997.
7. N. Nielsen, "Reflectivity of sol-gel coated window on the Beamlet test mule," internal memorandum, Aug. 27, 1998.
8. J. Ertel, "Organic films on metal surfaces," internal report, Lawrence Livermore National Laboratory, Livermore, CA, Oct. 22, 1998.
9. P. J. Wegner et al., "Characterization of third-harmonic target plane irradiance on the National Ignition Facility Beamlet demonstration project," Fusion Tech., Vol. **30**, 539 (1996) Feru, Beamlet Tech. Mtg.

ECMS NO CM RELEASE 20070611 14:14 0017657 OA (pdf format)

ECMS NO CM RELEASE 20070611 14:14 0017657 OA (pdf format)

5.0 Optics Damage

5.1 Fused Silica Damage

5.1.1 Purpose

The original purpose of the high-fluence 3ω campaigns that occurred in January through July 1998 was fourfold:

1. To demonstrate the full-aperture damage performance of prototype NIF fused silica optics manufactured with current vendor finishing capabilities. In most cases, the optics made for these tests were not made using the final manufacturing equipment expected to be used for NIF production, although the processes were close enough that they had been qualified for NIF optic production.

2. To compare damage performance measured in off-line tests with that produced during Beamlet tests. The data of interest includes damage site concentration and damage site growth rate. Both of these parameters would be measured as a function of fluence.

3. To evaluate the evolving model for predicting optical damage evolution under NIF-like conditions based on data obtained in off-line tests.

4. To evaluate the performance of an integrated final optics package including interactions between the tripler, lens, diffractive optic plates, and the debris shield. Primary interactions expected included beam modulation from upstream optics and contamination from damage to adjacent optical surfaces.

The damage performance of 3ω fused silica optics was evaluated in four different campaigns during 1998. The optics used and a summary of the shot programs are provided in Table 5-1. The final campaign, High Damage Threshold test 2 (HDT2) included a test of the full integrated optics package. HDT2 is the focus of the present report, but the other campaigns will be described when relevant. The campaign had four phases, a–d. The fluence programs are described in Table 5.1, and the optics configurations are shown in Figure 5-1.

ECMS NO CM RELEASE 20070611 14:14 0017657 OA (pdf format)

Table 5-1. Fused silica optics used in 1998 Beamlet 3ω Mule campaigns.

Campaign		Fluence program					Optic			
		# pulses		tau	fluence J/cm2					
		ramp	main	ns	average	highest	RFL	DOP1	DOP2	DS
MDT		6	20	3	5.1	5.7	02T			
Tripling			38	1.5	2.5	4	01K			
HDT1	a	3	10	3	5.1	6.3	04T			
	b		10	3	5.6	6.2	04T			02B
HDT2	a	8	2	3	5.1	7.8	01K			
	b	2	4	3	7.1	8.6	01K	02K	04K	02B
	c		4	3	6.3	6.3	01K			
	d		4	3	7.6	7.7	01K			03K

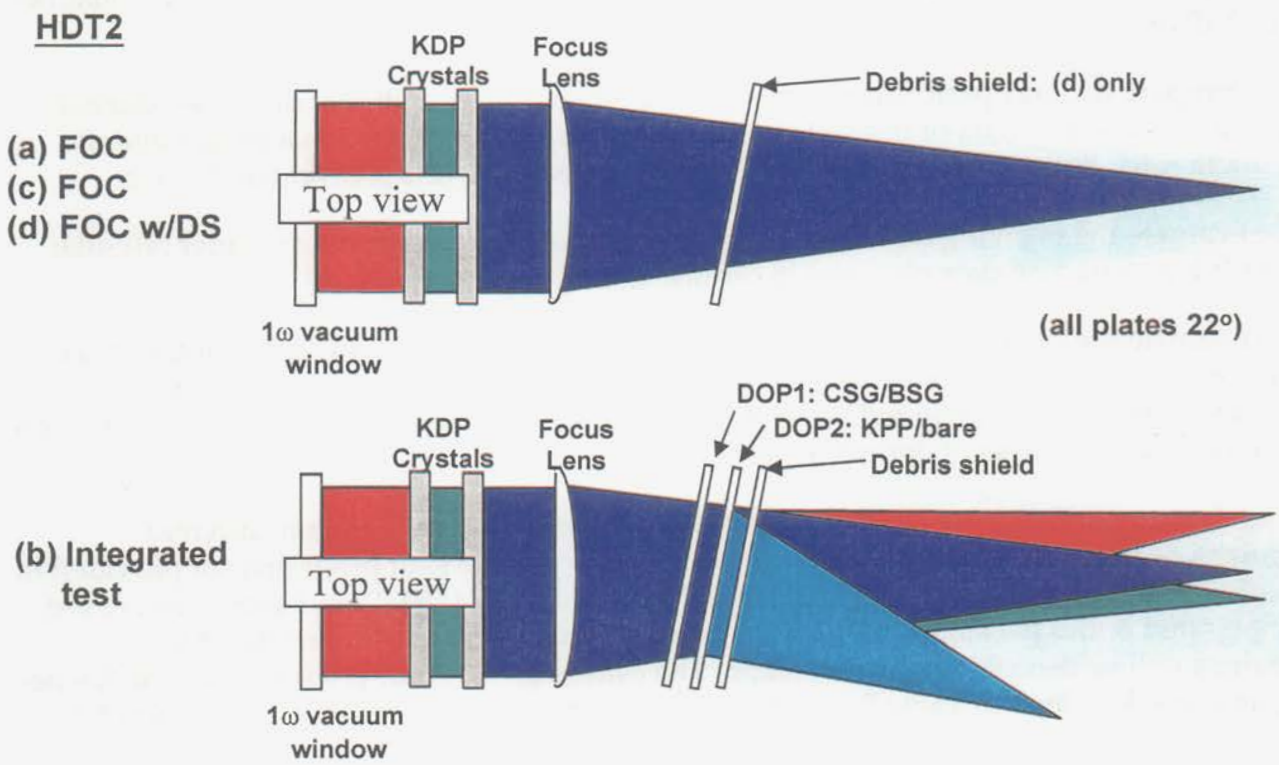

Figure 5-1. Four optical configurations used to test the FOC and the integrated optics package.

5.1.2 Summary of Optics Used

A high-quality 3ω polished focus lens, two debris shields, and two diffractive optics plates were evaluated as part of the July HDT2 campaign. The HDT2 shot program is summarized in Figure 5-2. The lens (RFL01K) had been tested off-line and had been used, and lightly damaged, in the earlier Beamlet frequency tripling campaign (April 16–30, 1998) with low

ECMS NO CM RELEASE 20070611 14:14 0017657 OA (pdf format)

fluence shots. This lens was used for the entire HDT2 campaign, which consisted of 23 shots ranging in fluence from 2 to 8.5 joules/cm^2 at the lens surface, 3-ns square pulse. For the six-pulse integrated test during HDT2, a debris shield (DS02B) was used that had been previously damaged during the final 10 pulses of the HDT1 campaign (see Table 5.1). The two diffractive optics plates (DS02K and DS04K) used in the integrated test had not been previously illuminated. During the final four pulses of the HDT2 campaign, another previously unexposed debris shield (DS03K) was exposed. For the HDT2 lens and debris shield that had been used on Beamlet prior to the campaign, the optics were stripped and recoated prior to installation.

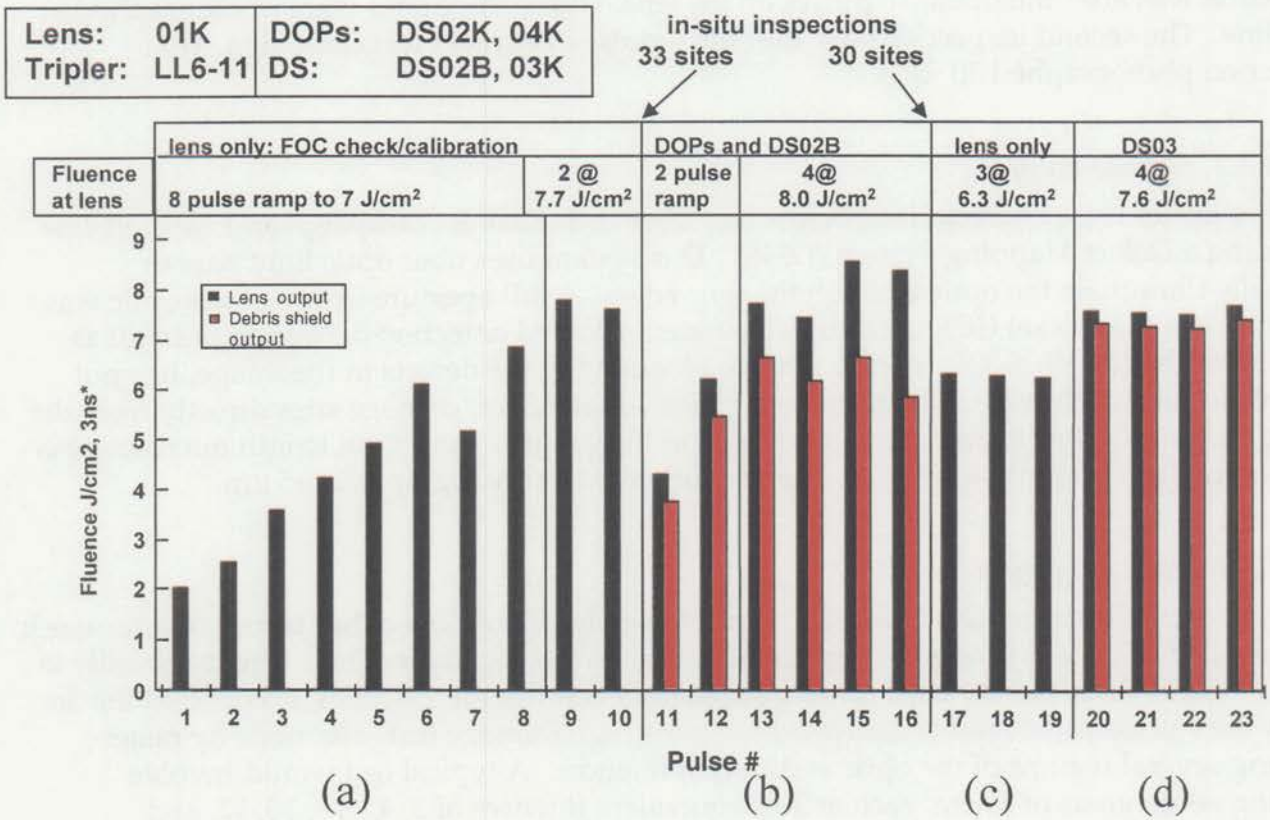

Figure 5-2. Fluences used in the four phases of HDT2.

5.1.3 Experimental Techniques

5.1.3.1 In-chamber microscopy

In-situ damage characterization of the focus lens during the MDT and HDT Beamlet campaigns employed the use of a CCD camera and microscope to record images of laser-induced damage. Initially, two cameras were used to record images at ~3- and ~9-mm field of view (FOV) without repositioning the microscope during the mapping process. By the end of the campaigns, a ~6-mm FOV system was converged upon that made finding of individual damage sites simple while still maintaining the necessary resolution. An Infinity K2 long-working-distance single-camera microscope was used in this effort. A working distance of 30

ECMS NO CM RELEASE 20070611 14:14 0017657 OA (pdf format)

cm provided for a safe margin between the camera and the sample. The microscope assembly was bagged for cleanliness and mounted on a X–Y rail system for coordinate measurements. All images were taken from the output side of the lens. The lens was also lit from the output side using an intense fiber light was held close to the damage, diffusely scattering light into the camera. The light source was positioned to minimize CCD saturation and background noise. Damage position (X–Y coordinate plus front, rear, or bulk), diameter, and morphology were recorded for each site measured. The origin of the X–Y coordinate system was at the largest recognizable site.

During the HDT2 campaign, the system was vented twice for in-situ inspections. The first inspection was after the initial 10 pulses on the lens. Thirty-three sites were photographed at that time. The second inspection was after the 6-pulse integrated test campaign. That inspection photographed 30 sites.

5.1.3.2 Surface mapping

Silica optics were characterized before and after each Beamlet campaign and each off-line test, using a Defect Mapping System (DMS). This system uses fiber optic light bars to internally illuminate the optic through the four edges. A full aperture image of the optic was taken using a megapixel CCD camera. The system allowed detection of defects as small as 10 μm over the full 39- × 39-cm optic. Due to blooming of the defects in the image, it is not possible to resolve the size or features or the individual defect/damage sites directly from the megapixel map. After identification of defects in the image, a long focal length microscope is used to photograph individual sites. The resolution of the micrographs is ~5 μm.

5.1.3.~~4~~ 3 Laser damage tests

Many of the Beamlet FOA fused silica optics were tested off line either before or after use in the Beamlety FOA. All tests were performed in the 3ω test facility in B165. The test facility is similar to B391 Plato facility used for large-area laser conditioning studies, except that the 3ω facility is in a cleanroom and is dedicated to 3ω testing. Damage tests are made by raster-scanning several regions of the optic at different fluences. A typical test would involve scanning seven areas of 20 cm^2 each at 3-ns equivalent fluences of 2, 4, 6, 8, 10, 12, and 14 J/cm^2. The laser used is a commercial Nd:YAG system. The beam is Gaussian with a $1/e^2$ diameter at the sample plane of 1–1.6 μm. The rep-rate is 10 Hz, and the pulselength is 6–8 ns. Step increments in the raster-scan are specified as the beam at a given fraction of the peak fluence. For example, a scan increment corresponding to the 90% peak beam diameter would be ~0.2 μm.

After scanning areas at the specified fluences, the DMS system was used to map and count the number of damage sites created during the test. Additional inspections with a microscope were used to determine the location of individual damage sites (front, rear, bulk). Damage concentrations for each test region were calculated after correcting the scan size for the effective beam area. The effective beam area was calculated based on a Weibull statistical analysis attapted by M. Feit.

ECMS NO CM RELEASE 20070611 14:14 0017657 OA (pdf format)

5.1.3.4 Fluence distributions

Fluence distributions were measured during the Beamlet campaigns using scientific-grade CCD cameras with a spatial resolution of ~1 μm. The depth of field of the camera is ~2 m. For experiments involving only the FOC (doubler, tripler and focus lens), the fluence distribution measured by the standard near-field diagnostic may provide a good approximation of the fluence distribution at the surfaces of the optics of interest (tripler and lens). For subcampaigns where additional optics were present (DOPs or debris shield), the beam profile can be expected to change significantly as the beam propagates through the mule, particularly if damage is occurring in the optics. In these cases, the standard near field does not provide suitable information to describe the fluence seen by individual optics. It is clear from inspection of damage patterns seen on the optics, particularly the DOPs and debris shield, that the fluence distribution was changing significantly over distances of only a few cm. Features seen on one surface are found to be shifted spatially (vertical lines on DOPs and debris shield) or to have changed sharpness (feature on top north corner of KPP and debris shield) from one optic to the next. Differences in the optical performance the optics is also apparent from the post-campaign photometry maps.

For most pulses, a film camera was used to obtain higher-resolution near field (HRNF) fluence distributions in the mule. For this camera, the depth of field was ~0.2 m, and the resolution was ~85 microns. For all pulses except the 6-pulse "integrated FOA" campaign, the HRNF camera imaged the lens plane. During the integrated FOA campaign, which included the two DOPs and the debris shield, the focal plane of HRNF camera was moved to the debris shield. A comparison of profiles from the standard and high-resolution near-field diagnostics should be made to evaluate the quality of the fluence distribution data.

One of the objectives of the Beamlet high-fluence 3ω campaigns was to compare the measured damage performance with the performance predicted from off-line damage tests of the individual components. An accurate comparison requires knowledge of the fluence distribution at each optic. The concentration of laser damage sites on an optic follows a strong power dependence on the fluence ($C = F^m$, where m varies from 2 to 22). In general, the density of damage of an optic can be expected to change by about one order of magnitude for a fluence change of about 2 J/cm^2. The fluence peaks therefore have a very strong influence on the average damage density, and therefor the lifetime, of the optic. The damage density predicted from off-line tests can always be expected to underestimate the measured damage performance on Beamlet if the Beamlet fluence distribution used in the prediction is not accurate at the plane of the optic, that is, the peak fluences are averaged over several optics.

5.1.4 Results (not interpretation)

5.1.4.1 Focus lens RFL01K

Background

RFL01K was manufactured by Kodak and delivered in February 1998. Details of the finishing process are proprietary and are described in other documents. Off-line damage tests of RFL01K were performed in May 1998. The damage density data obtained from those tests are summarized in Figure 5-3. Lens 01K was damage tested at 355 nm using a large-aperture

ECMS NO CM RELEASE 20070611 14:14 0017657 OA (pdf format)

raster scanning facility in Building 165 (1-mm-diam beam). The lens was scanned at fluences ranging from 2 J/cm^2 to 14 J/cm^2, 3 ns, on a cumulative surface area of 140 cm^2. A DMS map of finishing defects and laser damage was made before and after the damage test. The after damage test DMS map indicated 164 artifact sites including laser damage and finishing defects. A complete report of the test is available. [1]

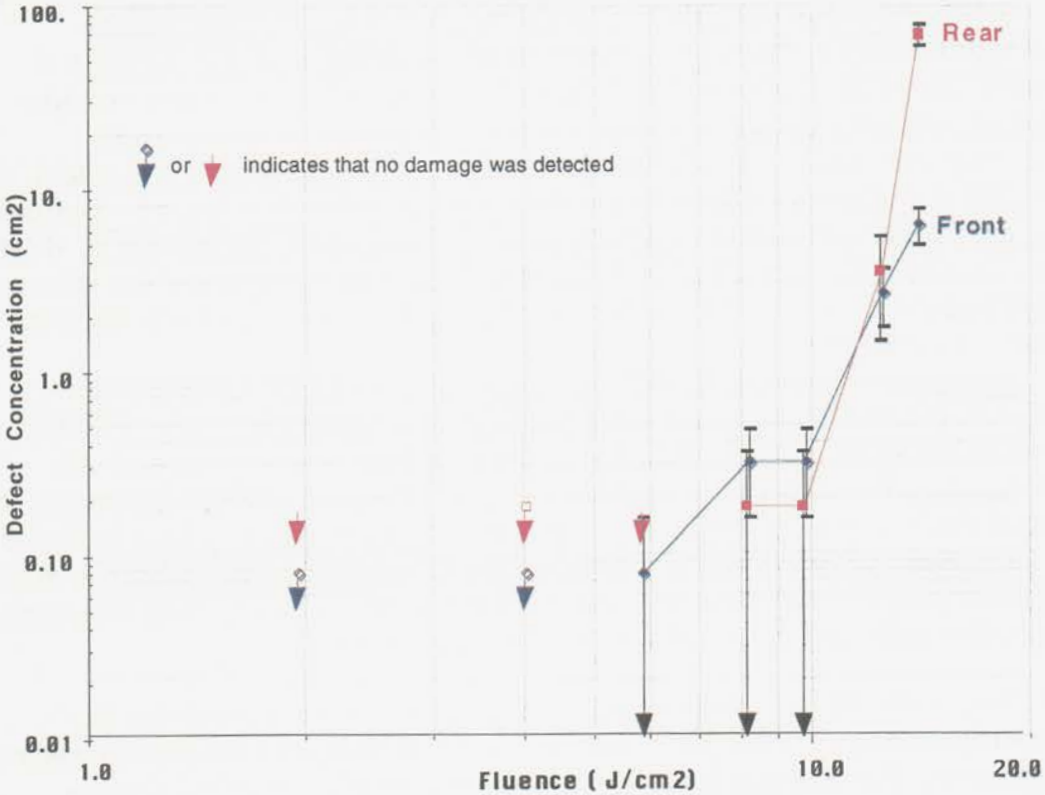

Figure 5-3. Results from off-line 3ω damage testing of lens 01K prior to installation on Beamlet. The defect concentration plot shows the contributions from the front and rear surfaces. The open symbols indicate the detection limit for the scan (i.e., concentration if one damage site was detected).

The lens was sol-gel coated with a 3ω AR and used for frequency tripling experiments in April 1998. Mapping of the lens following that campaign identified 545 artifact sites within the beam aperture. Microscopy of a 20% sampling of the artifacts indicated the following distribution of site locations: 190 on front surface, 20 in bulk, and 335 on rear surface. Note that 164 of the artifact sites were present prior to the Beamlet tripling campaign. The largest damage site on the lens had a diameter of 2.35 mm. This site was initiated during the off-line test and had a diameter of 0.95 µm prior to installation for the tripling campaign.

Most of the 20 bulk sites identified after the Tripling campaign showed no evidence of bulk damage at that time. However, most had created rear-surface damage sites due to modulation.

After DMS mapping of the Tripling campaign damage, but prior to use in the HDT2 campaign, the sol-gel coating on the lens was removed in B392, and the lens was recoated.

ECMS NO CM RELEASE 20070611 14:14 0017657 OA (pdf format)

HDT2 illumination

During the initial 10 pulses of the campaign, some discrete damage to the lens was observed by visual inspection from the BLISS diagnostic position and was indicated in the near-field images. It was apparent that the lens input surface was also being contaminated with debris from damage to the KDP tripler output surface.

Following the first ten pulses of the campaign two members of the damage team entered the mule and inspected the lens. The inspection microscope and procedure were described above. The primary purpose of the inspection was to document the evolving size of new and existing damage sites so that damage growth rates could be evaluated. During the first inspection, 33 sites were photographed. The lens was again inspected following the 6-shot integrated test. In that inspection 30 sites were photographed.

The lens was next inspected in the FOA after it was moved from the Beamlet Mule to B174. It appeared that many of the KDP damage sites had deposited debris in the input surface of the lens forming hazed regions ~1 cm in diameter. Rings of diffuse damage (like sand blasting) were apparent on the output surface of the lens opposite the KDP-influenced input surface areas.

There was also indication that damage at scratches on the input surface of the lens had also deposited debris on the output surface of the tripler. This tripler damage then caused modulation that damaged the output surface of the lens in an identical pattern.

The lens was removed from the FOC and transported to B392 for photometry measurements. The lens was then moved to the 3ω Test lab in B165 for documentation of the laser damage. A full-aperture image of the lens was taken using the DMS inspection system. The 33 sites inspected during the in-situ inspections were photographed again. Additional micrographs were taken to document the typical state of the input and output surfaces both inside and outside the beam aperture.

No contamination sampling has been performed on this lens.

Damage observations on lens RFL01K

The DMS image of the lens was analyzed for an initial evaluation of the various contributions to the lens damage. This DMS map is shown in Figure 5.4, which identifies several types of damage sites on the lens (Note the optic is incorrectly positioned in this map. The upper North corner of the optic is in the lower right corner). Using a NIH image analysis package the total obscuration on the lens resulting from damage was calculated to be ~11%. Note that this value is an overestimate because some blooming is allowed in order to document the positions of the small damage sites (≥ 5 micron diameter).

ECMS NO CM RELEASE 20070611 14:14 0017657 OA (pdf format)

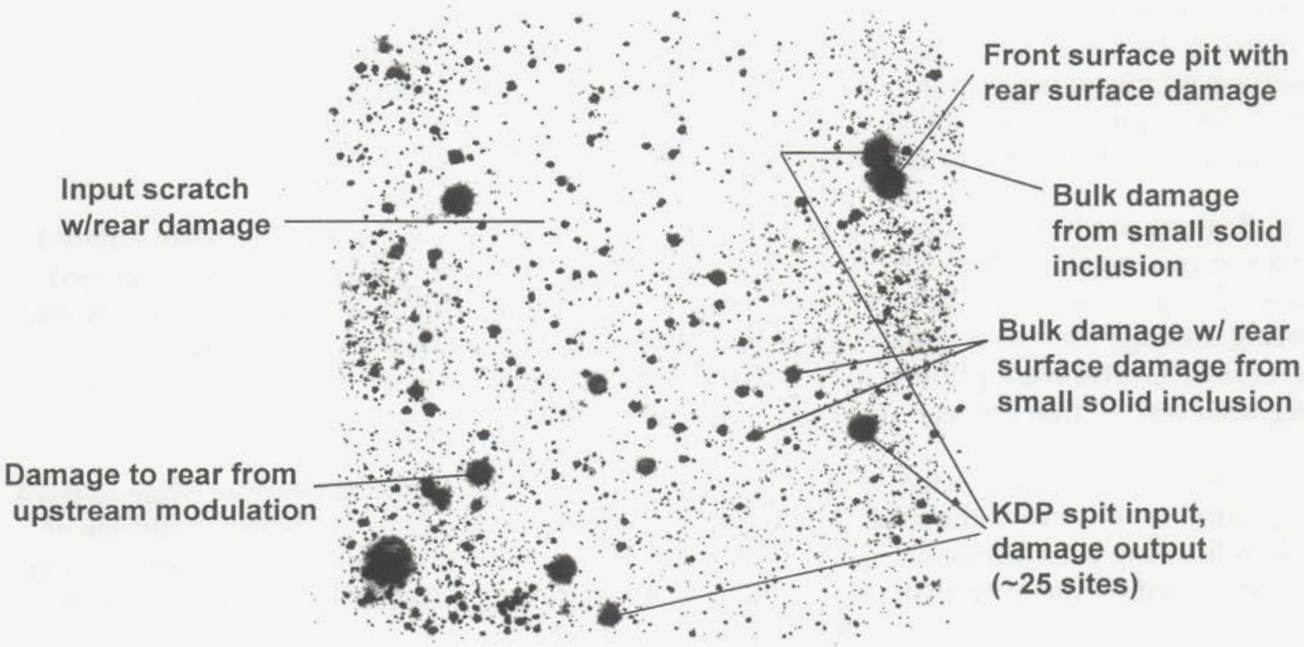

Figure 5-4. Automated image analysis indicates over 9000 catter sites >10μm (note: upper north corner on Beamlet is lower right corner in this image).

Several contributors to damage to the lens are immediately apparent:

a. Damage induced by KDP tripler output surface damage (35% of the obscuration).

b. Damage associated with small (<80 μm) solid inclusions in the fused silica (20% of the obscuration).

c. Damage assumed to be associated with the lens finishing process (40% of the obscuration). It is likely that some of the damage resulted from system-induced surface contamination, but in our initial inspection, we had no way to differentiate such sites.

The relative contributions of (a) tripler-associated damage, (b) bulk sites and (c) all other types is best seen by comparing Figures 5-5(a), 5-5(b), 5-6(a) and 5-6(b).

- In Figure 5-5(a), the DMS map of RFL01K from Figure 5-4 has been rotated so the upper north corner is on the upper left side of the image. Obscuration is ~10.7%.

- Figure 5-5(b) depicts the same image as Figure 5-5(a), but the obscurations associated with KDP damage were manually removed from the image. Remaining obscuration is ~7.1%

- Figure 5-6(a) depicts the same image as Figure 5-5(b), but the small number of obscurations related to pre-HDT2 off-line raster testing were removed from the upper right corner of the image. Remaining obscuration is ~6.6%.

ECMS NO CM RELEASE 20070611 14:14 0017657 OA (pdf format)

- Figure 5-6b depicts the same image as Figure 5-6a, but the sites associated with bulk damage (mostly associated rear-surface damage sites) have been removed. Remaining obscuration is ~4.5%.

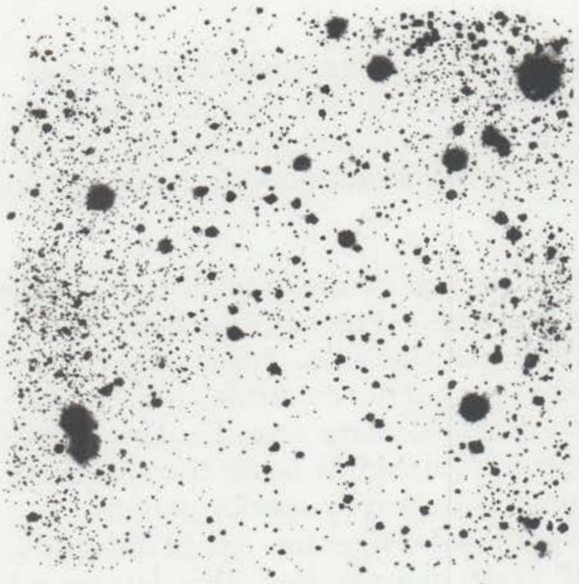

• Fraction of clear aperture obscured: ~10.7%

(a)

•Fraction of clear aperture obscured: ~7.1%

(b)

Figure 5-5(a). DMS image of lense RFL01K after Beamlet HDT2 campaign and (b) DMS image from Figure 5-5(a) but with KDP damage removed (3.6% obscuration removed).

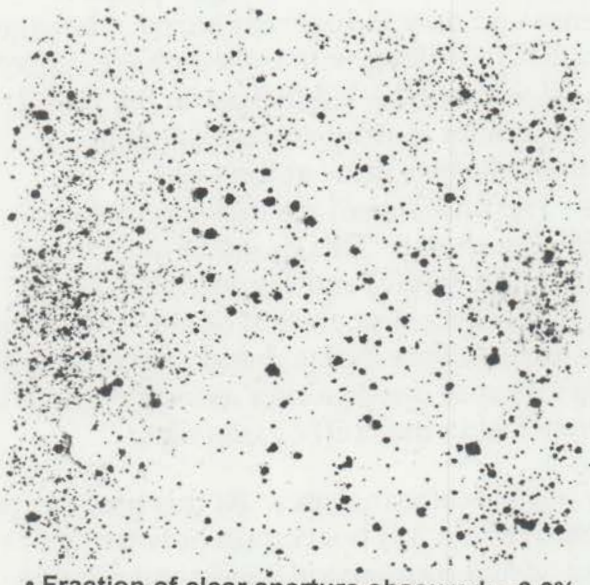

• Fraction of clear aperture obscured: ~6.6%

(a)

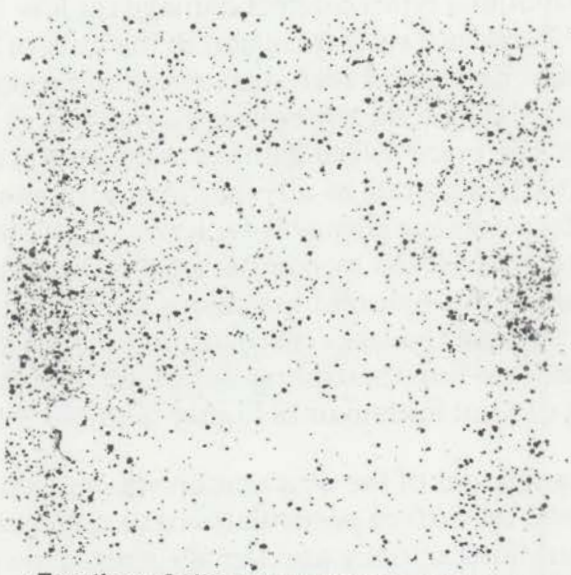

• Fraction of clear aperture obscured: ~4.5%

(b)

Figure 5-6(a). DMS image of lens RFL01K after Beamlet HDT1 campaign, but with KDP and off-line testing damage removed (4.1% obsuration removed) and (b) DMS image from Figure 5-6(a), but with damage associated with bulk damage removed (6.2% obscuration removed).

ECMS NO CM RELEASE 20070611 14:14 0017657 OA (pdf format)

An initial count of the number of damage sites by the NIH software resulted in a count of ~10,000 sites. Approximately 8000 of these sites are initially attributed to the lens surface finishing. At this time, the relative contributions of front and rear damage have not been resolved.

The lens was damaged more than anticipated both in terms of density of damage sites (~10–50x expected density) and rate of growth of damage sites (30–50x expected rate). The expected density was based on the off-line test (Figure 5-3 above), and the expected growth rate was based on limited 3ω growth studies performed in optics sciences lasers (OSL) (Milam and Genin).

Damage induced by the large KDP tripler damage sites was markedly different on the front vs. the rear of the lens. The front surface of the lens had large (~1 cm) diffuse scattering damage sites similar in size and shape to the KDP tripler damage sites. These were caused by spitting of the KDP onto the lens (indicated by topography, but not confirmed by chemical analysis) and possibly by modulations induced by the tripler damage sites. The lens showed a doughnut-shaped ring of damage on the rear (output) surface slightly larger than the front surface damage site. This ring of damage was presumably caused by speckle pattern modulation from scattering off the edge of the front-surface damage site. About 35% of the obscuration on the lens was associated with the KDP tripler damage sites. This damage is best observed by comparing Figures 5-5(a) and 5-5(b).

The second category of lens damage was caused by ~60 solid inclusions within the bulk of the fused silica lens. Twenty of these sites were mapped after the low-fluence tripler campaign, since they had already caused either rear surface or bulk damage downstream of the inclusions. It has been demonstrated by modeling (Feit) and by experiments (Genin, Runkel) that this type of defect damages at low fluence and may induce rear-surface damage. Figure 5-7 shows a solid inclusion in the bulk of lens RFL01T along with bulk damage caused by a similar defect and rear-surface damage associated with the bulk damage. In the HDT2 campaign, the bulk damage sites grew slowly at a rate similar to front surface damage. However, the rear-surface damage associated with the bulk sites grew at the same unexpectedly high rate as all other rear-surface sites. The final size of the inclusion-related rear-surface damage sites was typically about 500–800 μm in size. This group of defects is most readily observed by comparing the DMS map in Figure 5-6(a) and Figure 5-6(b). As a consequence, the ~60 solid inclusions induced about 20% of the obscuration on the lens. These inclusions produced large rear-surface damage sites because they initiated and started to grow during the low-fluence tripling campaign. The higher density damage sites associated with finishing did not initiate until higher fluences were reached in the HDT2 campaign.

The remainder of the obscuration was caused by ~8000 scattering sites. At this time, scatter sites caused by surface particulates have not been removed, so it is not certain how many of the obscurations actually are damage sites. However, visual comparison inside and outside the Beamlet test aperture suggest most of these are probably caused by damage sites rather than particulate scattering. These damage sites are assumed to be attributed to unknown surface flaws associated with the 3ω finishing process. The finishing related defects represent the largest single component of the overall obscuration: ~40%.

ECMS NO CM RELEASE 20070611 14:14 0017657 OA (pdf format)

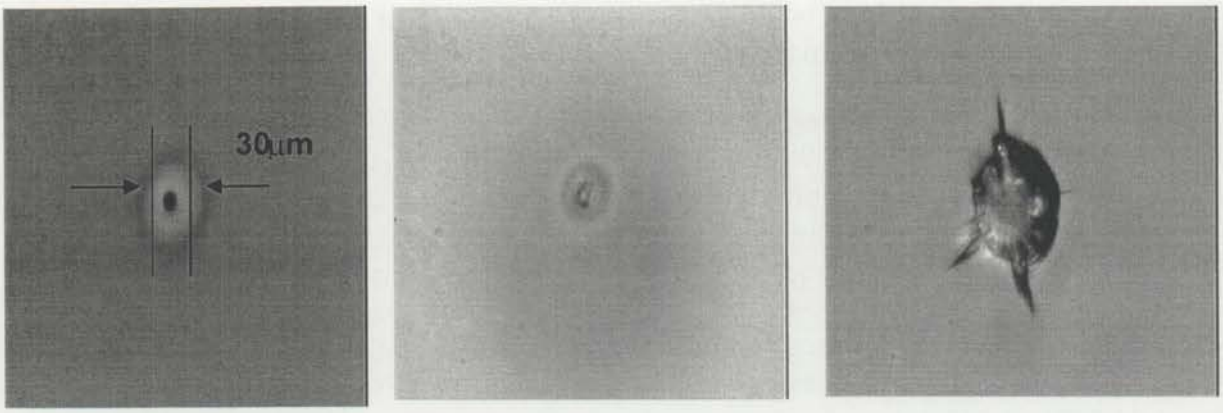

Bulk inclusion Bulk damage Rear surface

Figure 5-7. Solid bulk inclusion and associated damage in fused silica lens RFL01T.

Some of the uncorrelated damage may have been caused by particulate contamination on the lens, but there was no direct evidence of contamination-related damage except for the ~20 large KDP tripler damage sites. Surface damage growth rates may have been higher than expected due to surface contamination, but again, there was no direct evidence that contamination affected damage growth rates.

A fine scale (~20 μm spacing) semi-periodic line structure from the KDP tripler was imprinted into all downstream optics within the laser aperture. The defect was observed on both front and rear surfaces as either a slight disruption of the AR coating or small damage under the coating. This damage is shown in Figure 5-8.

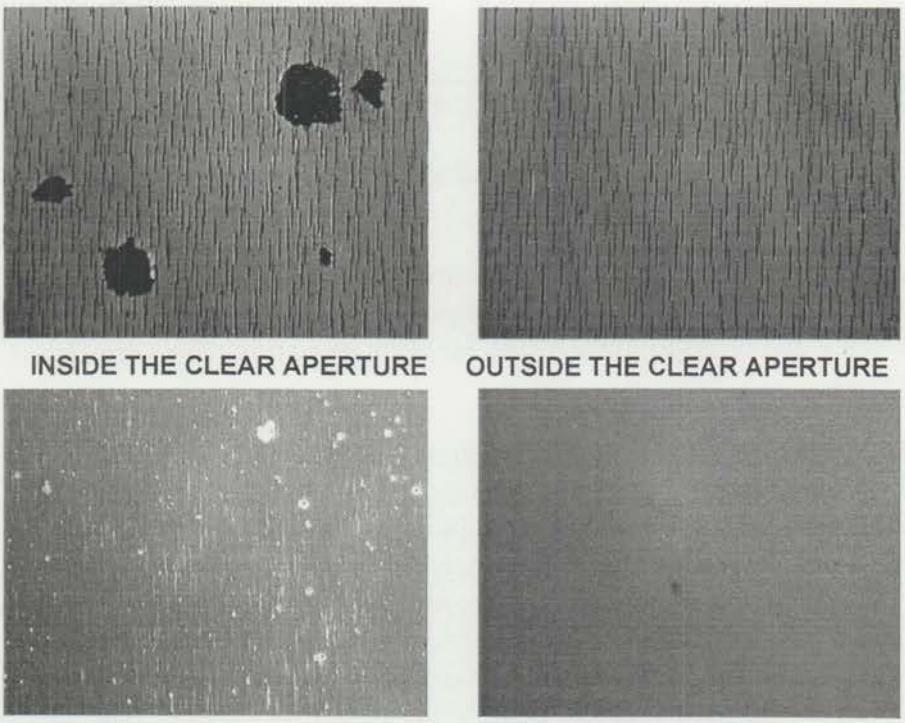

INSIDE THE CLEAR APERTURE OUTSIDE THE CLEAR APERTURE

- KDP output surface
- Focus lens input surface

Figure 5-8. The fine-line structure on the KDP-crystal-coated surfaces replicated as damage in all the downstream-fused silica optics.

ECMS NO CM RELEASE 20070611 14:14 0017657 OA (pdf format)

About 5% of the obscuration of the beam was caused by growth of damage sites created during off-line testing prior to the campaign.

Damage growth rates were calculated from the damage micrographs obtained during the in-situ and DMS inspections. Figure 5-9 provides a summary of the growth rates measured in the sub-campaigns of the HDT2 test (points connected by thick, solid lines). HDT2 data is provided for front, rear, and bulk damage and is compared with similar measurements made in the MDT, tripling, and HDT1 campaigns. The rear-surface growth rates measured in three campaigns on three lenses made by two different vendors all show similar growth rates near 5 J/cm^2. Rear-surface growth rates are consistently ~10× higher than those of the bulk or front surface. Because the obscured area varies as the square of the growth rate, the rear-surface damage clearly dominates functional damage effects.

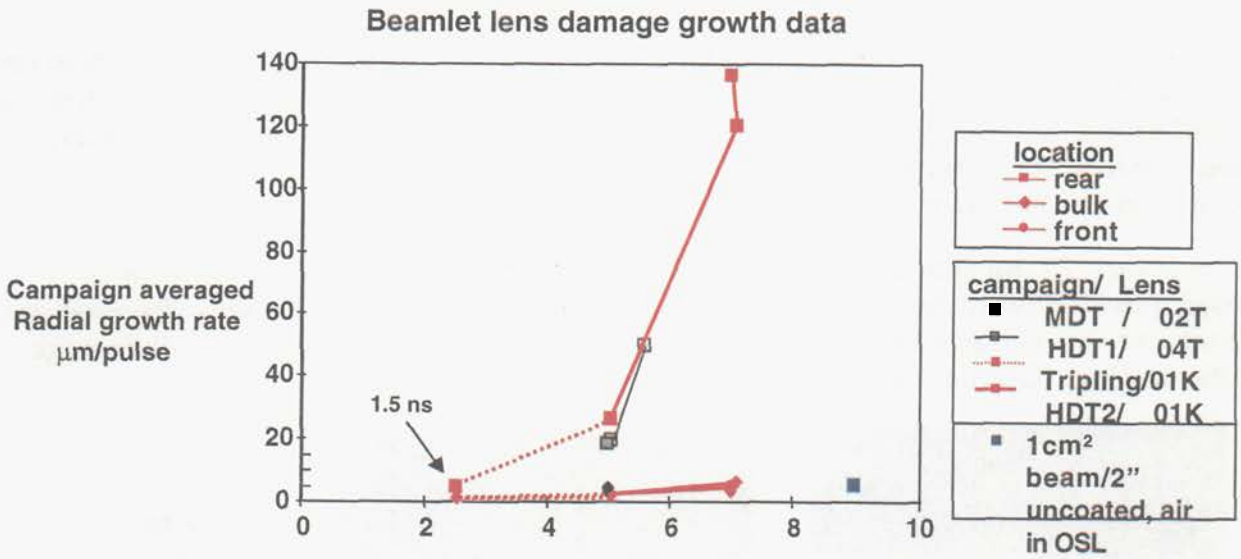

Figure 5-9. Summary of Beamlet lens damage growth rates calculated from damage micrographs obtained during in-situ and DMS inspections.

In small-beam growth experiments at 1ω, the growth rate varies linearly with fluence. For the Beamlet data, it is not clear that the growth rates are as well behaved. Note, however, that the data at the highest fluences were obtained late in the HDT2 campaign after significant KDP and DOP damage had occurred.

Comparison of Figures 5.6(a) and (b) identifies damage sites initiated by bulk inclusions. These sites include the bulk damage as well as rear-surface damage caused by beam modulation from the bulk damage. Because rear-surface damage grows at ~10x the bulk growth rate, the obscured area due to inclusions is dominated by the resulting rear-surface damage. In Figure 5.6, the damage sites attributed to bulk inclusions appear larger than most damage associated with surface initiators. No difference in rear-surface growth rates was observed, however, between surface and bulk-initiated rear-surface sites. The large size of inclusion-related sites results from the low-damage thresholds of the inclusions. The inclusions damage at very low fluences (1–2 J/cm^2) and therefore grow over more pulses than damage

ECMS NO CM RELEASE 20070611 14:14 0017657 OA (pdf format)

initiated at higher fluences later in the campaign. In fact, most of the inclusion-related damage in lens 01K was initiated during the earlier low-fluence tripling campaign.

The most relevant 351-nm damage growth data obtained in off-line test was from a test using the OSL laser (Milam and Genin). A representative rear-surface growth rate measured at 9 J/ cm^2, 3 ns, is included in Figure 5-9. The OSL growth rate is 20x to 50x lower than what would be predicted from extrapolation of the Beamlet data. Several differences must be noted between the OSL and Beamlet data. The Beamlet studies were done in a vacuum environment using a large-aperture sol-gel coated lens produced by NIF-qualified vendors. The OSL study was performed in air on a 2-in., uncoated substrate from a back-up vendor. The influences of environment, (contaminated) AR-coating, and substrate source on growth rate have not yet been determined.

The 3ω reflectance was measured on the plano input surface of RFL01K after the HDT2 campaign. Figure 5-10(a) shows the reflectance spectrum (s polarized). For comparison, the DMS map showing obscurations is also included as Figure 5-10(b) (identical to Figure 5-5[a]). Both the photometry image and the DMS map are oriented with the upper north corner of the optic on the upper left.

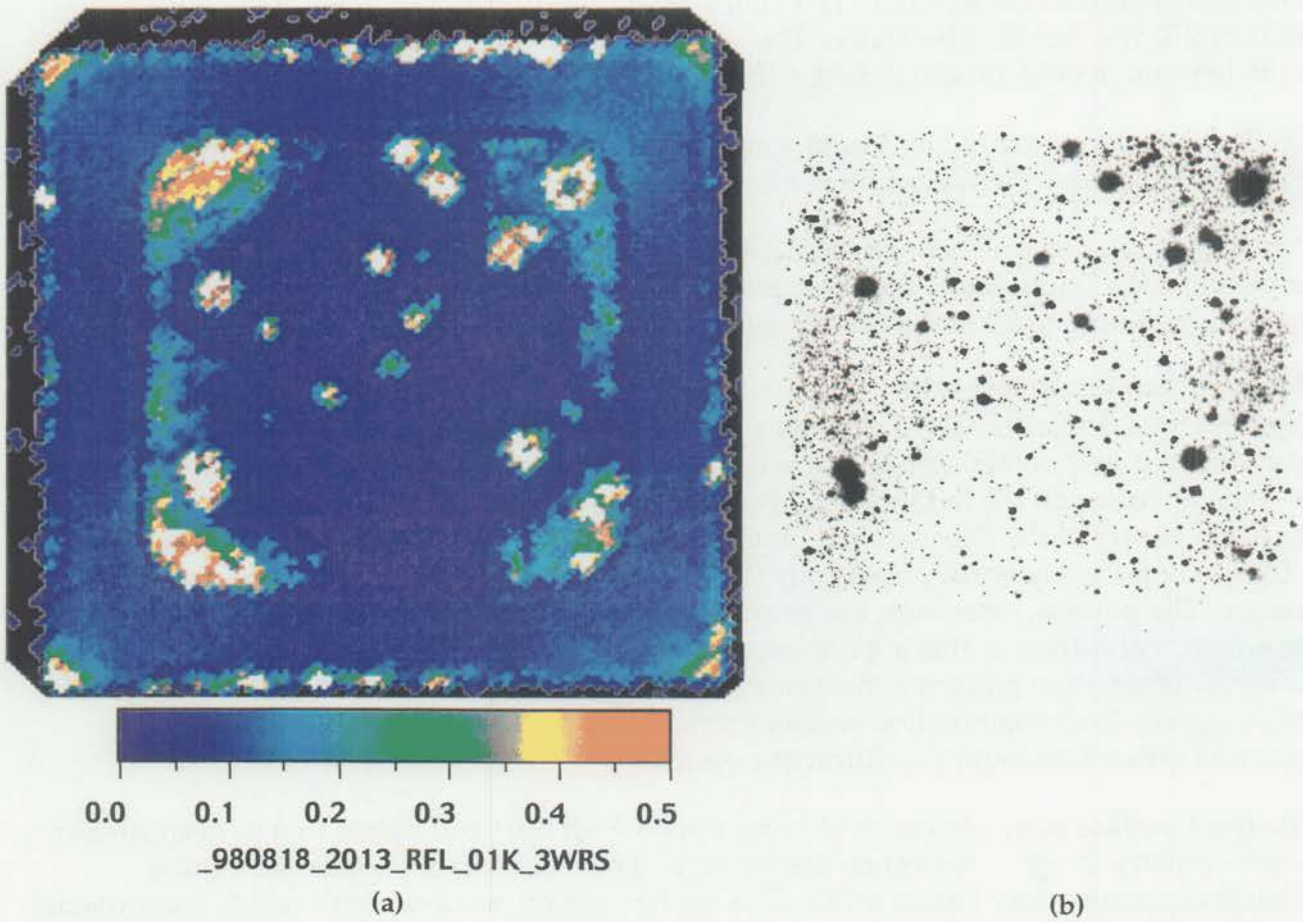

Figure 5-10 (a). 3ω reflectance of RFL01K after HDT2 campaign and (b) DMS map of RFL01K after HDT2 campaign.

ECMS NO CM RELEASE 20070611 14:14 0017657 OA (pdf format)

Several observations are apparent when these two images are compared:

- Reflectance of the lens is very low (<0.1%) in areas without large damage sites. It may be that the tight spacing between the tripler and the lens protects the lens input surface from hydrocarbon contaminants in the FOC.

- Measured reflectance is higher at many of the major damage sites on the lens that are known to be diffuse scattering. This suggests the reflectance measurement is picking up diffuse scatter and cannot be completely trusted on highly damaged optics such as RFL01K.

Higher reflectance is observed in all four corners of the optic, both within and outside the HDT2 beam footprint. This may be due to plumes of contamination coming into the tripler/lens gap from the relatively open corners.

5.1.5 Debris Shield (no diffractive optics)

Background

Two debris shields were tested. The debris shield tested along with the diffractive optics plates (DS02B) will be described later. The last four shots of the HDT2 campaign included both the lens and a new, untested debris shield (DS03K), but no diffractive optics.

DS03K was manufactured by Kodak using the same process as that used for the DOP2(KPP) substrate. Neither of these two parts was damage tested prior to use on Beamlet.

Prior to installation on Beamlet, DS03K was sol-gel coated and then photometry-mapped. After the part was illuminated with four pulses in the mule it was removed from Beamlet, mapped in the photometer and then damage-mapped in the 3ω Lab.

Beamlet illumination results

Photometry taken after HDT2 showed a loss of about 4% transmittance with clear evidence of laser cleaning within the laser aperture (shown in Figure 5-11[a]). Most of the light loss was outside the aperture on the left (north) side of the beam. The pattern of the light loss in the upper north corner of the debris shield matched the location and pattern of a massive damage site observed on the kinoform phase plate (KPP) during the earlier integrated portion of the campaign. The pattern, extending inside and outside the HDT2 beam footprint, appears to the eye as a region of diffuse scattering **not** associated with discrete damage sites. The existence of a similar contamination pattern at the same location with and without diffractive optics in the system suggests the contamination was associated with the Beamlet beam and optics conguration rather than with the diffractive optics.

The front surface of the debris shield was coated with dust and debris in a pattern similar to the photometry image—dirtiest on the left side. The rear surface showed no similar particulate contamination (Figure 5-12). This contamination occurred both inside and outside

ECMS NO CM RELEASE 20070611 14:14 0017657 OA (pdf format)

the beam aperture. The input surface was presumably contaminated by debris from the output of the lens, ~42 cm upstream.

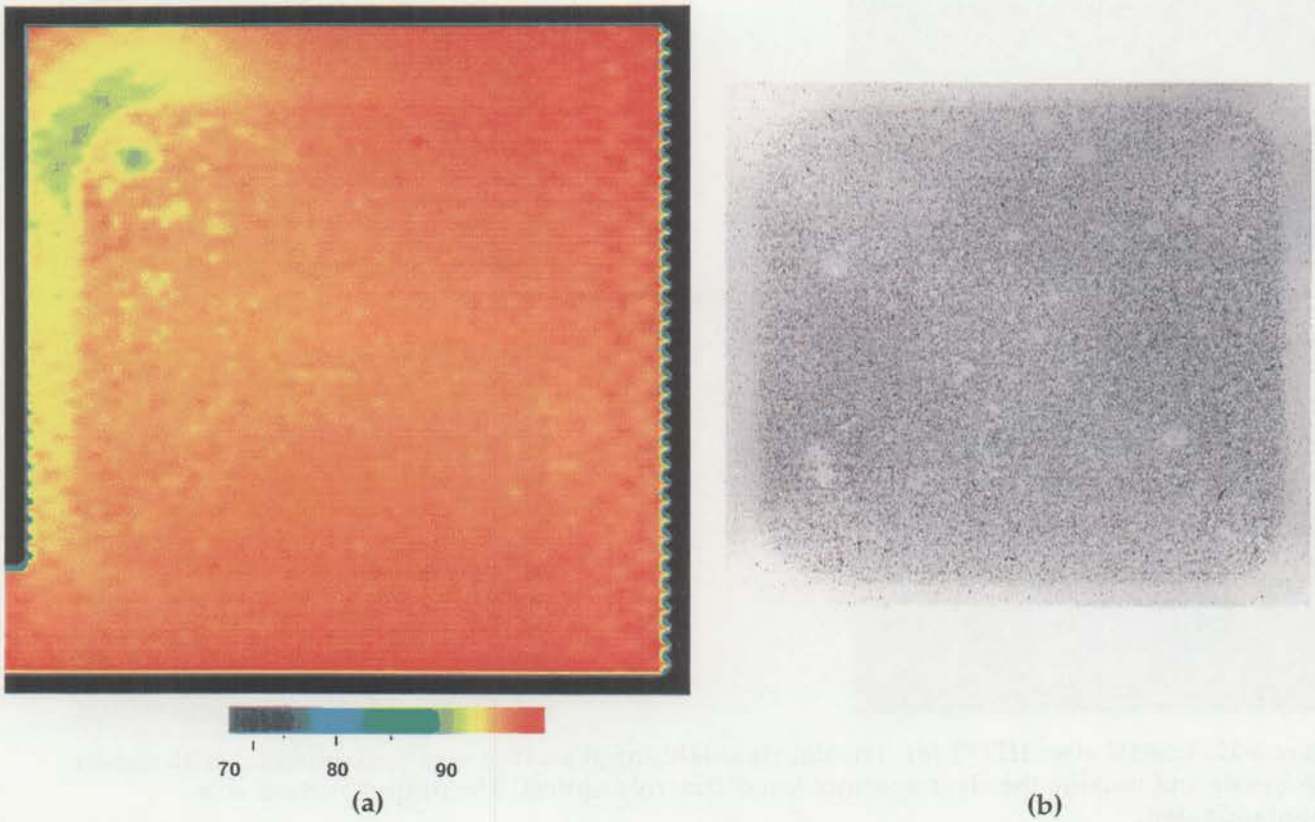

Figure 5-11 (a). DS03K transmittance photometry at 3ω and (b) DS03K DMS map with sensitivity turned up to emphasize pinpoint damage sites.

Inspection of DS03K indicated small damage sites on both surfaces of the debris shield. Figure 5-11b shows the DMS map for DS03K. In this map, the camera sensitivity and lighting were turned up so the large number of very small (mostly <50 μm) defects would be visible in the map. It is clear in the DMS map the large damage sites in up-stream optics (lens and tripler) did not cause modulation-induced damage on the debris shield. The upstream sites instead acted as beam obscurations resulting in **undamaged** areas on the debris shield. The front surface of DS03K contained a few dozen relatively large (~100 μm) damage sites both inside and outside the HDT2 beam footprint. These sites appeared to be caused by spitting from the lens.

ECMS NO CM RELEASE 20070611 14:14 0017657 OA (pdf format)

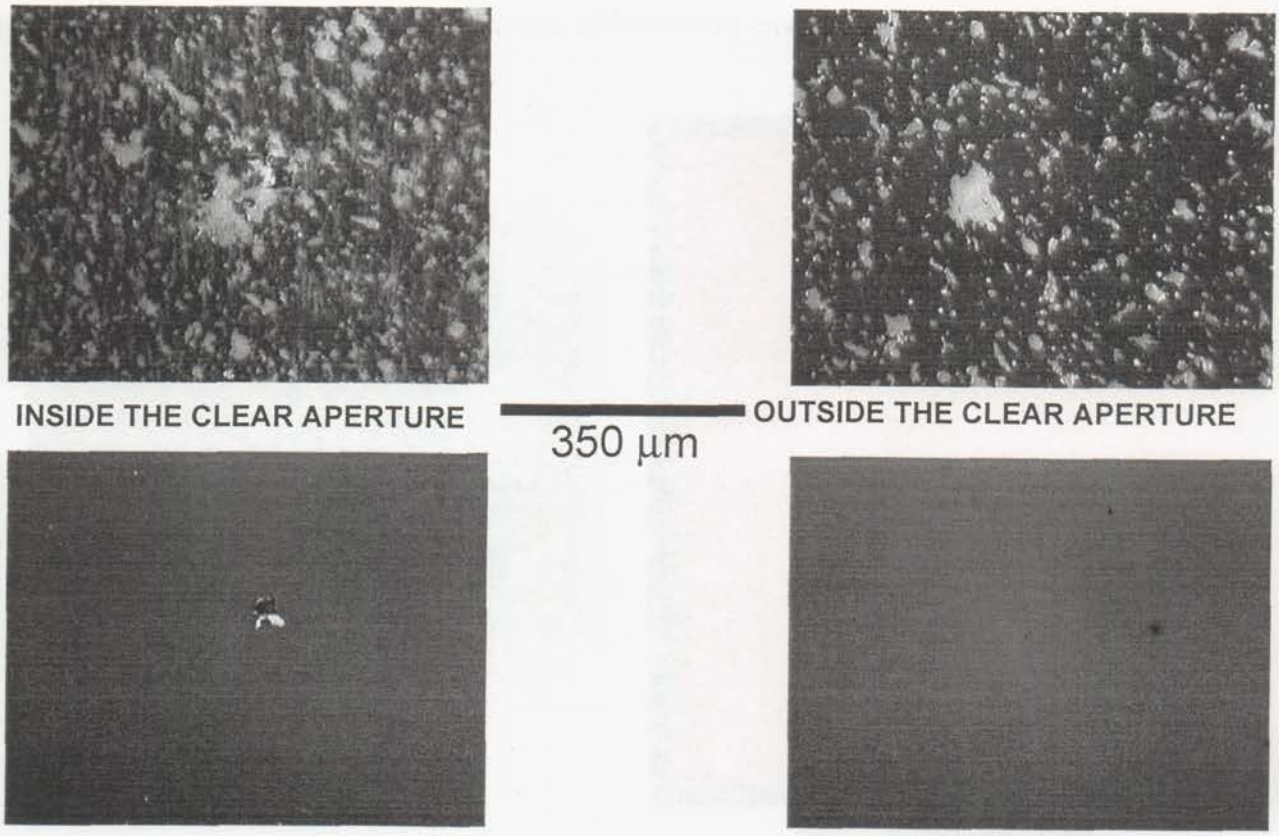

Figure 5-12. DS03K after HDT2 (d). The debris shield input surface was contaminated with debris both inside and outside the clear aperture (no diffractive optics). The output surface was uncontaminated.

5.2 Diffractive Optics Damage

In HDT2 phase (b), six shots were taken with the fully integrated NIF optics package set up in an approximation of the NIF configuration. In addition to the final optics cell, the configuration included two DOPs and one debris shield. DOP1 contained a full-aperture color separation grating (CSG) on the input surface and a beam sampling grating (BSG) on the output surface. DOP2 contained a 16-level discrete kinoform phase plate (KPP) on the input surface and no diffractive structure on the output surface. Figure 5-13 depicts the optics configuration used in this portion of HDT2.

Two of the six shots were ramping shots, and four were at near-NIF fluence: 7–8.5 joules/cm^2. The two diffractive optic plates and the debris shield were removed for damage analysis because of the large amount of damage apparent from these six shots. Figure 5-14 shows DMS maps from the lens, DOP1, DOP2, and the debris shield DS02B along with the near field image of the last diffractive optics shot. Both DOPs and the debris shield were damaged sufficiently in six shots to warrant removal for analysis. Damage was primarily on the rear surfaces of each DOP and the downstream debris shield.

ECMS NO CM RELEASE 20070611 14:14 0017657 OA (pdf format)

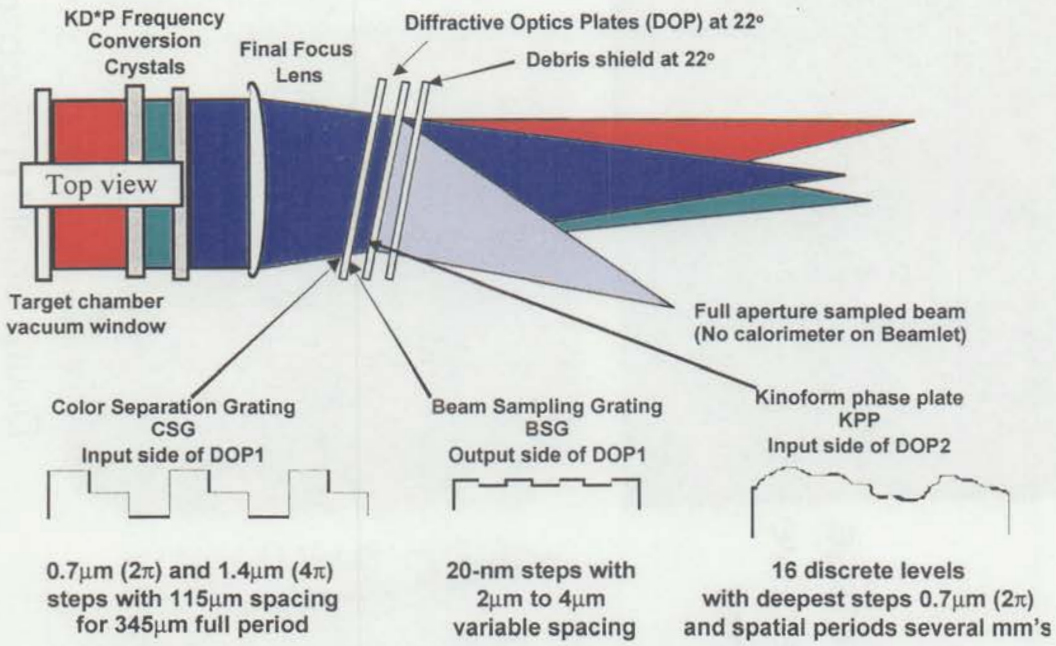

Figure 5-13. Three diffractive optics fielded on Beamlet in nearly the current NIF baseline configuration.

ECMS NO CM RELEASE 20070611 14:14 0017657 OA (pdf format)

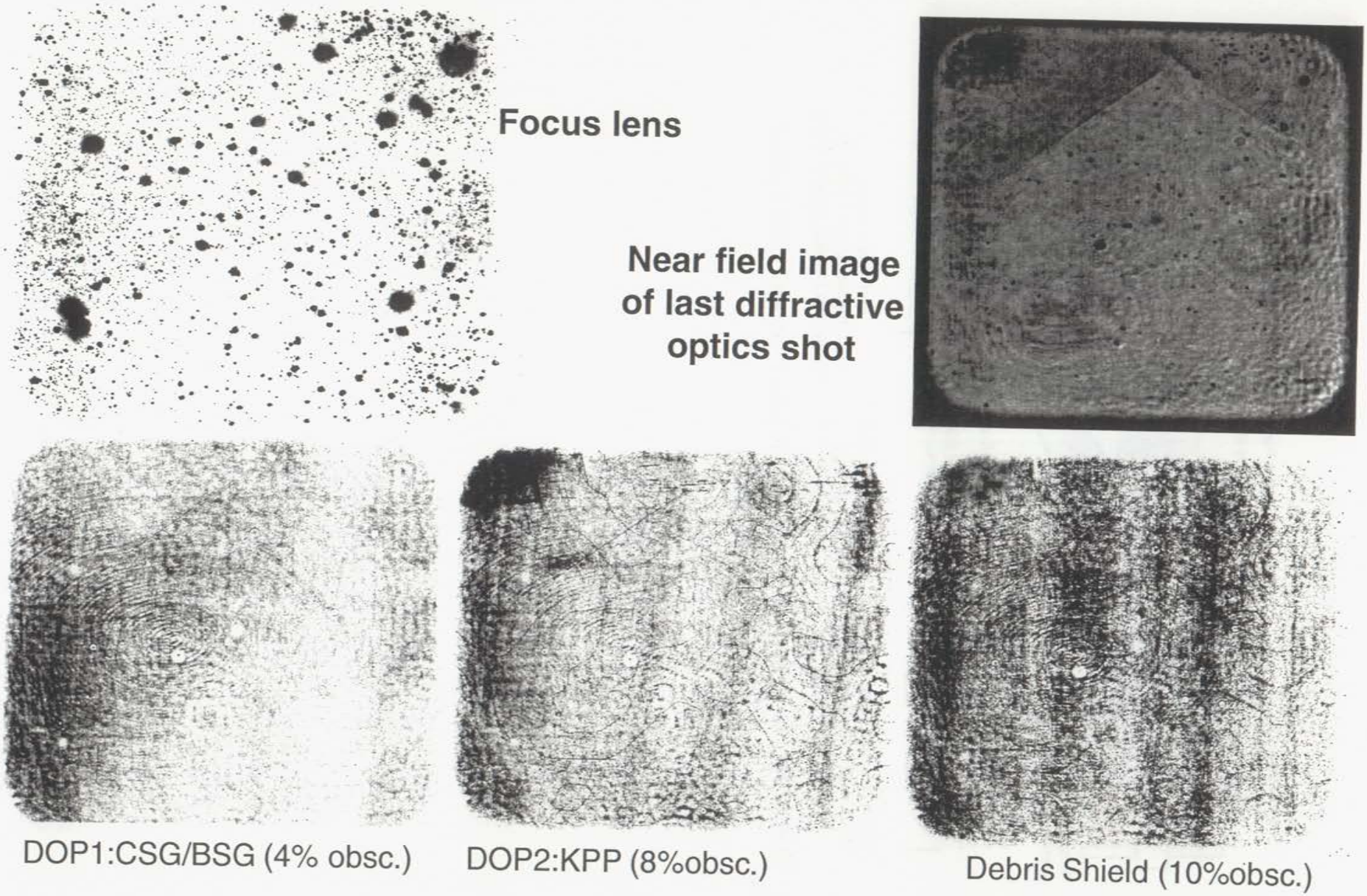

Figure 5.14. Significant damage observed on both DOPs and debris shield. Obscuration increased with each optic in the chain.

ECMS NO CM RELEASE 20070611 14:14 0017657 OA (pdf format)

DOP1:CSG/BSG

The CSG pattern on the input surface was a stair-step grating with a period of 345 μm in three 115-μm steps. Two of the steps were 2π (0.7μm) in height, and one was 4π (1.4μm). The grating was not a split pattern, but it was of a period similar to that required by the NIF baseline split design. The grating was coated with a dipcoated colloidal sol antireflection (AR) coating. The BSG on the output surface of DOP1 had much smaller features—about 20-nm deep with a variable period of about 2 μm.

After the six Beamlet shots, the rear surface of DOP1 was covered with a very large number of damage sites as shown in Figure 5-15. The damage patterns mimicked the modulation patterns already apparent in the Beamlet beam in the near-field shot prior to the introduction of the DOPs (Figure 5-16). Essentially, all modulation high spots in the beam were written into the rear surface of DOP1. The damage image was composed of a pattern of damage sites spaced typically 350 μm apart—the same as the 4π-line spacing in the CSG (Figure 5-17).

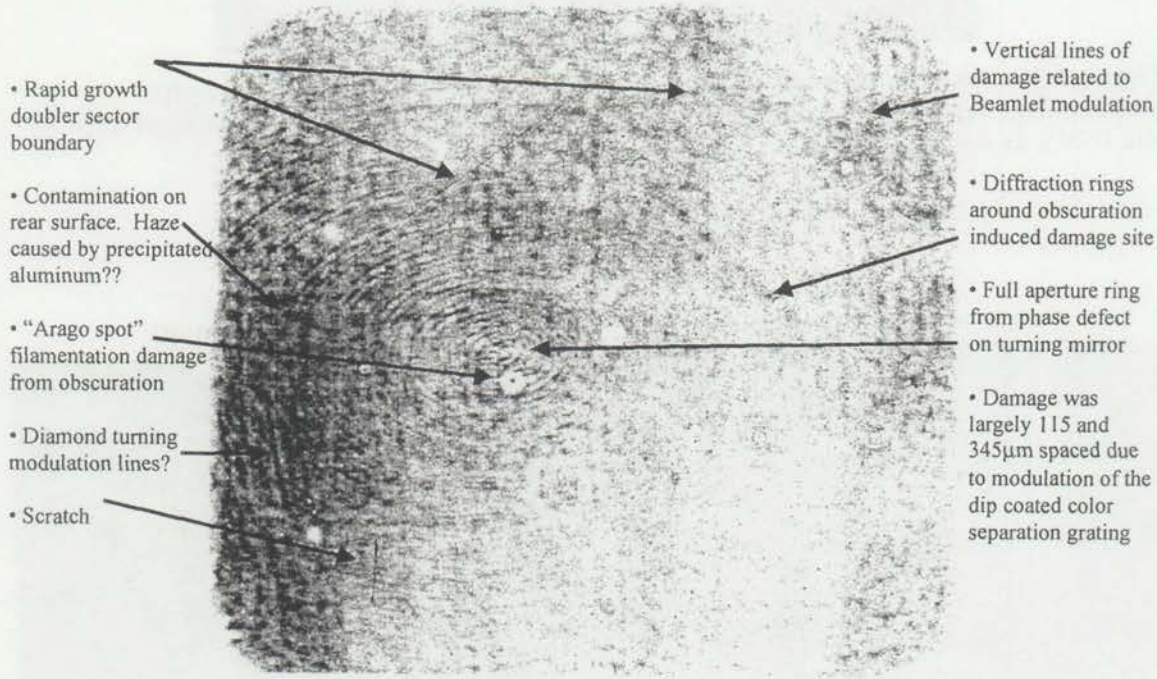

Figure 5-15. DOP1 after HDT2. The color separation grating (CSG) was on the input surface; the beam sampling grating (BSG) was on the output surface.

ECMS NO CM RELEASE 20070611 14:14 0017657 OA (pdf format)

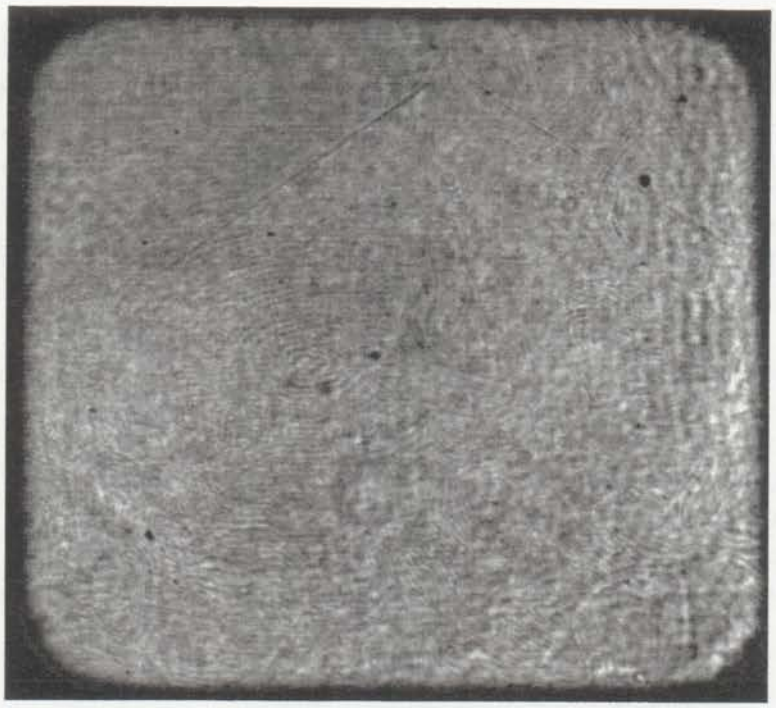

Figure 5-16. Near-field image from the first D.O. shot, flipped to match optics positioning. Upstream modulations already present in the beam were 'printed' into the DOPs as damage sites.

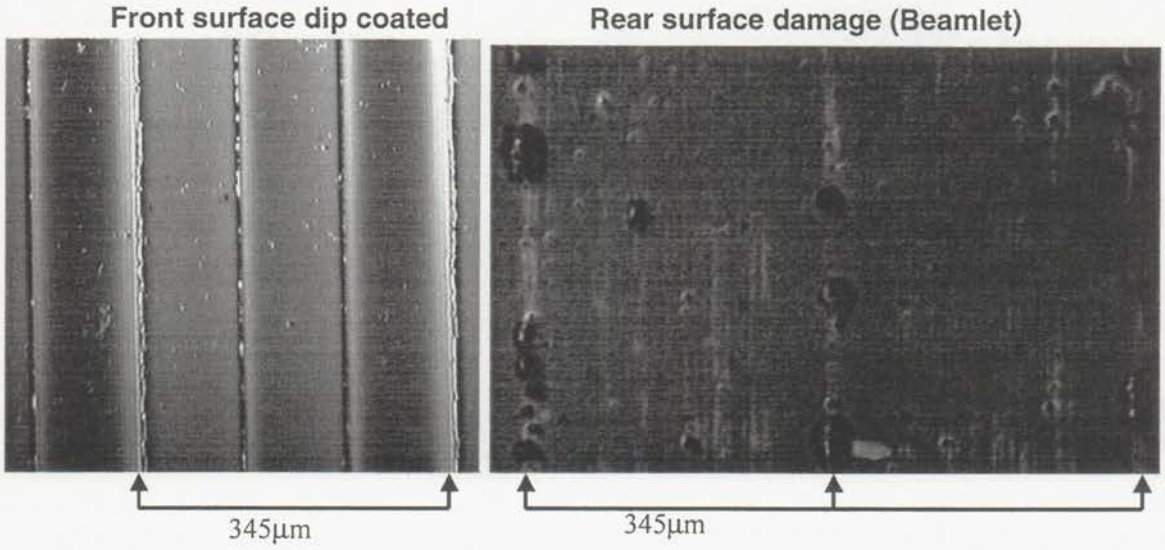

Figure 5-17. DOP1 [CSG/BSG] after HDT2. The largest sol-gel defect occurred every 345 μm at the 4π jump. Rear-surface damage was usually, but not always at the 345-μm period.

ECMS NO CM RELEASE 20070611 14:14 0017657 OA (pdf format)

Modulation-induced damage sites included:

1. A large elliptical diffraction ring associated with a phase error in a turning mirror (Figure 5-18).

2. Two lines associated with a rapid-growth doubler sector boundary (Figure 5-19).

3. Small Fresnel diffraction rings from upstream modulation sites (Figure 5-18).

4. Wavy lines of damage apparent in the near-field pattern that are suggestive of the spatial filter pinhole cutoff period (Figure 5-15).

5. A large diameter pattern possibly associated with diamond turning marks on a KDP crystal (Figure 5-15).

6. Localized damage sites from upstream modulation around point defects (Figure 5-18).

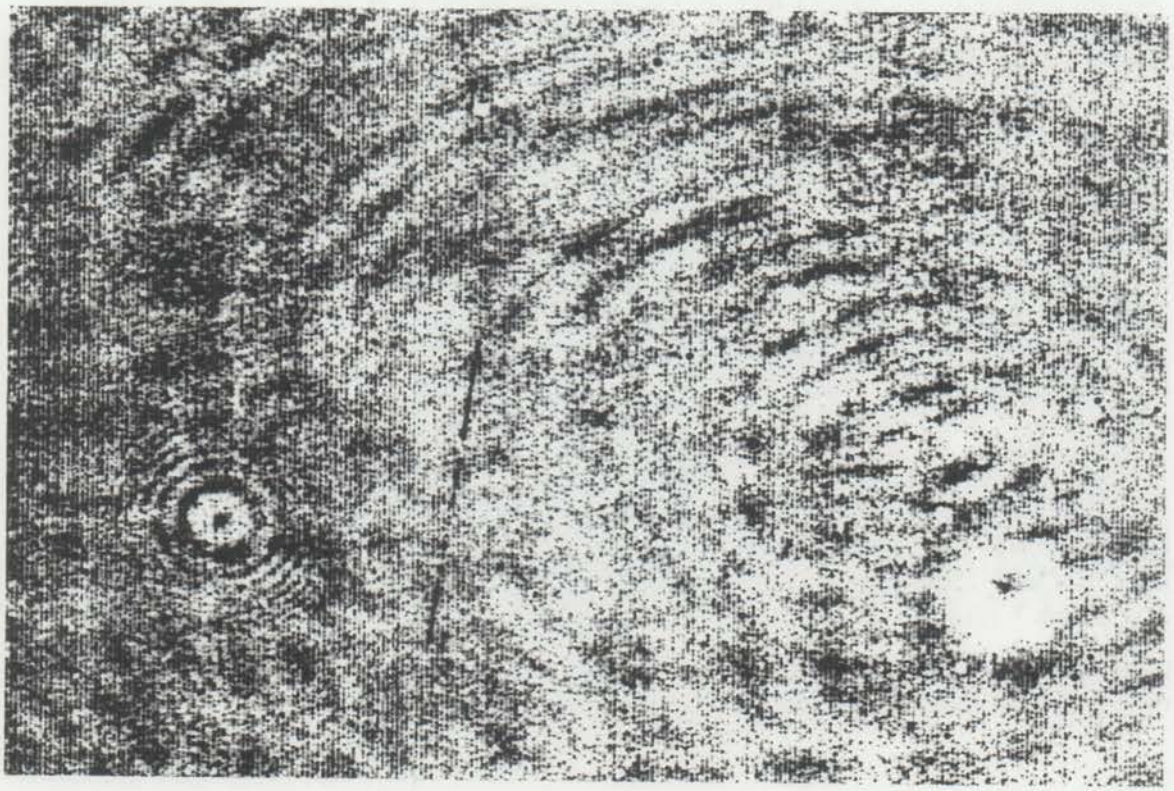

Figure 5-18. Beamlet modulations are painted on the rear surface of the CSG in dashes of damage sites at 115 and 345-μm spacing.

Unlike the lens, there was little or no direct correlation between damage on DOP1 and the large KDP tripler damage sites or KDP-associated sites on the lens. Instead, there were numerous protected areas of zero damage (Figure 5-20)

ECMS NO CM RELEASE 20070611 14:14 0017657 OA (pdf format)

where it was apparent the DOP saw little or no laser fluence. This suggests many of the large KDP-associated damage sites on the tripler and the lens caused high-angle modulation that died off before reaching DOP1. These spots of non-damaged area are similar to those seen on the debris shield DS03K during HDT2 phase (d) after the diffractive optics were removed (Figure 5-11b).

Photometry showed a large variation in transmission loss across the laser aperture ranging from 0–35% and averaging about 4% (Figure 5-21a). The loss was strongest on the left side (north). DOP1 showed significant (~5 to 10%) transmission loss outside the laser aperture. This loss appeared to be due to diffuse scatter from particulate, based on optical micrographs and appearance to the unaided eye. The strongest loss outside the aperture was on the left (north) side in a pattern similar to that observed on the debris shield used in the nondiffractive optics portion of the campaign (DS03K). There was evidence of diffuse scattering on the rear of DOP1 in this high-loss area.

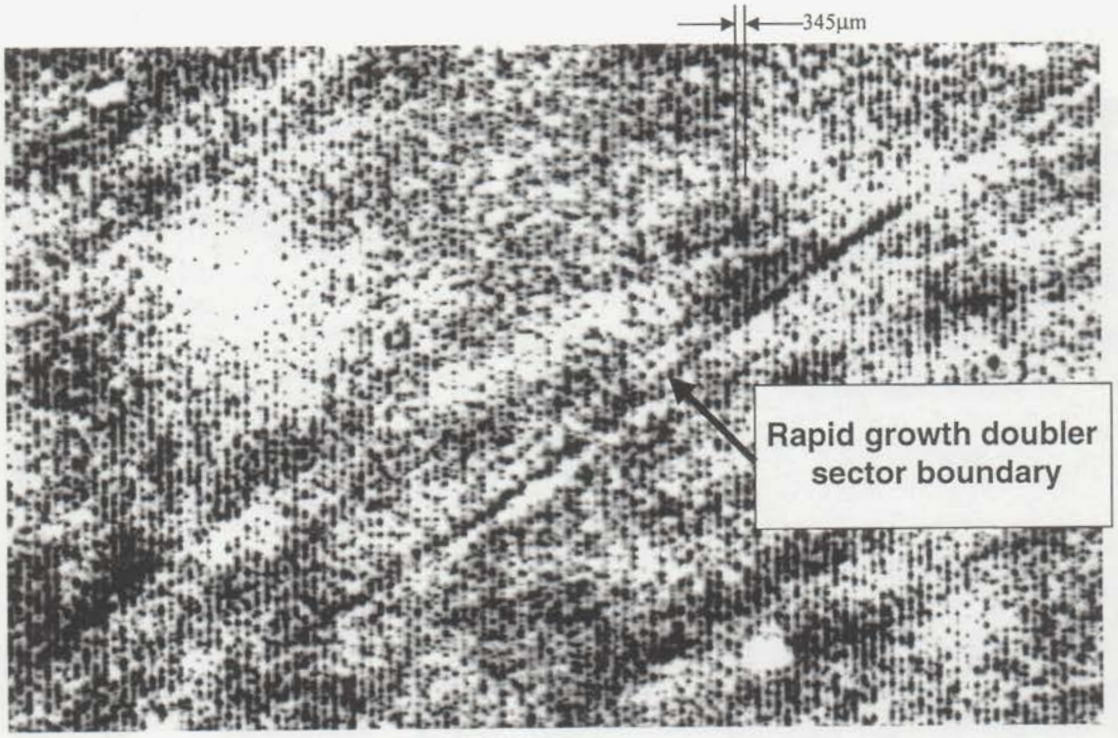

Figure 5-19. DOP1 (CSG/BSG). Beamlet modulations were painted on the rear surface of the DOP1 in dashes of damage sites at 345-μm spacing.

ECMS NO CM RELEASE 20070611 14:14 0017657 OA (pdf format)

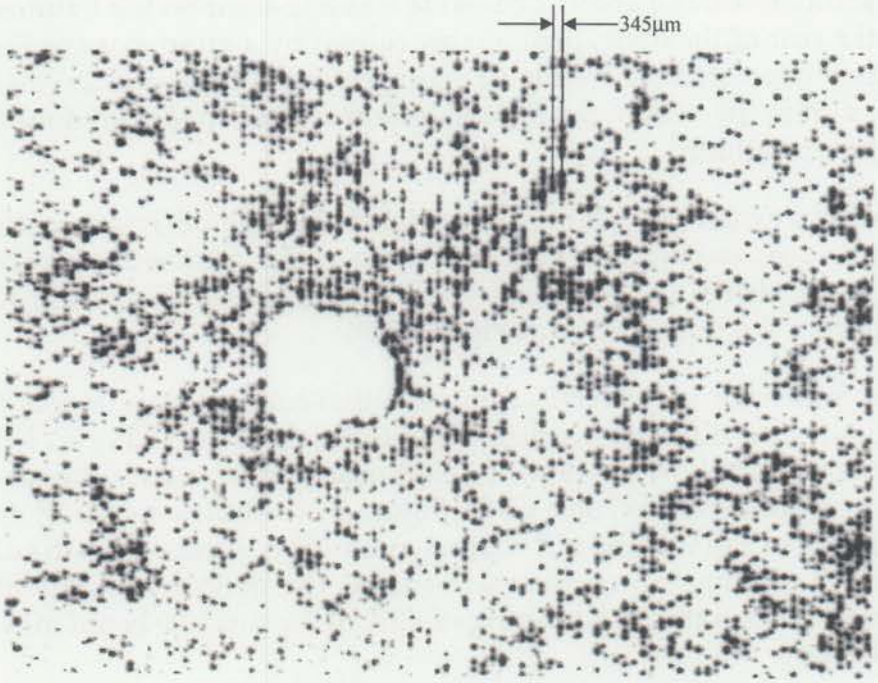

Figure 5-20. Soft-edged obscurations left windows of nondamaged areas through the chain of downstream optics.

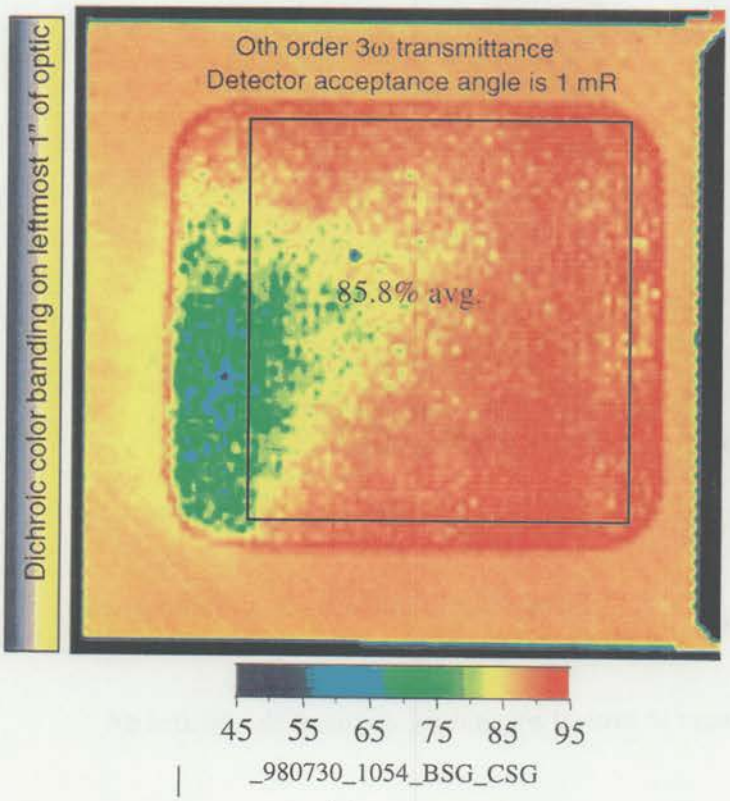

(a)

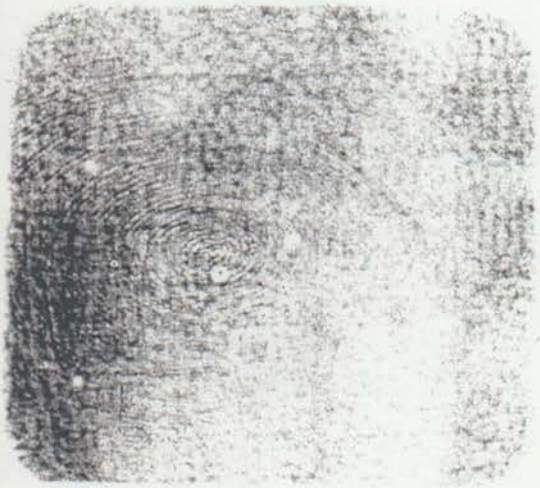

(b)

Figure 5-21 (a). Transmittance at 3ω for DOP1(CSG/BSG) after HDT2. The damage resulted in ~4% drop in specular transmission and (b) DMS map of DOP1: CSG/BSG.

ECMS NO CM RELEASE 20070611 14:14 0017657 OA (pdf format)

A visible dichroic band about 2 cm wide was apparent on the leftmost (north) portion of the rear of the optic, presumably caused by a quarter-wave film of contamination deposited coherently. This is presumed to be due to volatilization of aluminum from the wall of the fixture, but no analysis has been done to support this supposition.

There was no evidence of damage associated with the BSG pattern, but no technique was used having sufficient resolution to observe the 2-μm periodicity of this grating. Calculations done after the HDT2 campaign (I. Barton) suggest modulation from the BSG may be as high as 30%.

It was known prior to the HDT2 campaign that colloidal sol AR coatings do not conformally coat diffractive structures of the scale of the CSG and KPP. Figures 5-22 and 5-23 show the type of defect observed when traditional colloidal sol AR coatings are deposited on a CSG. Figure 5-24a shows the 3ω 0th order transmittance of a CSG with no AR coating, with AR coatings on both surfaces, and with an AR coating only on the rear surface. The nonconformality of the coating results in the forward scattering of ~9% of the total 3ω beam into higher diffractive orders.

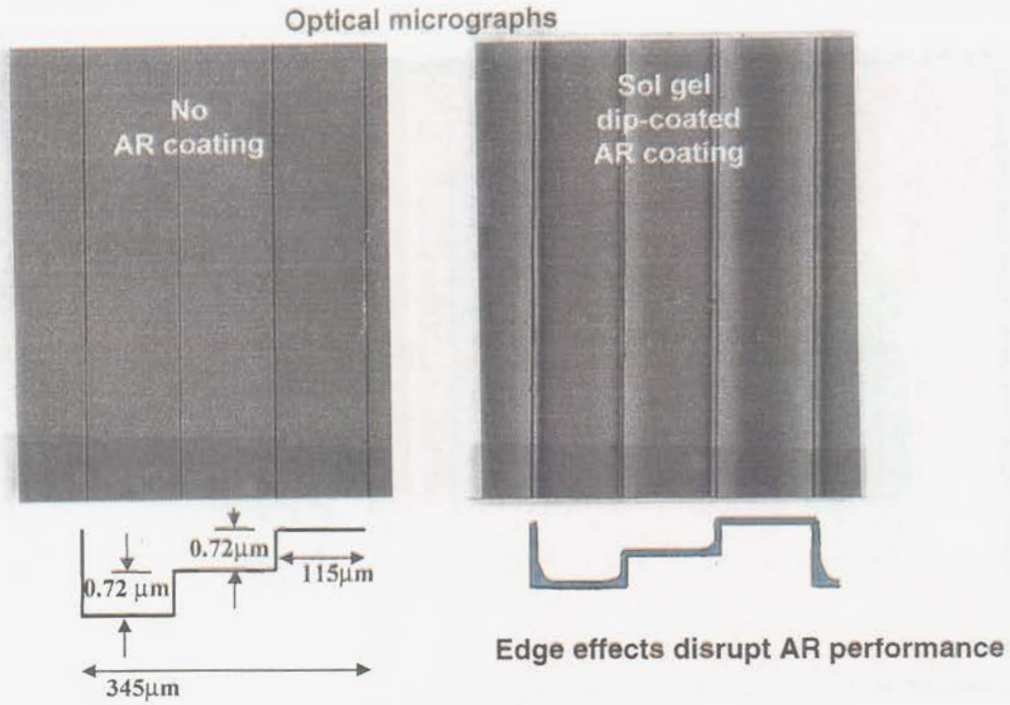

Figure 5-22. The los in AR performance is caused by coating errors at the 2π and 4π steps of the CSG.

ECMS NO CM RELEASE 20070611 14:14 0017657 OA (pdf format)

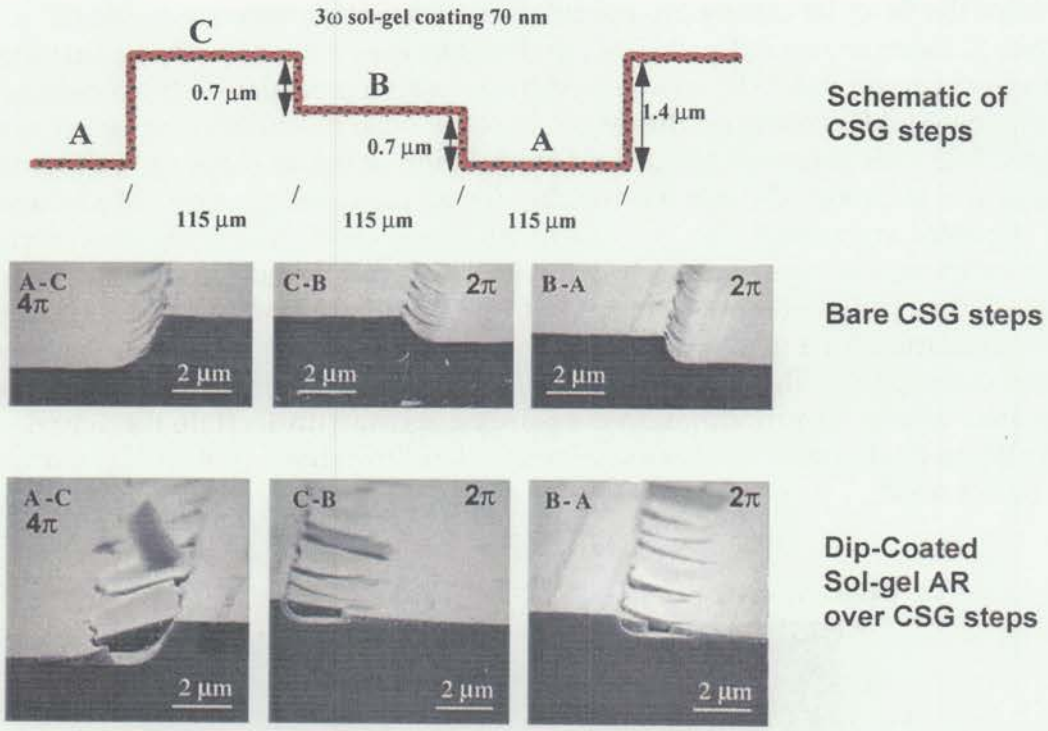

Figure 5-23. SEM micrographs of dip-coated CSG steps show planarization, crazing of thick sol-gel layer at steps.

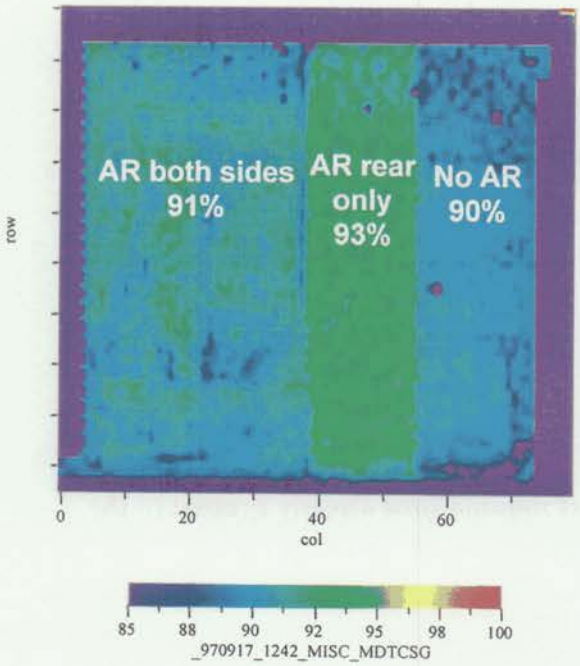

5.24(a)

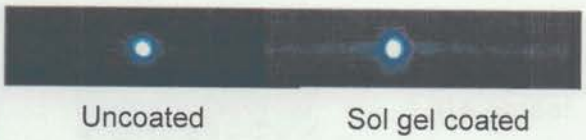

Figure 5.24(b). Photographs of the transmitted beam of a CSG with and without AR coating on the grating surface. Coated grating diffracts ~9% into higher orders.

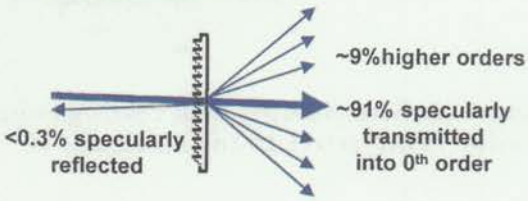

Figure 5.24(c). Cartoon depicting forward scattering/diffraction of 3ω light from an AR-coated CSG.

Figure 5-24(a). Transmittance of 3ω zeroth order transmittance (1 mR acceptance angle) of CSG with colloidal-sol AR-dipcoated on both surfaces, nongrating surface only, and neither surface.

ECMS NO CM RELEASE 20070611 14:14 0017657 OA (pdf format)

After the Beamlet campaign, modulation measurements were made (J. Britten, S. Herman) on subscale CSG gratings to verify the hypothesis that the damage observed in HDT2 was caused by excessive modulation from defects in the dipcoated AR coating on the larger 4π steps. The modulation measurements (Figure 5-25, 5-26) showed about 1.5× modulation at the 4π steps for a dipcoated grating and substantially less modulation for an uncoated grating. Modulation was apparent at 2π steps also, but at a much lower level. Modeling was carried out to estimate the expected modulation for bare and coated gratings. (I. Barton, Figure 5-27). The model predicted about 1.5× modulation with no coating and 2.7× modulation for a grating with edge-width errors similar to those observed on dipcoated parts. The calculated modulation is significantly higher than the measured values. The modulation measurements may understate the actual modulation peak intensity because of resolution limitations of the CCD camera and optics used.

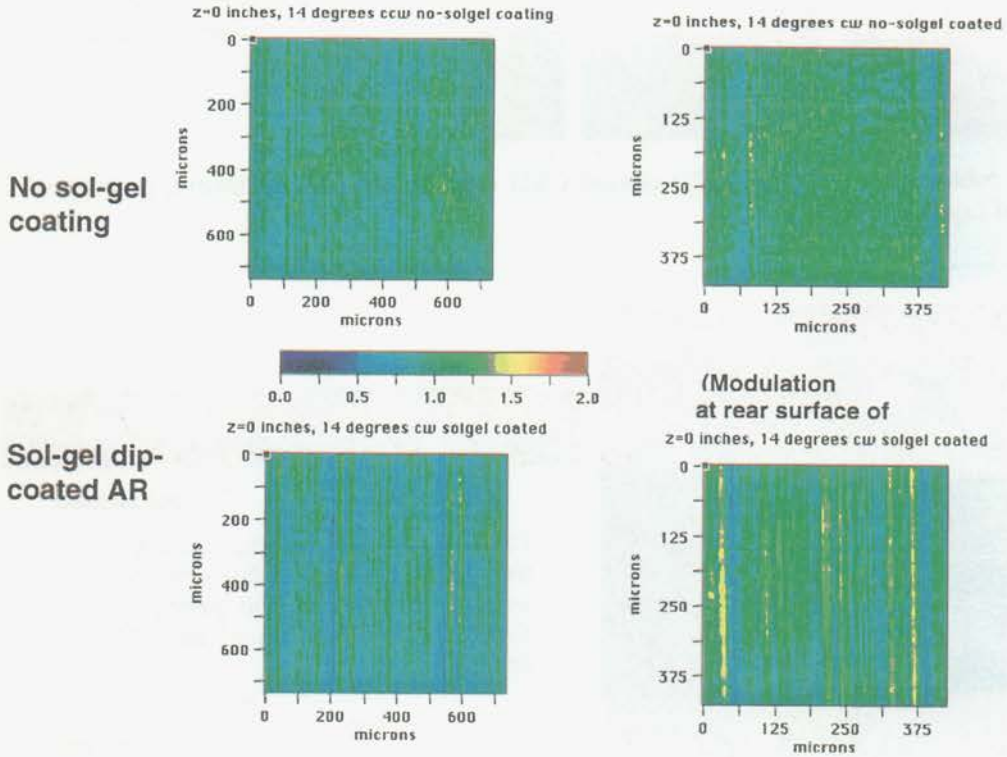

Figure 5-25. The disrupted AR coating enhances modulations already present in the CSG due to imperfect 2π and 4π steps.

ECMS NO CM RELEASE 20070611 14:14 0017657 OA (pdf format)

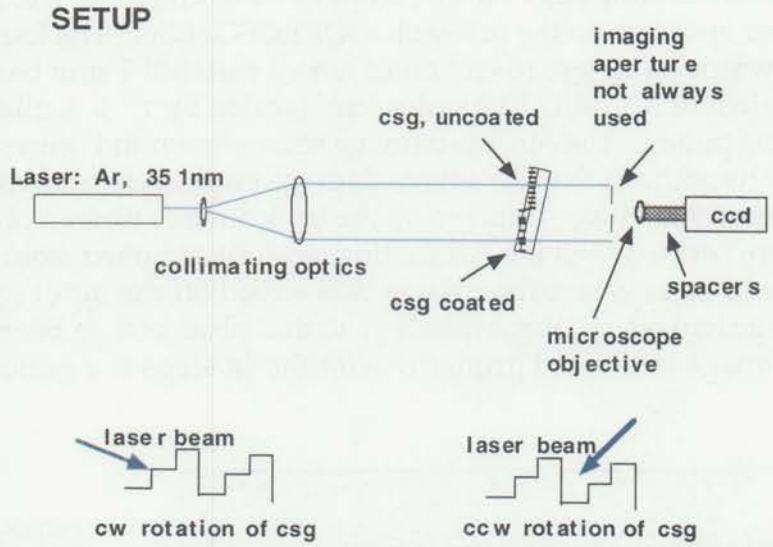

Figure 5-26. Modulation due to the CSG steps measured using the 351-nm Ar laser on the beam sampling grating exposure station. Measurements may underestimate modulation due to resolution limitations.

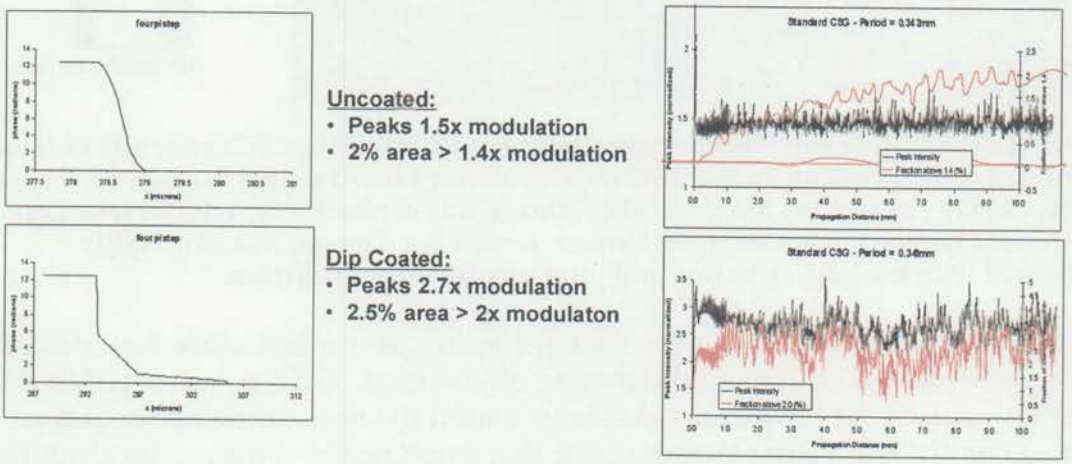

Figure 5-27. Modulation calculations of 343 μm stair-step CSG. The model predicts modulation peaks are >3× higher (+170% vs. +50%) when a nonconformal dipcoated AR coating is on the grating surface.

ECMS NO CM RELEASE 20070611 14:14 0017657 OA (pdf format)

After the Beamlet campaign, off-line damage measurements were made outside the laser aperture on the full-scale DOP1:CSG/BSG. The Large Area Test (LAT) system was used to test 10-cm^2 areas with a rastered 1-mm beam in air at the 3-ns equivalent of 8.3, 10.1, 12.3 joules/cm^2 (scaled by $\tau^{1/2}$). Actual testing was done with 7.5-ns pulses. The off-line damage tests, shown in Figures 5-28 and 5-29, verified the hypothesis that the severe damage on Beamlet was exacerbated by the dipcoated AR coating. Damage on the back surface was an order of magnitude more severe when the AR coating was not removed from the input surface relative to areas where the coating was wiped off the input (grating) surface. Damage had a similar morphology to that observed on Beamlet with the rear-surface damage associated primarily with the 4π steps at a period of 350 μm (Figure 5-30).

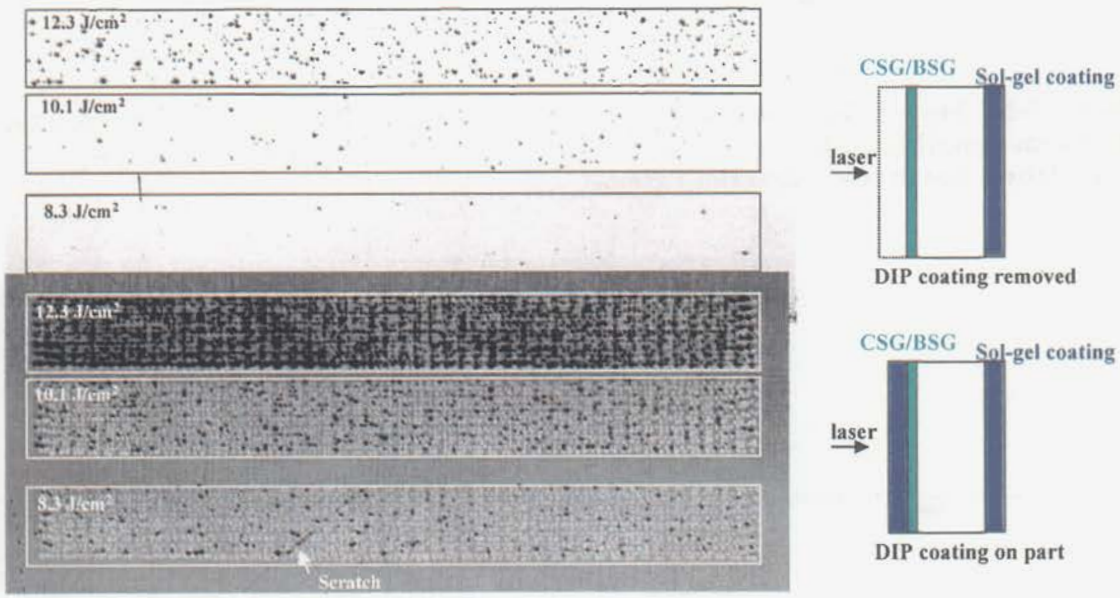

Figure 5-28. Off-line small beam raster testing of DOP1 (BSG/CSG) after HDT2. The disrupted sol-gel coating on the CSG (input surface) caused severe damage on the rear surface at 115 μm and 345 μm intervals. Damage was dramatically reduced when the sol gel was removed from the front surface; remaining damage was still highly correlated with the grating period and primarily on the rear surface.

It is possible the off-line raster tests are overly pessimistic since the uncoated areas were created by wiping the coating off by hand. Off-line testing of DOP1 after it was used for HDT2 may also have biased the tests unfavorably due to damage on the front surface of the optic that could not be removed by cleaning (observed during subsequent tests of DS03K). These tests should be repeated with gratings that have never been coated to ensure no negative bias from coating and wiping. Alternatively, the off-line test may underestimate the damage density for large-aperture systems. Modeling calculations are under way to estimate how much of the modulation error can be accurately sampled with the ~1-mm Gaussian beam vs. the 345-μm period of the current grating.

ECMS NO CM RELEASE 20070611 14:14 0017657 OA (pdf format)

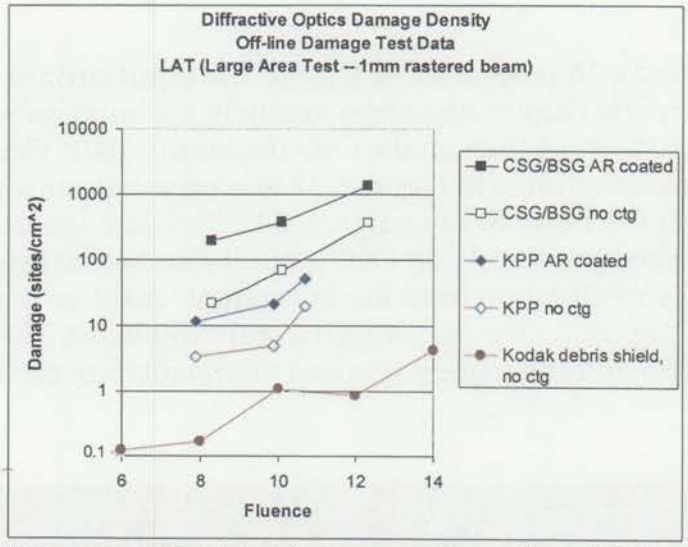

- CSG/BSG== color separation grating/beam sampling grating on DOP1
- KPP == kinoform phase plate on DOP2
- All plotted damage is rear surface damage; front surface damage did occur, but at about an order of magnitude lower frequency
- The AR (antireflection) dip coating was on the front/input surface
- Uncoated surfaces were obtained by wiping off the coating

Figure 5-29. Comparison of off-line test data from DOP1 (CSG/BSG) and DOP2(KPP) after HDT2. Data measured on 10 cm^2 areas outside HDT2 beam footprint at 7.5 ns, then adjusted to 3 ns equivalent ($\tau^{1/2}$).

- **Damage morphology of CSG/BSG with dip coating**

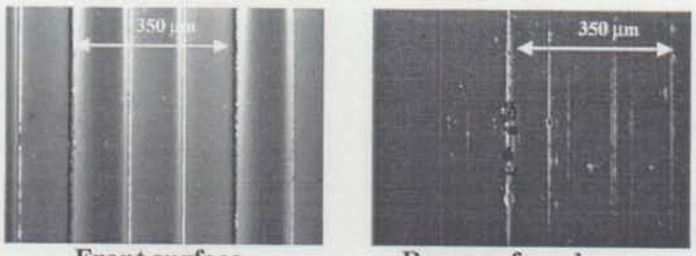

Front surface **Rear surface damage**

- **Damage morphology of CSG/BSG without dip coating on front surface**

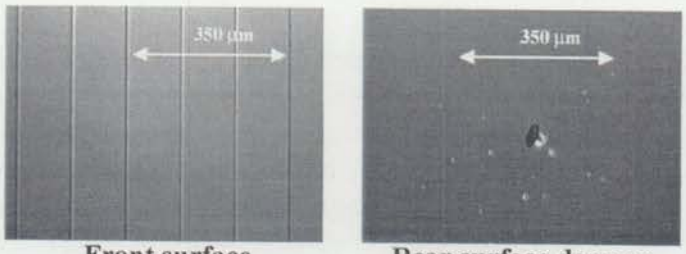

Front surface **Rear surface damage**

Figure 5-30. Damage morphology from off-line testing of DOP1(CSG/BSG) with and without dip coating on the front (grating) surface.

ECMS NO CM RELEASE 20070611 14:14 0017657 OA (pdf format)

DOP2:KPP

DOP2 supported a 16-level discrete KPP on the input surface. The deepest step on the phase plate pattern was approximately 2π, but there was a much lower density of such steps than on the CSG (factor of ~100). On the KPP, the "contour map" pattern shown in Figure 5-31 was on a scale of several millimeters. After the Beamlet campaign, DOP2 had damage analogous to all of the damage described previously on DOP1, but it also had damage on the rear surface induced by modulation from the 2π "contour map" of the KPP (Figure 5-32, 5-33). The damage on the rear of DOP2 still exhibited a 350-μm pattern induced by the CSG, but the pattern was less dominant than on the CSG (Figure 5-34).

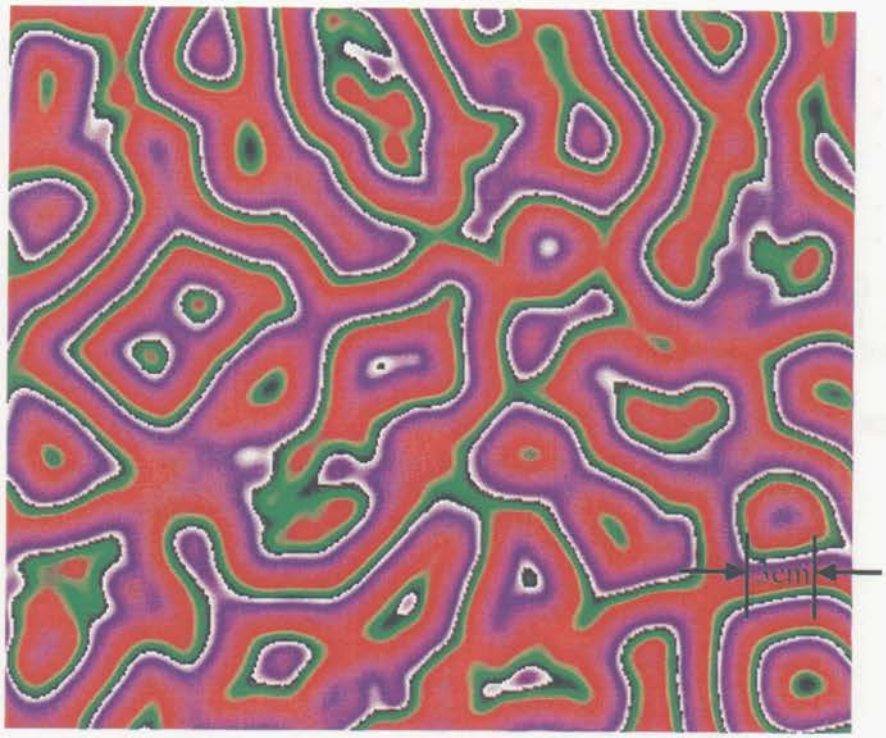

Figure 5-31. 16-level discrete kinoform phase plate design used for DOP2(KPP). Major contours represent the 2π steps.

DOP2 had a large (~5- × 5-cm) square area of severe damage in the upper left (north) corner on the rear surface (Figure 5-32). This pattern may have been caused by a small, focused ghost or by contamination on the surface. Its appearance suggested a very hot spot in the beam, but no hot spots were in that vicinity of the Beamlet aperture. This damage pattern was "spit" onto the debris shield DS02B ~4 cm away and replicated in diffused detail as surface contamination on the front of the debris shield.

ECMS NO CM RELEASE 20070611 14:14 0017657 OA (pdf format)

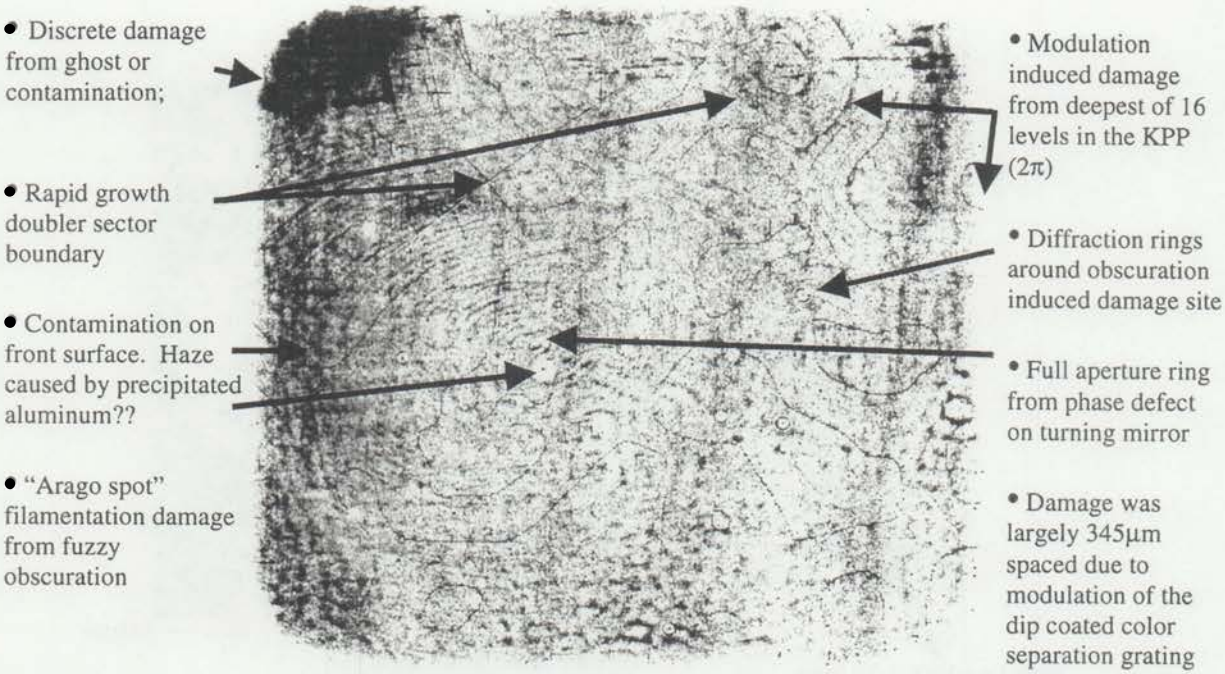

Figure 5-32. DMS map of DOP2(KPP) after HDT2 campaign. The 2π step of the kinoform phase plate was written into the rear surface of DOP2 in damage sites.

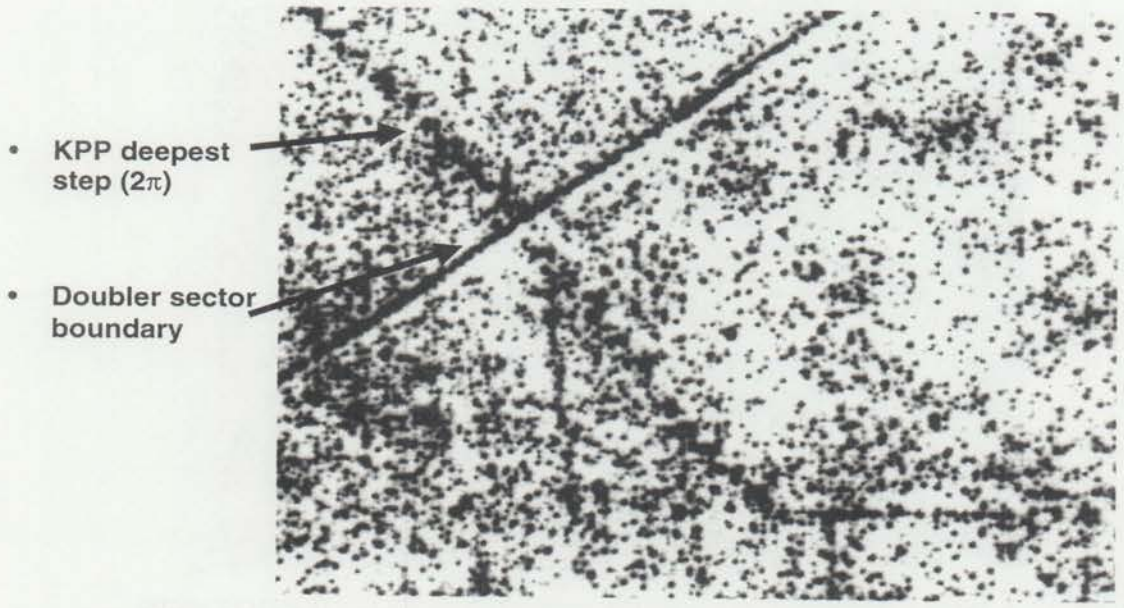

Figure 5-33. Damage on the KPP rear surface was driven by a combination of the modulation from the CSG, etc., and from the 2π steps of the KPP.

ECMS NO CM RELEASE 20070611 14:14 0017657 OA (pdf format)

Figure 5-34. KPP damage was driven by a combination of the 2π kinoform steps and the periodic modulation of the CSG. Nondamaged areas coincided with large damage sites on the lens.

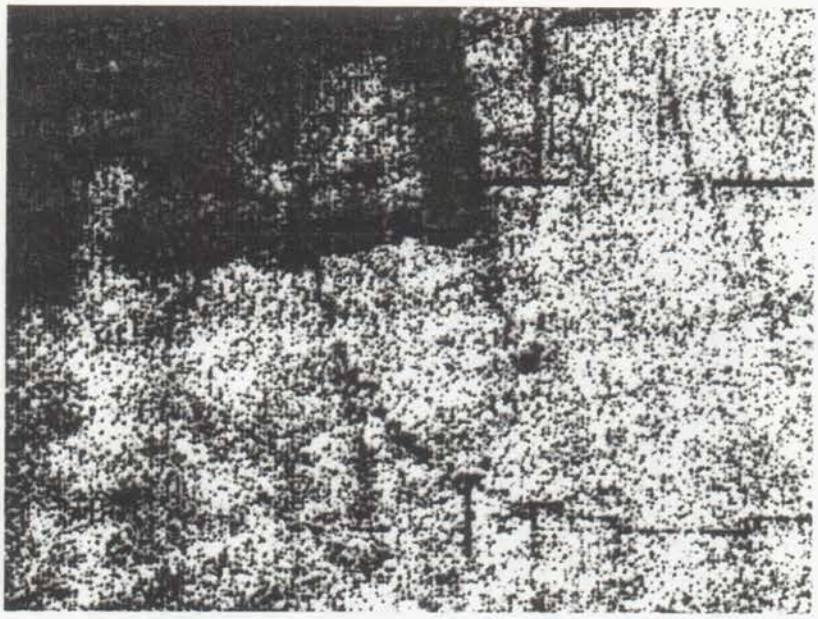

Figure 5-35. A large square of damage in the upper left corner of the DOP2/KPP output surface had sharp edges. The image of the damage was mirrored on the input of the debris shield, with some fuzzing out of the image.

ECMS NO CM RELEASE 20070611 14:14 0017657 OA (pdf format)

DOP2 had diffuse scattering due to surface contamination on the front left surface located in a pattern similar to that observed on the rear of DOP1. Micrographs of the surface in these areas showed the appearance of vapor-precipitated solid contamination (Figure 5-36).

KDP-induced front surface damage on KPP

Contaminated area on front surface of KPP

No AR coating damage outside clear aperture

Figure 5-36. Photographs of the front surface of DOP2(KPP) showed severe contamination/damage on portions of the surface.

Photometry showed about 8% transmittance loss overall, although the severely damaged 5- x 5-cm pattern on the upper left side had areas with as much as 50% loss due to scattering from damage sites (Figure 5-37). As on DOP1, the transmittance loss was highest on the left side, with evidence of contamination outside the laser aperture.

ECMS NO CM RELEASE 20070611 14:14 0017657 OA (pdf format)

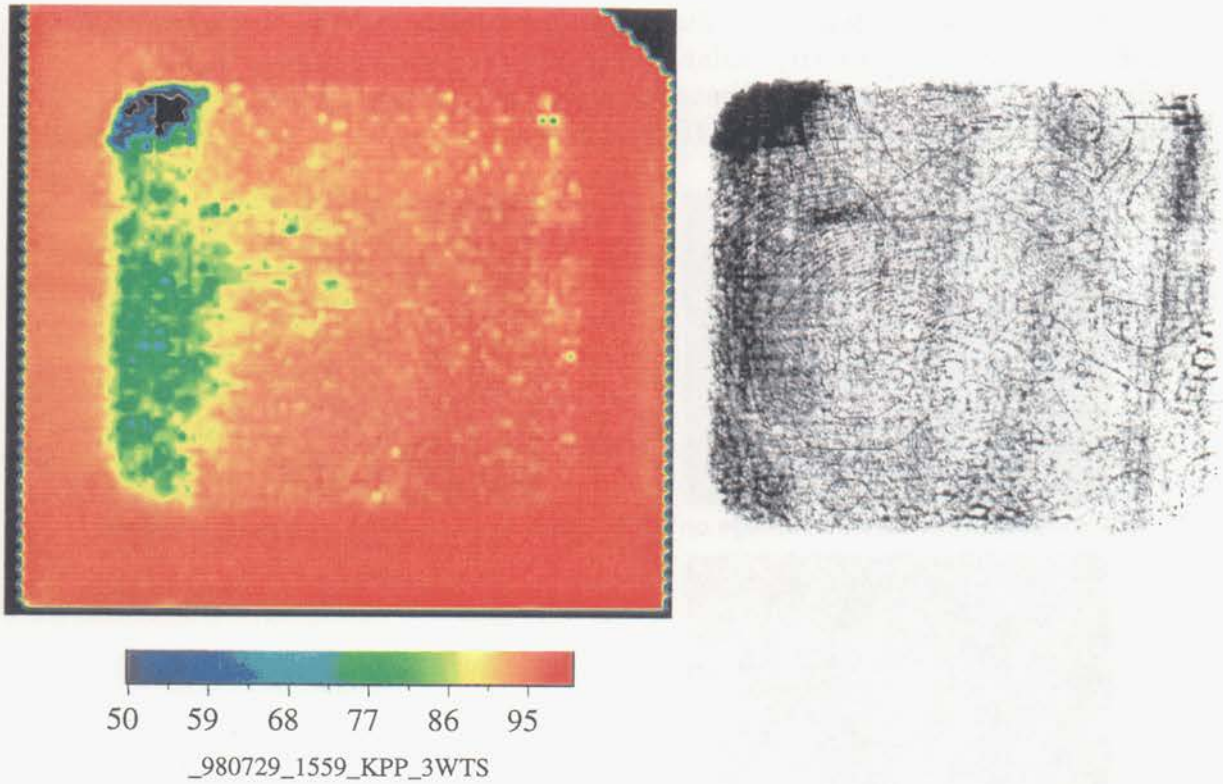

Figure 5-37. Transmittance of DOP2(KPP) after HDT2 campaign. DOP2 lost more than 8% transmittance, especially on the left side of the optic.

Large-aperture rastering off-line damage testing was carried out on DOP2 after the Beamlet campaign. Similar to the results with DOP1, damage density was nearly an order of magnitude lower for areas where the dipcoated AR coating was wiped off the diffractive structure on the input surface of the optic (Figure 5-38 and 5-29). In areas where the AR coating was not wiped off the KPP, damage morphology was similar to that observed on Beamlet—rear-surface damage with a strong correlation to the 2π steps of the KPP pattern shown in Figure 5-31.

ECMS NO CM RELEASE 20070611 14:14 0017657 OA (pdf format)

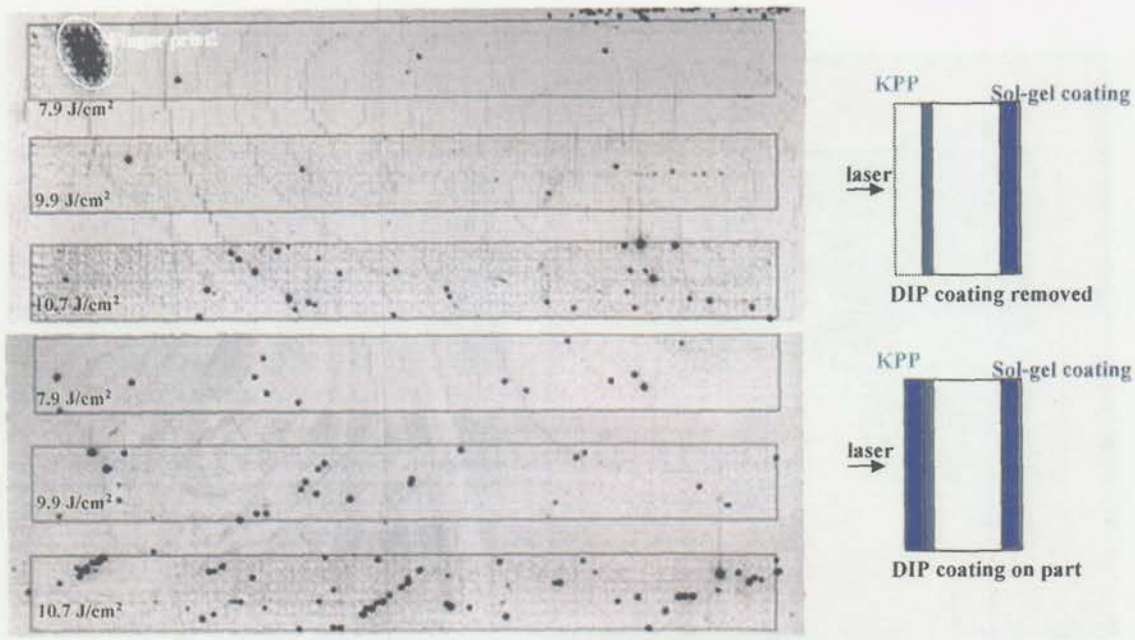

Figure 5-38. Off-line small beam raster testing of DOP2(KPP) after HDT2. Damage was significantly less on the KPP than on the CSG/BSG. Damage was significantly reduced when the sol gel was removed from the front (KPP) surface; remaining damage was still highly correlated with the 2π steps of the KPP.

Debris shield used with diffractive optics (DS02B)

The debris shield used with the diffractive optics showed damage patterns analogous to DOP2, but damage was more severe. The upstream beam modulations written into DOP1 and DOP2 were also written into the debris shield, including the KPP 2π steps (Figure 5-39b). Photometry showed a 3ω transmittance loss of about 10% overall (Figure 5-39a)—worse than the 4% and 8% losses observed on DOP1 and DOP2, respectively. As observed on the DOPs, the loss was most severe on the left (north) side. The upper left corner where DOP2 spit on the part showed losses of as much as 50%. Most of the particulate contamination was front surface, but most damage was rear surface.

ECMS NO CM RELEASE 20070611 14:14 0017657 OA (pdf format)

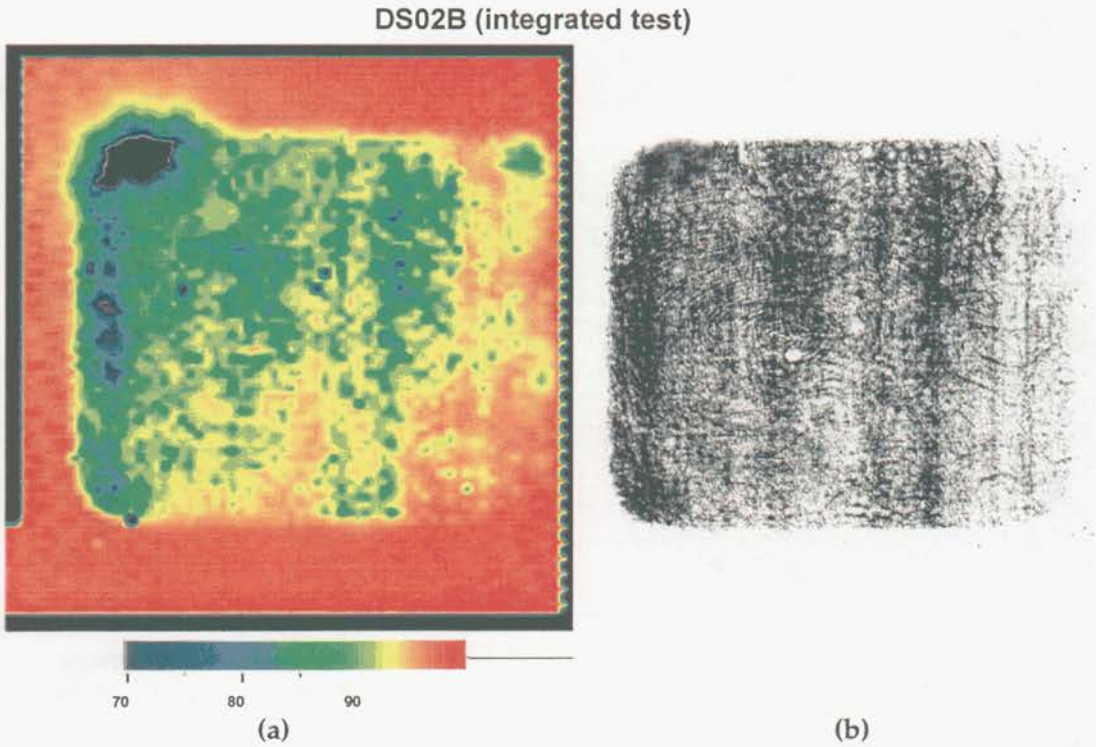

Figure 5-39 (a). Photometry of debris shield DS02B after HDT2(c) campaign with DOP1 and DOP2 in place and (b) DMS map of debris shield DS02B after HDT2(c).

The contamination pattern on the debris shield input surface appeared to be determined by the divergence of the debris from the adjacent optic. On DS02B where the upstream optic was only ~1cm away, the contamination was mostly inside the HDT2 beam footprint. This was quite different from the front surface particulate contamination observed on DS03K where the lens was the nearest upstream optics and was ~40 cm away. In this case, contamination was observed both inside and outside the beam footprint.

Potential Alternatives to the NIF Baseline

This Beamlet campaign suggests the NIF baseline configuration, which incorporates a dipcoated AR coating, is unfeasible. Even without a dipcoated AR coating, the downstream rear-surface damage density induced by modulations from the current 345-μm period CSG is one to two orders of magnitude higher than NIF optic lifetime goals require (see Figure 5-29).

A subaperture CSG has been under evaluation to increase 3ω transmission of the CSG and to minimize the footprint of unconverted light in the target chamber (see Figure 5-40). The currently recommended period of 1100 μm may be a preferred alternative to the current full-aperture design. A subaperture CSG covering about 15% of the full aperture would have a smaller damage footprint than the current full-aperture approach and would have about 3× lower density

ECMS NO CM RELEASE 20070611 14:14 0017657 OA (pdf format)

of 4π steps. In addition, modulation calculations have suggested this large-period stair-step grating would have about half as much modulation as the 345-μm period used on Beamlet. The combination of lower density of steps and lower modulation at each step would effectively reduce the damage density of such a grating by almost two orders of magnitude. If left uncoated, this may produce a CSG that would allow an acceptable lifetime of downstream optics.

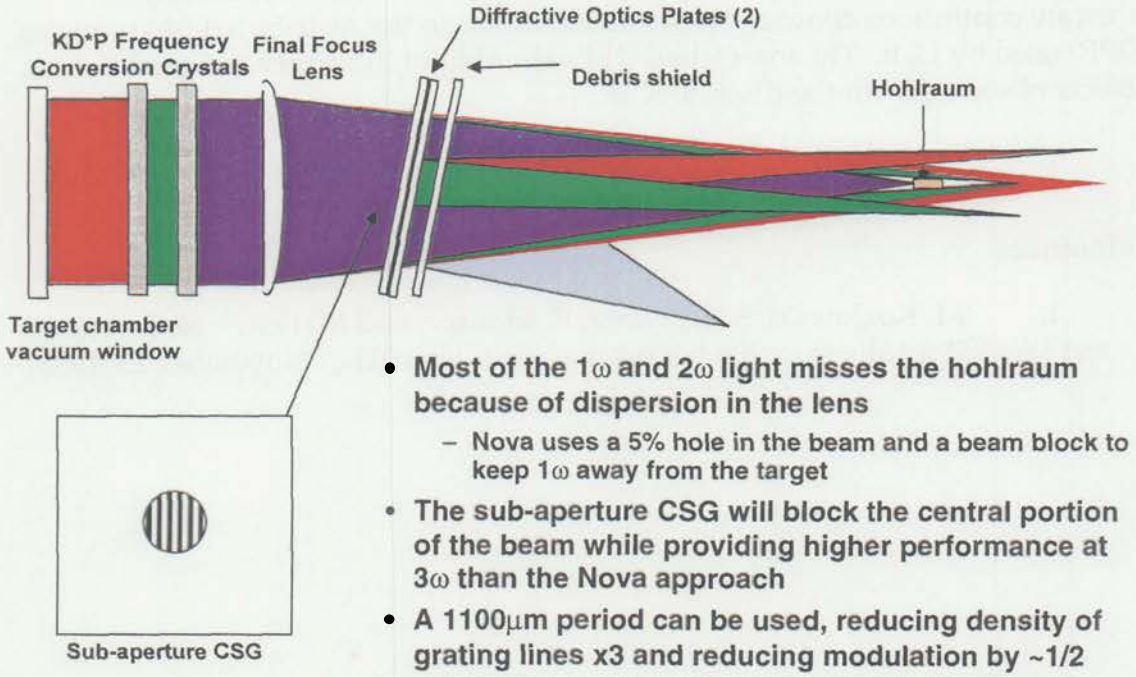

Figure 5-40. A subaperture color separation grating can improve transmittance while reducing damage probability.

Dipcoating of the current KPP design results in damage density on downstream optics one to two orders of magnitude higher than our target for damage density on the NIF. The current KPP may allow acceptable lifetimes for downstream optics if uncoated. Spincoating of colloidal-sol AR coatings has recently been shown to induce less damage than dipcoating, suggesting it may be feasible to AR coat the current KPP with a spincoating. However, it may prove impossible to achieve similar quality spincoatings on full-scale gratings.

The combination of an uncoated subaperture CSG with a spincoated KPP and spincoated BSG would provide 3ω performance similar to or greater than the current NIF baseline specifications for these three diffractive structures. These diffractive structures could be on separate DOPs or combined onto a single surface. The latter approach would be most attractive if it turns out to be unfeasible to AR coat the KPP or BSG.

If modeling and modulation measurements indicate current edge-width errors will likely induce unacceptable damage, we can use ion etching to

ECMS NO CM RELEASE 20070611 14:14 0017657 OA (pdf format)

fabricate gratings with less edge-width error than we observe on our current HF wet etching process. This would require development and facilities not currently in place in the NIF diffractive optics fabrication lab. However, it offers the possibility of reduced modulation-induced damage from the uncoated CSG and the KPP. Technical verification of ion-etched edge-width errors can be done on the existing reactive ion-etching chamber at LLNL's Vacuum Processing Lab.

If the discrete KPP is shown to be unfeasible, we can use ion etching to fabricate continuous contour phase plates similar to the distributed phase plates (DPP) used by LLE. The ion-etched DPPs should not introduce the modulation defects observed with the discrete KPP.

References

1. M. Kozlowski, S. Schwartz, R. Mouser, and M. Feit, " 3ω damage test (Y0005) results from Kodak reverse focus lens 01K," November 25, 1998.

ECMS NO CM RELEASE 20070611 14:14 0017657 OA (pdf format)

6.0 Improved AR Coatings for Conversion Crystals

Crystal coating development has traditionally focused on reducing the Fresnel losses for freshly coated crystals. Furthermore, all of the performance testing—optical and damage—has been conducted on clean coatings in air and at atmospheric pressure. The recent Beamlet experience [1,2] has underscored the importance of attacking the broader problem of improved transmission with long lifetime—including reflection, scatter, and absorption losses that develop with use in a vacuum environment. The problem can be broken down into four separable parts: (1) process and material development to enable improved coating designs, (2) characterization of optical and damage performance of these coatings in a clean vacuum environment, (3) process and material development to improve optical and damage performance in a contaminated vacuum environment, (4) process and material development to reduce scatter loss from damaged sol coatings or roughened KDP surfaces. As depicted in Figure 6-1, these four areas lead to specification of coated crystal performance, metrology requirements, and system design.

6.1 Process and Material Development for As-Made Coatings

An aggressive development plan has been implemented to improve the transmission of freshly coated KDP/KD*P crystals in air [3]. This plan is dependent upon success in four key areas:

1. Development of an improved spin-coating process.
2. Development of an intermediate-index coating for thermally annealed KDP.
3. Development of an intermediate-index coating for deuterated KDP.
4. Implementation of improved measurement capability to guide the coatings development program and to verify NIF production coatings.

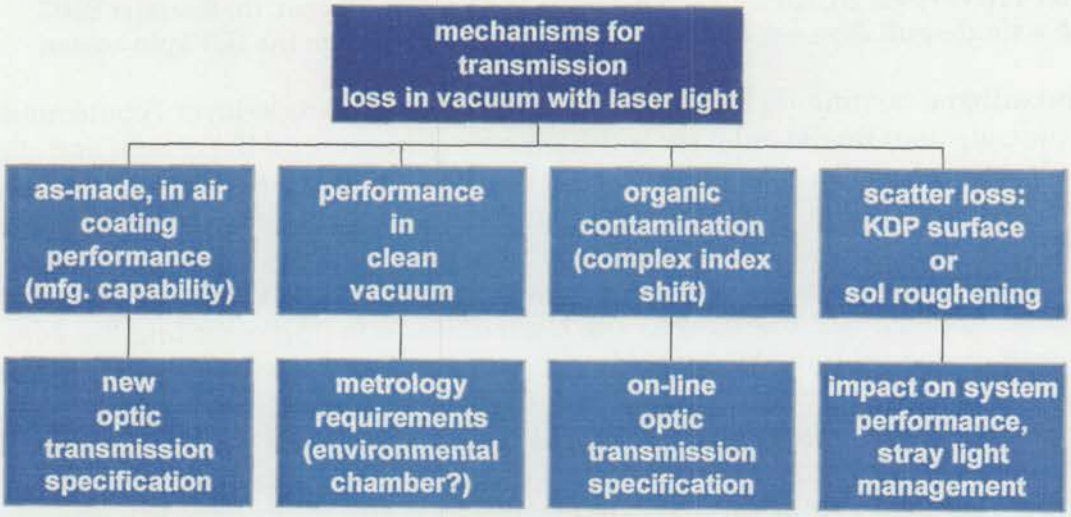

Figure 6-1. The problem of achieving improved crystal coating transmission with long lifetime can be divided into four separable areas.

ECMS NO CM RELEASE 20070611 14:14 0017657 OA (pdf format)

An improved spin-coating process is needed to obtain the required thickness repeatability and uniformity to meet tight performance specifications. This will enable us to put a different, optimized coating design on each surface of the crystal. The Nova/Beamlet spin-coat process had severe thickness nonuniformity and poor repeatability. A "covered chuck" spin coater has been procured for the NIF and process development on glass parts has begun. As shown in Figure 6-2, single-layer sol AR coatings with comparable optical performance to the dip-coated Beamlet KDP doubling crystals have been demonstrated. In addition, 37-cm optics that met the 0.7% 1ω and 2ω NIF reflection goal using a 2-layer broadband coating containing commercial, thermally cured GR650 silicone for the intermediate index layer have been produced. The limitations of the Nova measurement capability are rapidly being approached, which will defer further process optimization until the NIF photometer has been deployed in February, 1999.

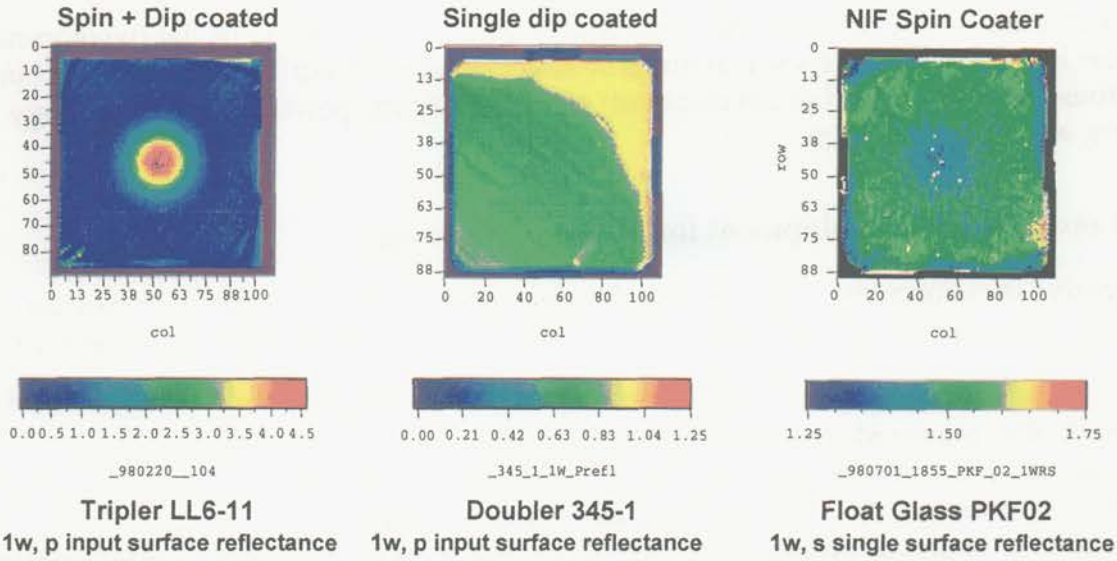

Figure 6-2. The NIF spin coater produces coating uniformity comparable to dipcoated Beamlet crystals: (a) Beamlet THG crystal coated by a combination of spin and dipcoat, (b) Beamlet SHG crystal coated with a single-pull dip coat, and (c) 41-cm float glass coated on the NIF spin coater.

A two-layer broadband coating [4] has two advantages over the single-layer "compromise" coating used on the output of the Beamlet second-harmonic generator (SHG) crystal and the input of the Beamlet third-harmonic generator (THG) crystal. As Figure 6-3 illustrates, the theoretical Fresnel losses at 1ω and 2ω for the broadband coating are roughly one-half the theoretical loss that can be achieved with a single-layer sol coating. Also, the broadband 2-layer coating is much less sensitive to coating thickness variability and hence will be much easier to manufacture to meet tight tolerances. The main obstacle to implementing the 2-layer coating on the output surface of NIF SHG crystals was concern that the reflected wavefront would be degraded. It has recently been verified that the reflected wavefront is not measurably altered for a 37-cm crystal. The deuterated THG crystal is not compatible with the thermal cure cycle currently used for the commercial GR650 silicone. Implementation of a broadband coating for the THG input surface will depend upon either developing a lower-temperature cure process for GR650 or successfully developing an intermediate-index material that cures at room or slightly elevated temperature.

ECMS NO CM RELEASE 20070611 14:14 0017657 OA (pdf format)

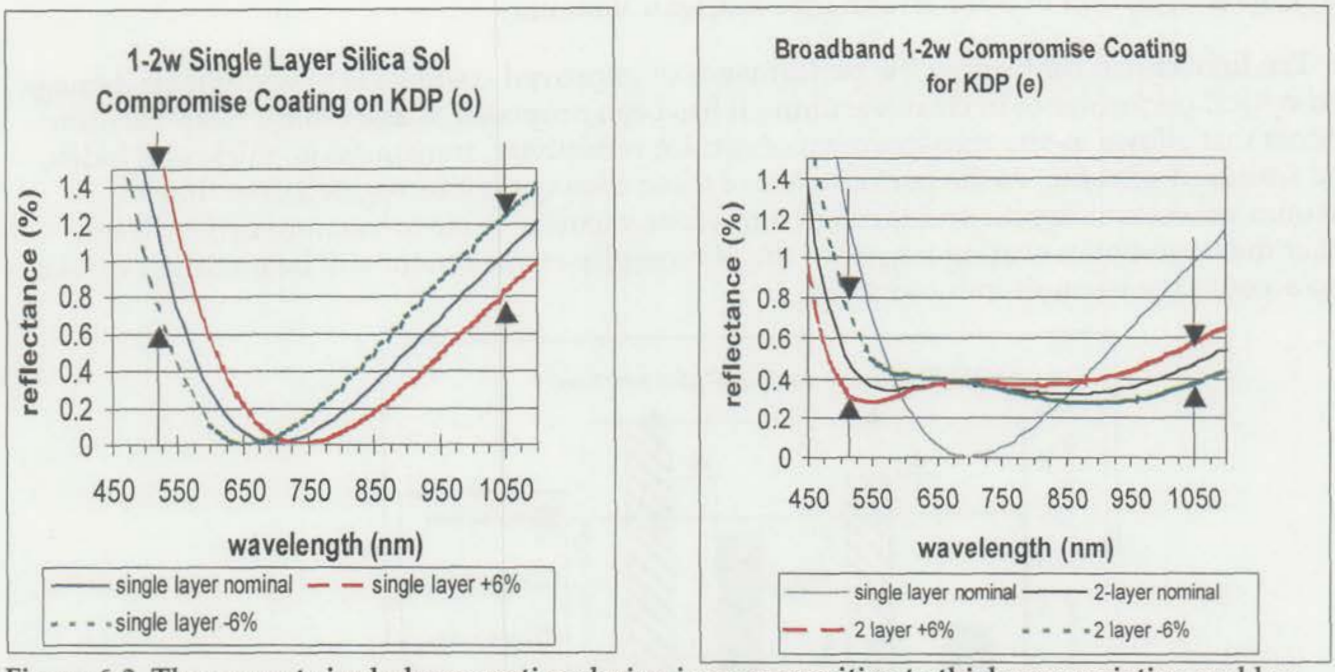

Figure 6-3. The current single-layer coating design is more sensitive to thickness variation and has higher reflection than the proposed 2-layer broadband design.

Process development of a room-temperature-cured silicone coating [5] made from hydrolysis of high-purity methyltriethoxysilane (MTS) and tetraethylorthosilicate (TEOS) has begun. It has been verified that the refractive index of a fully cured MTS/TEOS silicone is the same as that of the commercial GR650 silicone (1.43 at 633 nm). Figure 6-4 shows that the 3ω damage threshold falls within the range historically observed for GR650. Hence, if the 1ω and 2ω damage threshold of the MTS/TEOS silicone meet the NIF specifications, there will be no performance advantage to the thermally cured GR650, and resources will be focused on developing an MTS/TEOS material that can be used on both THG and SHG crystals.

Improved measurement capabilities to support the development and production of coated conversion crystals is the final development effort that is required to support improved transmission of as-coated crystals. Methods to support coatings development on small optics are currently being defined. Development of methods for large optics production is a longer-term objective. Assuming successful development of the materials and processes identified in this plan, full-scale demonstration of AR coatings on NIF-like crystals is expected to be complete in the fall of calendar year 1999.

ECMS NO CM RELEASE 20070611 14:14 0017657 OA (pdf format)

6.2 Characterization of Sol Performance in Clean Vacuum

The first step in confirming the performance of improved coatings is to verify their damage and optical performance in clean vacuum. It has been proposed to assemble a clean vacuum system that allows in-situ measurement of surface reflectivity, transmission, thickness, index, and scatter (if possible) as the performance of these coatings is interrogated over time in vacuum vs wet and dry air and through numerous vacuum-to-air-to-vacuum cycles. Then, either the large-optics coating targets or the photometry environment will be modified to take into account the vacuum-induced shifts.

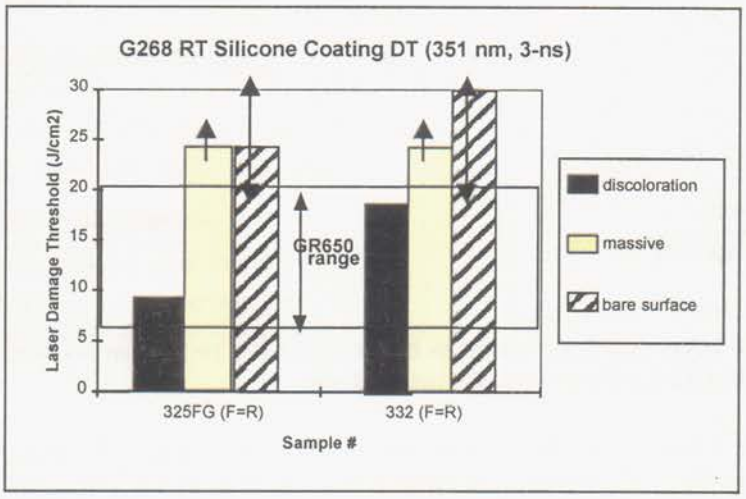

NIF Spec'n: 1 omega: Doubler, Tripler 18.0 J/cm²
3 omega: Tripler 14.3 J/cm²

Figure 6-4. Damage threshold of the G268 experimental room temperature cured silicone coating falls within the range of historically observed thresholds for commercial GR650 thermal cured silicone.

6.3 Development of AR Coatings with Reduced Affinity for Organics

The effect of environmental contamination of porous sol coatings has been well documented [6]. A plan to develop and test methodologies to modify the microporosity and surface chemistry of classical colloidal silica-sol AR coatings to minimize the adsorption of organic contaminants has been proposed. Treatment of the colloidal sol with a bulky silane coupling agent, HMDS, has been tested on fused silica, and it has demonstrated qualitative improvement. Preparation of HMDS-treated deammoniated sol and rigorous testing on KDP/DKDP should be completed in the spring, 1999. The hypothesis that a single-layer AR coating made from low-porosity Dupont AF2400 fluoropolymer film should have less capacity to adsorb organics will also be tested. However, the higher index of this material and the elimination of the 2-layer broadband design will reduce the theoretical optical performance for clean coatings. This longer-term, higher-risk solution will not be rigorously tested unless colloidal sol can not meet NIF requirements.

ECMS NO CM RELEASE 20070611 14:14 0017657 OA (pdf format)

6.4 Development of AR Coatings with Reduced Scatter Loss

There are two potential sources of scatter loss from conversion crystals: (1) roughening of the crystal surface itself [7] and (2) damage to the sol AR coating due to interactions of organic contamination and laser light. It is expected that scatter loss due to damage will be addressed concurrently with development of coatings with reduced affinity for organics.

Appendix C summarizes the photometry and microscopic inspection of a number of 5-, 27-, 32-, and 37-cm KDP and DKDP crystals. Some of these crystals were used in various Beamlet campaigns. Others were coated and stored in the Building 174 nitrogen-purged glove box, but never saw laser fluence. In addition, some of the 5-cm crystals were used on the OSL. These crystals exhibit a variety of defect morphologies that are correlated with significant transmittance losses. Defect morphologies change across crystal growth sectors and in response to the diamond turning process, crystallographic orientation (type I, II, or z-cut), coating chemistry, thermal history, and use environment (exposure to vacuum and/or laser fluence).

Significant (3 to 10%) transmittance reduction has been observed over 1 to 6 months for sol-coated crystals in the absence of vacuum or laser illumination. This transmittance loss is accompanied by the development of "squares," "diamonds," "triangles," "dashes," or "dots" on the crystal surface, as shown in Figures 6-5 through 6-8. It has been verified that when these features are found on 5-cm crystals, they do not penetrate the sol coating surface; the AFM is unable to detect them even though they are readily observed with >100× magnification on an optical microscope. The Wykko white light interferometer reports these features as 100 to 300 nm deep (below the surface), but it is not certain whether the interferometer perceives the active optical surface to be the sol coating or the KDP itself or some combination. Squares, diamonds, and triangles have only been found on 5-cm crystals. It is suspected that some of the dots observed on the large crystals are small triangles or diamonds that cannot be resolved with the Plato microscope. But no triangles were found on 80% LL1-12 when it was broken into small enough pieces to examine utilizing the same microscope as the 5-cm crystals.

"Line defects" (illustrated in Figures 5-8, B-2, and B-3) were only found after exposure to laser fluence in vacuum and only on the triplers (80% LL1-12, 80% LL6-11, and RG8A-1). None of the 37-cm Beamlet doublers, nor the 32-cm tripler that was operated in air (80% LL6-14), nor the 37-cm Beamlet mule tripler 70% LL1-37-1 developed line defects. (These crystals did develop 'dots'.) Line defects are pervasive on the output surfaces of both crystals, are clearly evolving on the input of LL6-11, and may be found with very high magnification sparsely populating the input of LL1-12. The depth of the line defects on the output of LL1-12 has been measured by both AFM and white light interferometry; the measured depth of 80 to 300 microns implies these slits penetrated both the 70-nm-thick sol AR coating and the KDP surface. (LL6-11 measurements are pending release of the crystal.)

Line defects differ from dashes only in their reflectance characteristics. Line defects are brighter than the sol-coated background, much as bare KDP appears in scratches and damage sites. Dashes are darker than the sol-coated background. Figure B-2 and B-3 suggests that dots and dashes may evolve into line defects by some as yet unknown mechanism. After the tripling campaign, dots and dashes (or line defects?) were observed on rapid-growth tripler

ECMS NO CM RELEASE 20070611 14:14 0017657 OA (pdf format)

RG8A-1. As seen in Figure 6-8, the dots and dashes are segregated by the prism-pyramid sector boundary. The crystal was subsequently refinished, recoated, and stored in the Building 174 glove box for five months. During that time, RG8A-1 developed dots and dashes without exposure to vacuum or laser fluence. There was no obvious segregation by sector boundary this time.

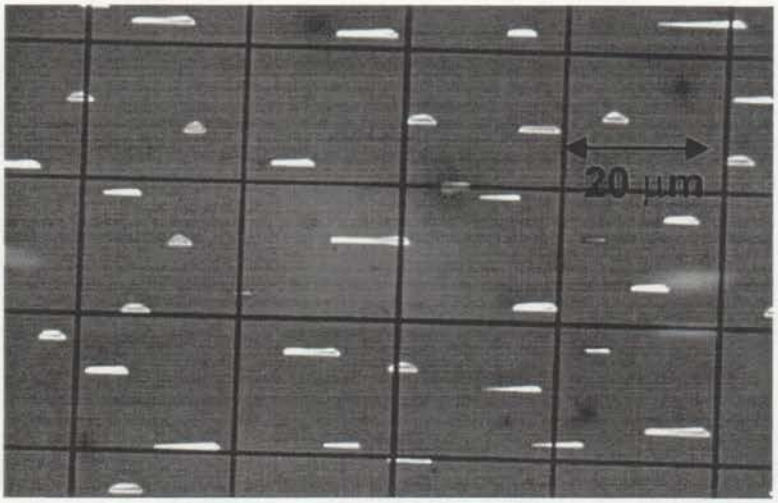

527 non-arrow side

Figure 6-5. 527-1, a type II 5-cm crystal (THG) diamond-turned at LLNL and coated with 80-nm of silica sol deposited from ethanol solution, developed "triangles" whose long axis is perpendicular to the projection of the z-axis. This is the same orientation as the line defects developed on the 37-cm triplers.

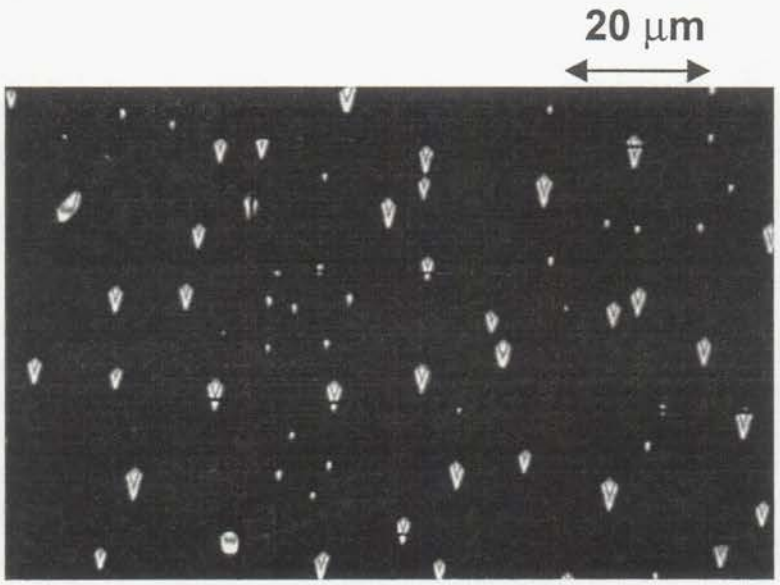

RG9B-54

Figure 6-6. RG9B-54, a type I 5-cm crystal (SHG′), diamond-turned at LLNL and coated with 145-nm of silica sol deposited from ethanol solvent, developed "diamonds" whose long axis is parallel to the projection of the z-axis.

ECMS NO CM RELEASE 20070611 14:14 0017657 OA (pdf format)

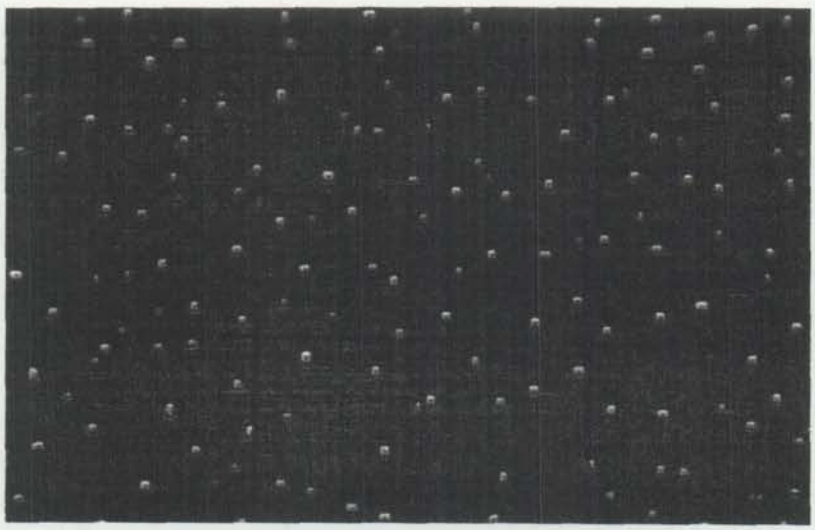

Figure 6-7. LL3-321, a 5-cm z-cut crystal, diamond-turned at CCI, coated with 215-nm of silica sol applied from sec-butanol solvent, developed "squares."

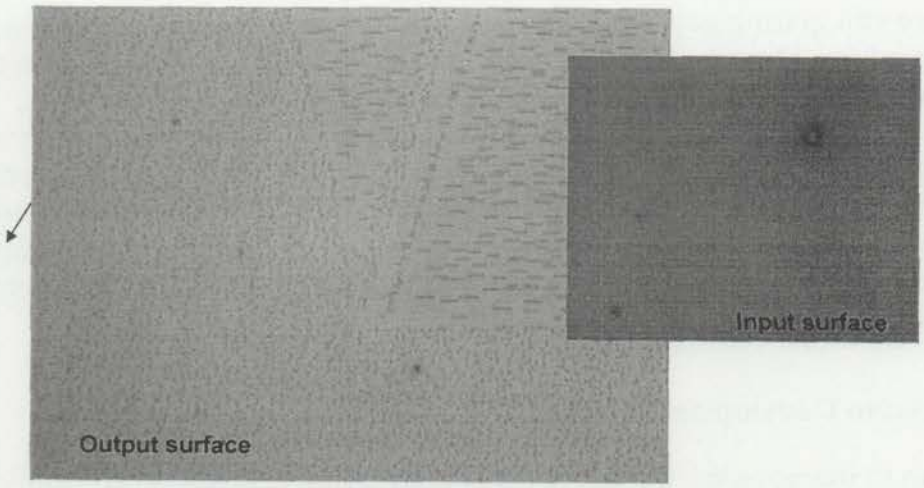

100x, after June rapid growth conversion campaign

Figure 6-8. RG8A-1 with dashes inside the pyramid sector on the output surface and dots everywhere else after the conversion campaign.

Recent inspections (June–December, 1998) found dots on both input and output surfaces of three 37-cm Beamlet doublers (345-1, 328-4, RG8B-2), the high-intensity/short-pulse triplers (RG8A-1, 70%LL1-37), and the 32-cm tripler LL6-14. (328-6 has not been inspected.) Dots were also reported on the input surface of the high-fluence 37-cm tripler (80% LL1-12) and on both surfaces of RG8A-1 after it was refinished, recoated, and stored for five months (no fluence or vacuum). Squares, triangles, and diamonds have been found on all aged, sol-only coated

ECMS NO CM RELEASE 20070611 14:14 0017657 OA (pdf format)

5-cm crystals, whether they were finished at LLNL or CCI and irrespective of whether the sol was applied from ethanol or secondary butanol solvent. Scattered squares and line defects were observed on a doubler and a tripler crystal that were coated with silica sol applied on top of room temperature-cured silicone. Line defects have only been found on three triplers that saw laser fluence and vacuum and are most prominent on the output surfaces of these crystals. The only crystals that do not have any periodic surface defects (dots, dashes, line defects, etc.) are (1) uncoated crystals, (2) crystals coated only with silicone (room temperature or thermal cured), and (3) thermally annealed crystals with either silicone/sol or sol-only coatings, and (4) sol-coated crystals that were finished with the experimental 80/10/10 Drakeoil 7/Lardcut/Lubrisol 936 diamond turning oil.

The routine development of these various surface defects makes it likely that much of the transmittance loss observed 'during' the Beamlet campaigns might well have developed in the absence of vacuum and laser light. Surface roughening is probably the source of the transmittance loss that could not be recovered by solvent washing, and most likely, only the ~1% transmittance loss that was recoverable by solvent washing was directly due to organic contamination of the sol coating. This would be consistent with the fused silica witness sample transmittance losses observed during the HDT campaigns and consistent with the observation that KDP specular reflection changes could not account for the observed decrease in transmittance.

Although there are still glaring gaps and inconsistencies in the above observations, some direction can be gleaned for directing future experiments to eliminate the scatter due to surface roughening. As the diamond turning process is developed on the new NIF flycutter, evaluation of diamond turning oil formulations that minimize the precursors to the various scattering defects is planned. This includes cleanable variations on the Drakeoil/Lardcut formulation. Evaluation of the effectiveness of thermal annealing KDP crystals in conjunction with silicone [8] coatings for doublers is also planned as well as evaluating room-temperature-cured silicone and fluoropolymer [9] coatings as a protective layer to prevent roughening of the THG crystal surface.

6.5 Facilities Required to Develop and Validate Improved Coatings

The proposed plan to improve the transmission of conversion crystals is predicated upon building a clean vacuum system with sufficient diagnostics to enable in-situ measurement of both the coating performance as well as relevant environmental and coating parameters. The system would include an RGA for gas analysis; an on-line scanning wavelength ellipsometer and spectrophotometer to measure coating thickness, index, absorption, reflection, and possibly scatter; a photometer for monitoring reflectance or transmittance at use wavelength; a cm-class 1, 2, and 3ω laser; and a 100 × Normaski microscope for observing damage morphology. This will enable us to determine which external factors are responsible for what observed change(s) in performance under controlled conditions. Such a facility would be used to evaluate optical performance and damage threshold in air and vacuum and in clean as well as organic-contaminated environments. Other off-line facilities such as precision photometry, scatterometry, and direct measurement of absorption would also need to be developed.

ECMS NO CM RELEASE 20070611 14:14 0017657 OA (pdf format)

6.6 Summary

Based upon successful completion of the proposed development plan, the goals shown in Table 6-1 have been established for sol-based conversion crystal coatings.

Table 6-1. Goals for sol-based conversion crystal coatings.

	Colloidal sol/ silicone coatings		AF2400		Beamlet degradation
Surface Loss %	Initial	Degraded (after 1 year)	Initial (AF2400)	Degraded (after 1 year)	Silica sol in 3–6 months
Crystal 1: SHG					
R1(1ω)	0.2%	1.0%	0.5%	0.7%	~0.5%
R2(1ω, 2ω)	0.7%	1.5%	1.5%	2%	~0.5%, 1–2%
Crystal 2: THG					
R1(1w, 2ω)	0.7%	1.5%	1.5%	2%	2%, 1–4%
R2(3ω)	0.2%	1.5%	0.5%	1.0%	3–5%

Goals for AF2400 fluoropolymer AR coatings are given to illustrate the potential trade-off that would be implicit in utilizing this backup technology. Finally, the goals are contrasted with the observations of degradation that occurs for single-layer sol coatings used on Beamlet. These goals will need to be reevaluated when development has progressed further.

6.7 References

1. P. K. Whitman, "Notes from the November 12th 3ω Optical Materials Working Group Meeting: Data-Dump on Beamlet Optics: Part 1," summarized by J. Campbell in NIF-0016748, December 1, 1998.

2. P. K. Whitman, Atherton's November 19, 1998 FOA Materials Review Meeting, "Beamlet FOA Data Dump: Part II (Beamlet and OSL KDP surface degradation)," summarized by A. Burnham in NIF0016682/rac.

3. P. K. Whitman, KDP Conversion TMP Review Meeting, "Conversion Crystals Coatings—Potential for Improvements," April 24, 1998, NIF0008425.

4. I. M. Thomas, "A two layer broadband antireflective coating prepared from a methyl silicone and porous silica," *Proc. of SPIE Sol-Gel Optics IV*, Vol. **3136**, 215–219 (1997).

5. I. M. Thomas, *Room-temperature cured broadband AR coating for KDP and amplifier blastshields*, Jan. 6, 1998, NIF0004306.

6. I. M. Thomas, Burnham, A. K., Ertel, J. R., and Frieders, S. C., "Method for Reducing the Effect of Environmental Contamination of Sol-gel Optical Coatings," *Solid State Lasers for Application to Inertial Confinement Fusion Conference* (June 7–12, 1998) UCRL-JC-1290x.

ECMS NO CM RELEASE 20070611 14:14 0017657 OA (pdf format)

7. M. R. Kozlowski et al., "Influence of diamond turing and surface cleaning proceses on the degradation of KDP crystal surfaces," *SPIE International Symposium* (July 21–26, 1991) UCRL-JC-105835.

8. I. M. Thomas, M. R. Kozlowski, G. Edwards, K. Stanion, and B. Fuchs, "Processes for the Elimination of Fogging on KDP Crystals Prior to and During Use in Laser Systems," *Boulder Damage Symposium* (October 23–25, 1991) UCRL-JC-108273.

9. I. M. Thomas and J. H. Campbell, "A novel perfluorinated AR and protective coating for KDP and other optical materials," *Boulder Damage Symposium* (Oct. 24–26, 1990).

ECMS NO CM RELEASE 20070611 14:14 0017657 OA (pdf format)

Appendix A

Orthogonal-polarization interferometry

Each converter crystal has two orthogonal crystal axes of interest in the plane normal to the direction of propagation, denoted as ordinary and extraordinary. The three fields in the harmonic conversion process are polarized along one or the other of these axes. In orthogonal-polarization interferometry , two transmission interferograms are made of the crystal with linearly-polarized light of wavelength λ_p; in one interferogram, the light polarization is parallel to the ordinary axis; in the second interferogram, the light polarization is parallel to the extraordinary axis. The difference of the two interferograms gives a distribution that is proportional to the thickness of the part times the difference of refractive indices in the extraordinary and ordinary directions ($\Delta n = n_e - n_o$). Using an approximation that the thickness of the part is constant, an approximate spatial Δn distribution is extracted from the data that can be used to model local departures from the phase-matching condition and thus predict local reductions in conversion efficiency.

Figure A-1(a) shows histograms of representative Δn distributions obtained from orthogonal-polarization interferograms of both conventional and rapid-growth doublers and triplers, expressed in terms of equivalent detuning angles. The equivalent detuning angles were calculated by assigning the variations in Δn to local changes in the direction of the crystal optic axis, so that

$$\Delta\theta = \Delta n \left[\frac{\partial n_e}{\partial \theta} \right]^{-1}_{\lambda_p} \tag{A1}$$

The relative impacts of these angular distributions on 3ω conversion efficiency have been calculated separately using the plane wave model, and are plotted versus drive irradiance in Figure A-1(b). The results predict the conversion efficiency at 3.5 GW/cm^2 for a converter using rapid-growth crystals to be 2% lower than one using conventional-growth crystals, in nominal agreement with the 1.5% measured on Beamlet and the 2.5% predicted by a full-diffraction calculation.

ECMS NO CM RELEASE 20070611 14:14 0017657 OA (pdf format)

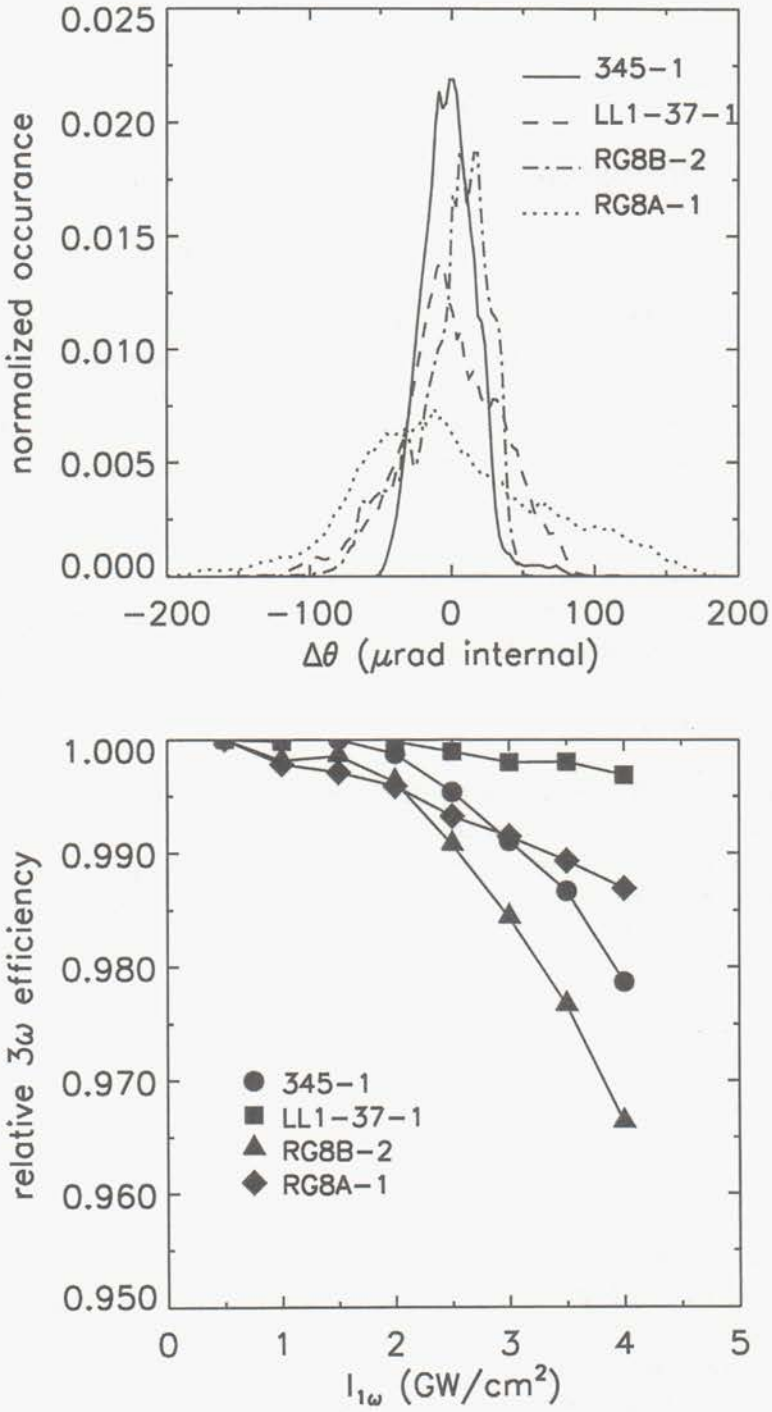

Figure A-1. (a) Histograms of representative Δn distributions obtained from orthogonal-polarization interferograms of both conventional and rapid-growth doublers and triplers. (b) The relative impacts of these angular distributions on 3ω conversion efficiency have been calculated separately using the plane wave model and are plotted versus drive irradiance. Nominal detuning angles for the doublers and triplers were 220 and 0 μrad respectively.

ECMS NO CM RELEASE 20070611 14:14 0017657 OA (pdf format)

Appendix B

HDTI Damage Investigation

At the conclusion of HDTI, the KD*P tripler was in the condition shown in Figure B-1. A comprehensive forensics effort was undertaken to identify the source of this damage. Optics, FOC components, and witness samples were analyzed using a variety of methods: photography, photometry, damage mapping and testing, optical microscopy, scanning electron microscopy (SEM) and energy dispersive spectroscopy (EDS) identification of particulate samples, gas chromatography and mass spectrometry (GCMS) of solvent wash residue, electron spectroscopy for chemical analysis (ESCA), auger spectroscopy, and secondary ion mass spectrometry (SIMS) of optics samples. Optical microscopy of the tripler surface revealed the unusual damage morphology shown in Figure B-2, including as yet unexplained line defects oriented perpendicular to the crystal e-axis and covering the entire surface with a spacing of ~20 μm. Solvent wash of the undamaged crystal surfaces, fused silica optics, and witness samples found ~0.5 $\mu g/cm^2$ of organic contamination in the sol gel. Di-octyl phthalate was found on all surfaces. Oil with a GCMS signature similar to KDP diamond-turning fluid found on the input surfaces of the tripler and lens, but not on the output surfaces. It was also found on the surfaces of the doubler, but was not extracted from a second doubler (345-1) when tested prior to laser exposure. Only a small amount of silicone was found on the surfaces, but it is expected that the solvent wash was not effective for this compound.

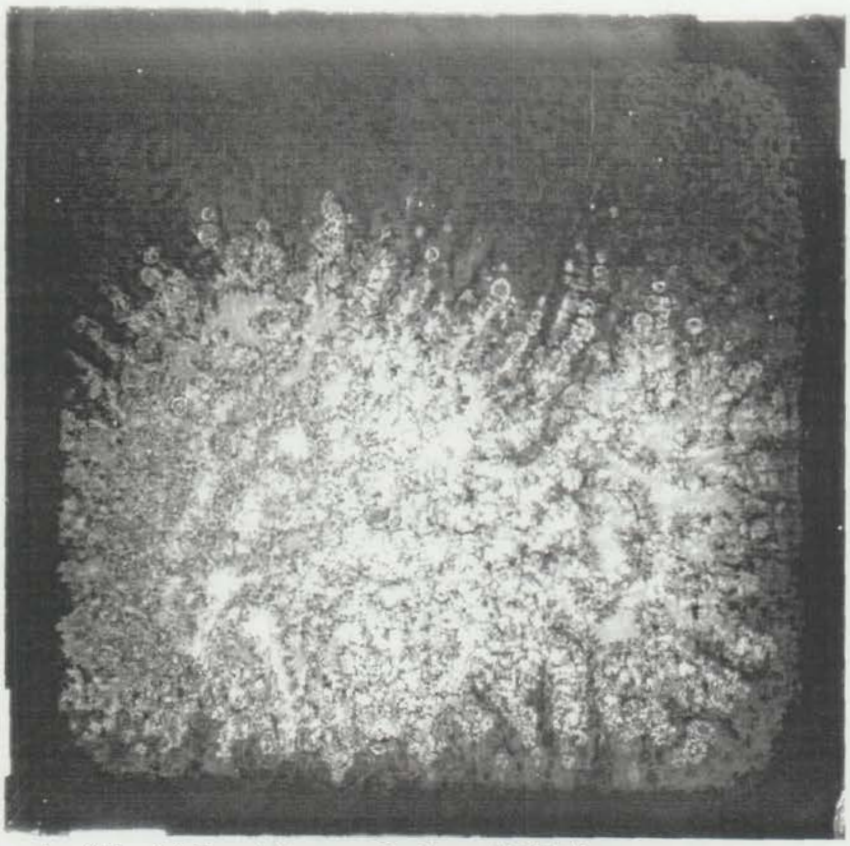

Figure B-1. Photograph of the tripler at the conclusion of HDTI.

ECMS NO CM RELEASE 20070611 14:14 0017657 OA (pdf format)

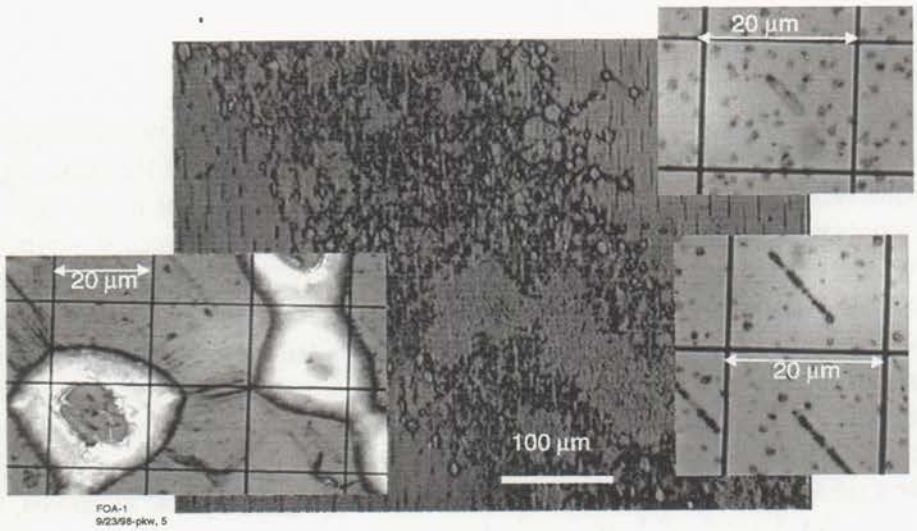

Figure B-2. Optical microscopy of the tripler surface revealed unusual damage morphology.

A corner of the tripler was broken off and tested directly for surface contaminants. SIMS found ~500 ppm of Al, 50 ppm of Fe, and 20 ppm of Cu on the output surface, both inside and outside the beam area. The input surface was not tested.

Particulate contamination found on the FOC and on the optic surfaces was identified with the SEM. Many particles of silica or substoichiometric silica were found on the output surface of the tripler, both surfaces of the lens, the sides of the FOC and cap flange, and the compliant element. Many of these particles appeared to be in molten form (see Figure B-3). The oxygen content of these particles was determined to be less than the virgin sol gel (SiO_2) but more than the compliant element. Fourier-transform infrared spectroscopy of the compliant element found no decomposition resulting from use. The remaining particles on the lens input surface were primarily Al or Al compounds. Very few KD*P particles were found on the input surface of the lens and bottom of the cell.

Off-line 3ω damage testing in air was unable to reproduce the on-line damage morphologies. The tripler was tested from 2 to 8 J/cm^2 (equivalent 3-ns fluence). Bulk damage prevented testing the surfaces at > 8 J/cm^2. The only observed surface damage was sol flaking. The input surface started at lowest fluence. The output surface inside the beam area had the least damage. Solvent cleaning eliminated sol-flaking from all surfaces. The lens was tested to an equivalent 3-ns fluence of 8 J/cm^2. The input surface inside the beam area did not damage. Outside the beam area, damage occured in the form of shell cracks. Some laser cleaning of particulate contamination was observed.

ECMS NO CM RELEASE 20070611 14:14 0017657 OA (pdf format)

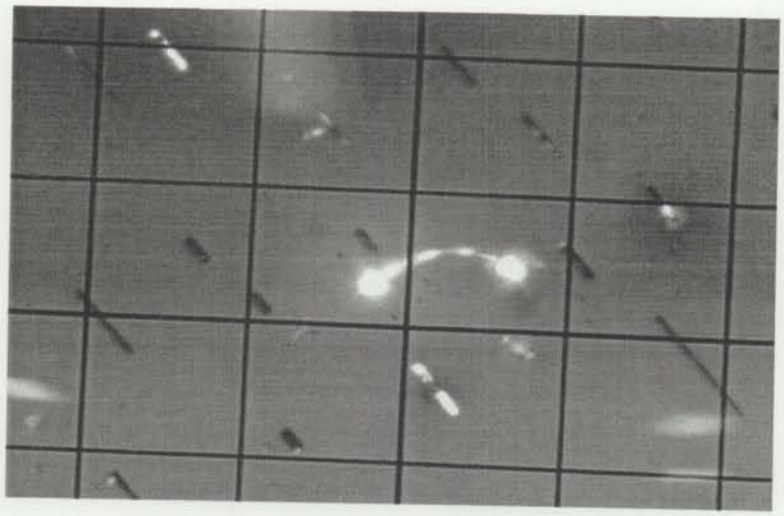

Figure B-3. Optical micrograph of second surface of tripler. Many particles of silica or substoichiometric silica found on the FOC and on the optic surfaces appeared to be in molten form.

ECMS NO CM RELEASE 20070611 14:14 0017657 OA (pdf format)

ECMS NO CM RELEASE 20070611 14:14 0017657 OA (pdf format)

Appendix C

37-cm Tripler (type II) Crystals (all finished at CCI)

Crystal ID	LL1-37-1 70% DKDP	RG8A-1 83%DKDP	LL1-12 80%DKDP	LL6-11 80%DKDP	32-cm LL6-14 80%DKDP	293-3 KDP	27-cm Nova* KDP	LL3-3* 80% DKDP	RG8A-1 83%DKDP
DTM Date	3/10/98	4/28/98	1/17/98	5/15/98	4/26/94	1994	5/98	5/98*	7/9/98
Rework # of times	0	0	3	3	0	0	N	N	1
Last Chuck side	Input				Input				
Date coated	3/17/98	6/1/98	6/29/97	5/26/98	6/21/94	10/15/98	~5/15/98	~6/12/98	7/14/98
SOL BATCH / Solvent	IT / EtOH	IT / EtOH	IT / EtOH	IT / EtOH	CB / EtOH	Small IT/BuOH-EtOH	IT/ EtOH	IT/ EtOH	ACSI AC-3/EtOH
Silicone ctg	None	None	None	None	None	GR650	None	None	None
Fluence or campaigns (Peak fluence at 3ns or equivalent)	CG tripling 4 J/cm², 1.5ns (5.6 J/cm², 3ns equiv)	RG tripling 3.8 J/cm², 1.5ns (4.2 J/cm², 3ns)	PhaseI (0.6 J/cm²,0.2ns) MDT (5.8J/cm², 3.4ns) HDTI (6.2 J/cm², 3.2ns)	CEA (0.2 J/cm², 0.2ns) CEA (1.1J/cm², 3ns) HDTII(7.8J/cm², 3.1ns)	32 cm activation (x3) 8.2 J/cm², 3ns	0	0	0	0
Vacuum Yes/No	Yes	Yes	Yes	Yes	No	No	No	No	No
Input ctg (λ peak)	700 nm	370 nm	350 nm	350 nm	350 nm	700 nm	700 nm	1053 nm	370 nm
Input Morphology	Meteors, no slits @ 100x (6/98)	Dots @ 100x (6/98)	dots at 100x (6/98) very few, small slits @ 1250x (11/98)	Elongated dots @ 100x (8/98)	Dots@ 500x (10/98)	Nothing of note @ 500x (11/24/98)	Nothing of note @ 500x (12/8/98)	Nothing of note @ 500x (12/10/98)	Small triangles? Dots? @ 500x – everywhere (11/25/98)
Output ct (λ peak)	350 nm	370 nm	350 nm	350 nm	350 nm	350 nm	350 nm	1053 nm	370 nm
Output morphology (date examined)	No dots or dashes @ 100x (6/98) Dots (very small triangles?) 12/98	Dashes –in pyr near boundary Dots- all other (6/98)	Slits, other 'high energy' damage (6/98 – 11/98)	Long Slits, tightly packed (8/98 – 11/98)	Dots (10/98)	Small triangles? Only around coating defects(11/24/98)	Nothing of note @ 500x (12/8/98)	Nothing of note @ 500x (12/10/98)	Small triangles? Dots? @ 500x – everywhere (11/25/98)
Other Comments	SBS'd (surface cracked)		massively damaged in HDT 1, discrete surface damage started during MDT	many lg. discrete damage sites HDT II	White scatter	Photometry unchanged after 5 wks. storage	Lots of coating defects (LLNL cleaned this one after DT)	CCI setup crystal z-cut Very clean	Photometry – dropped 2 – 3% T a 2ω by 12/4/98
Diffract (linearly)		No	Yes	Yes	No	No (little scatter)			No (lots 2π scatter)

Notes:

CCI standard oil is based on Drakeoil 7, with proprietary additives

*CCI is experimental formulation of Drakeoill 7/ Lard cut / Lubrizol 936 (80% / 10 %/ 10%)

ECMS NO CM RELEASE 20070611 14:14 0017657 OA (pdf format)

37-cm Doubler (Type I) Crystals (all finished at CCI)

Crystal ID	32-cm 311-4 KDP	32-cm 311-2 KDP	328-4 KDP	345-1 KDP	RG8B-1 KDP	RG8B-2 KDP
DTM Date	1994	6/94	~ 12/97	12/30/97	2/25/98	2/20/98
Rework # of times	0	0	0?	0	0	0
Last Chuck side						
Date coated	~1994??	6/94	1997?	1/98	5/14/98	~3/22/98
SOL BATCH / Solvent	CB / EtOH??	CB / EtOH	IT / EtOH	IT / EtOH	IT / EtOH	IT/ EtOH
Silicone ctg	GR650??	GR650	None	None	None	None
Fluence or campaigns	0? ('spare')	32-cm activation	CEA	conversion	0	HDT1&2
Vacuum Yes/No	No	No	Yes	Yes	No	Yes
Input ctg (λ peak)	700 nm?	700 nm	700 nm	700 nm	350 nm	700 nm
Input Morphology (date examined)	Tiny Dots (12/98)	Needs inspection	Dots (12/98)	Dots (12/98)	Nothing of note @ 500x coated or uncoated areas (12/4/98)	Diamonds @ 500x, but sparse in center. (11/24/98)
Output ct (λ peak)	700 nm?	700 nm	700 nm	700 nm	350 nm	700 nm
Output morphology (date examined)		Needs inspection	(Arrow side) Dots, dense (12/98)	Dots (12/98)	Nothing of note @ 500x coated or uncoated areas (12/4/98)	Diamonds? @ 500x, but much sparser in center. (11/24/98)
Other Comments	Burns (laser damage of GR650?)		White scatter 'cross-hair' pattern both sides	SBS'd 'holes' on output from SBS event?	Thermal annealed at 160 C, 6 days? Bottom ~1/4 didn't coat.	~3 %T drop first time used, stayed ~constant after that
Diffract (linearly)	History unclear. (working on it)					No

Notes:

CCI standard oil is based on Drakeoil 7, with proprietary additives

*CCI is experimental formulation of Drakeoill 7/ Lard cut / Lubrizol 936 (80% / 10 %/ 10%)

ECMS NO CM RELEASE 20070611 14:14 0017657 OA (pdf format)

5-cm Crystals

	527-1 DKDP	529-1 DKDP	524 KDP	324 KDP	RG9-54 KDP	LL3-321 DKDP	328-212 KDP	LL6-54 DKDP	325FG KDP	CCI332 KDP
DTM Site	LLNL	LLNL	LLNL	LLNL	LLNL	CCI	CCI	CCI	CCI	CCI
CTD Date	7/98	7/98	7/98	7/14/98	7/98	~1/96	~1/96	9/10/98	8/5/98	8/5/98
SOL Batch	ASCI AC-3/ EtOH	ASCI AC-3/ EtOH	ASCI AC-3/ EtOH	ASCI AC-3/ EtOH	ASCI AC-3/ EtOH	Sec-BuOH small lot	None	None	ASCI AC-3/ EtOH	ASCI AC-3/ EtOH
Silicone	No					No	GR650	RT Cure	RT Cure	RT Cure
Fluence	OSL?	OSL?	None	None	OSL?	DT	DT	None	DT	DT
Vacuum	No	No	No	Mule	No	SEM	No	No	No	No
CTU	370 nm	370 nm	700 nm	350 nm	700 nm	1050 nm	700 nm	700 nm	700 nm	700 nm
Morph	Obtuse Δ (10/9/98)	Obtuse Δ (10/9/98)	Diamond (11/10/98)	Square (10/17/98)	Diamond (10/9/98)	Square (10/27/98)	None (11/10/98)	None (11/10/98)	Slits where sol/silicone coated, silicone only - none @ 500x (9/3/98)	squares where sol/s coated, none where silicone only @ 500x (12/98))
Diffract	Yes	Yes		No	Yes					
Comments orient (cut)	Tripler	Tripler	Doubler	Z cut	Doubler	Z cut finished 1/6/95	Z cut	Z cut	Tripler? (not z cut by arrow)	Z cut

Notes: Input surface coating and morphology is same as output surface for all 5-cm xtals
LLNL finishing uses pure Drakeoil 7
CCI standard oil is based on Drakeoil 7, with proprietary additives

ECMS NO CM RELEASE 20070611 14:14 0017657 OA (pdf format)

ECMS NO CM RELEASE 20070611 14:14 0017657 OA (pdf format)

ECMS NO CM RELEASE 20070611 14:14 0017657 OA (pdf format)